Rheinland-Pfälzische Technische Universität

Fachbereich Chemie

Activation of dinitrogen on size selected transition metal cluster anions at cryo temperatures

Vom Fachbereich Chemie der Rheinland-Pfälzischen Technischen Universität Kaiserslautern-Landau zur

Verleihung des akademischen Grades „Doktor der Naturwissenschaften“ genehmigte

Dissertation

DE-386

vorgelegt von

Maximilian Luczak, M.Sc.

geboren in Birkenfeld/Nahe

Betreuer: Prof. Dr. G. Niedner-Schatteburg

Tag der wissenschaftlichen Aussprache 24.03.2026

Rheinland-Pfälzische Technische Universität 2026

Die vorliegende Arbeit wurde Zeitraum von Februar 2019 bis Januar 2026 im Fachbereich Chemie der Rheinland-Pfälzischen Technischen Universität unter Betreuung von Prof. Dr. G. Niedner-Schatteburg angefertigt.

Datum der Eröffnung des Promotionsverfahrens 5. Februar 2026

Promotionskommission:

Vorsitzender: Prof. Dr. W. Tiehl

1. Berichterstatter: Prof. Dr. G. Niedner-Schatteburg

2. Berichterstatterin: Jun.-Prof. Dr. Jennifer Meyer

Table of Contents:

Table of Contents: 12
1 Introduction 1
1.1 The fixation of molecular nitrogen 1
1.2 Probing elementary steps in the catalytic activation of nitrogen 5
1.3 Literature 10
2 Experimental setup and quantum chemical methods 12
2.1 Laser Vaporization Cluster Source 12
2.2 Electrospray Ionization Source 14
2.3 Fourier Transform Ion Cyclotron Resonance Mass Spectrometry 17
2.4 The FT-ICR mass spectrometer FRITZ 19
2.5 OPO/OPA IR Laser system 22
2.6 Infrared-multiple photon dissociation 24
2.7 Quantum chemical methods 26
2.8 Literature 28
3 Influence of the charge state on the N_2 adsorption on size selected cobalt cluster ions in isolation 31
3.1 Preamble 31
3.2 Abstract 31
3.3 Introduction 32
3.4 Experimental & computational methods 33
3.5 Results and discussion 35
3.6 Conclusion 39
3.7 Literature 40
3.8 Supporting information 42
4 Nickel Cluster Anions in the gas phase at cryo conditions 47
4.1 Preamble 47
4.2 Abstract 47
4.3 Introduction 48
4.4 Experimental & computational methods 49
4.5 Results & Discussion 50
4.6 Conclusion 57
4.7 Literature 58
5 Nickel cluster cations in the gas phase at cryo conditions 59
5.1 Preamble 59
5.2 Abstract 59

5.3 Introduction 60
5.4 Experimental & computational methods 60
5.5 Results & Discussion 61
5.6 Conclusion 65
5.7 References 66
6 Nitrogen adsorption and activation on size selected ruthenium cluster anions under cryo conditions in isolation 67
6.1 Preamble 67
6.2 Abstract 67
6.3 Introduction 68
6.4 Experimental and Computational Details 69
6.5 Results and Discussion 71
6.6 Summary and Conclusions 83
6.7 Acknowledgments 83
6.8 Author Contributions 84
6.9 References 85
6.10 Supporting information 90
7 Activation of dinitrogen on anionic ruthenium clusters 97
7.1 Preamble 97
7.2 Introduction 97
7.3 Experimental 98
7.4 Results and Discussion 99
7.5 Conclusion 107
7.6 Literature 108
8 Summary, conclusion, and outlook 109
9 Short Summary 119
10 Kurzzusammenfassung der Dissertaion 120
Lebenslauf 122
List of publications 123
Danksagungen 124
Eidesstattliche Erklärung 125

1 Introduction

1.1 The fixation of molecular nitrogen

Molecular dinitrogen is abundantly available in its gaseous state, as it makes up 78 % of the earth's atmosphere.[1] The two nitrogen atoms form a strong triple bond which makes the gas chemically inert.[2] Nitrogen-containing organic compounds are present in all organisms. They occur among others in amino acids and thus proteins, nucleobases comprising the DNA and adenosine triphosphate (ATP), the energy transporting agent in cells. The pathways of nitrogen containing organic compounds in the biosphere are summarized in nitrogen cycles which have been formulated for many different biotopes, highlighting the importance of this class of substances to living organisms on earth.[3][4] A significant growth of the biosphere thus requires the availability of nitrogen to the biosynthesis of molecules.

The generation of bioavailable nitrogen compounds is called nitrogen fixation. Nitrogen fixation can occur both biologically and abiologically. The inert characteristics of molecular dinitrogen pose a significant challenge to the process. The only source of fixated nitrogen from gaseous dinitrogen is the enzymatically catalyzed conversion of dinitrogen to ammonia.[5] The class of enzymes enabling this reaction are nitrogenases. They are found in cyanobacteria and rhizobacteria.[6]

Obtaining bioavailable nitrogen requires breaking the strong triple bond of molecular dinitrogen. This process is called the activation of dinitrogen. Nitrogenases enzymes contain metal-sulfur structures as well as molybdenum and sometimes vanadium cofactors. In the nitrogen fixation process they use $NADH^+$ as a reducing agent and ATP as an energy source to break the bond at room temperature and moderate conditions.[3,7] This process, however, is slow and the enzyme rare enough to make biologically fixated nitrogen a finite resource for the biosphere.

During the industrial revolution with its' fast-growing human population and the development of modern chemistry, a need for an industrial pathway to nitrogen fixation was imminent.[8] Natural resources such as niter were used for explosives, but more importantly artificial fertilizers, to meet the increasing demands in food production.[9] The idea to tab into the atmospheric resources of molecular nitrogen was intriguing.[10] The Haber-Bosch process was the first industrially successful activation of molecular nitrogen, using molecular nitrogen and hydrogen to produce ammonia.[11] The reaction is favored by the reaction enthalpy but hindered by its' entropy.

$$N_2 + 3\,H_2 \rightleftharpoons 2\,NH_3 \quad \Delta H_{298K} = -46{,}14\ kJ/mol \qquad (1\text{-}1)$$

The Haber-Bosch process therefore uses high pressure and comparatively low temperatures as reaction conditions alongside an alpha-iron catalyst.[12] The significance of this development was honored with a Nobel prize to Fritz Haber in 1918 and Robert Bosch, for more general high-pressure chemistry. The Haber-Bosch process was successfully implemented in the chemical industry and remains one of the most important chemical processes on the planet.[10] Therefore, a better understanding of the process, and developments to improve efficiency have a significant impact on the global energy consumption. Today, 1-3 % of the yearly energy consumption, along with 3-5 % of the yearly hydrogen supply is linked to the synthesis of ammonia.[13]

Ertl et all studied the ammonia synthesis on an alpha-iron catalyst in detail.[14–16] The diagram figure 1.1 shows the elementary reaction steps in the activation process of molecular nitrogen.

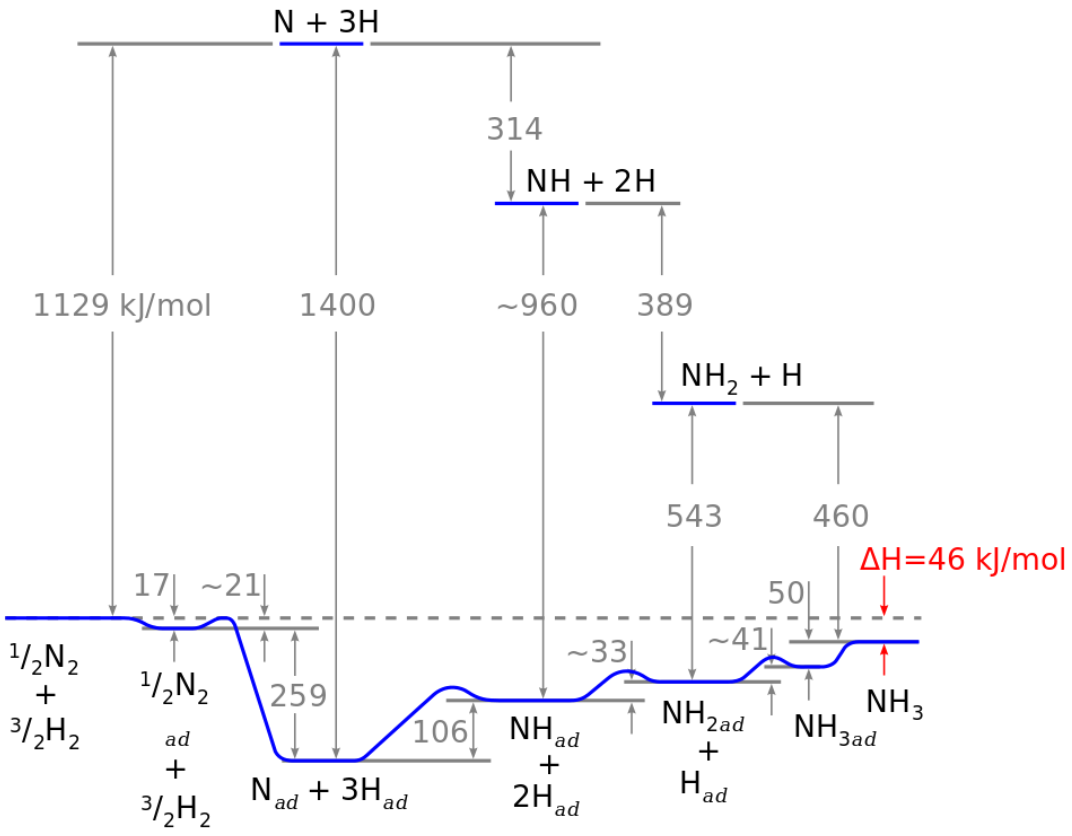


Figure 1.1: [15] The elementary Haber-Bosch process as described by Ertl et al. Numbers refer to the difference in Enthalpy in kJ/mol.

In the first series of steps, molecular nitrogen and hydrogen is adsorbed to the catalyst surface. In the second step the nitrogen and hydrogen bonds are cleaved, resulting in nitrogen and hydrogen atoms being adsorbed to the catalyst surface. Note, that in this step the bond breaking enthalpy amounts to 1129 kJ/mol, but the catalyst lowers the activation energy to 21 kJ/mol.[16] The following steps show a sequential addition of hydrogen atoms to the nitrogen. The steps have low energy boundaries and result in an adsorbed ammonia molecule residing on the catalyst.

The work of Ertl assigns demanding characteristics to the catalyst material. The adsorption step and subsequent cleavage of the nitrogen bond require a flexible electronic structure of the catalyst. The catalyst and the adsorbed nitrogen form a σ-donor – π-acceptor complex. Electron density along the binding axis must be accepted by the catalyst to facilitate the adsorption. Simultaneously, electron density is donated into the π*- orbitals of the nitrogen molecule, leading to its cleavage.

Modern catalyst systems often use ruthenium as the primary catalyst. Ruthenium is larger compared to iron and thus more polarizable.[17] The electron density is supported by promotors, often alkali metals, which supply electrons to the reaction. Complex electride structures are used to enhance the performance of the ruthenium catalyst by improving the electronical structure for the process.[18]

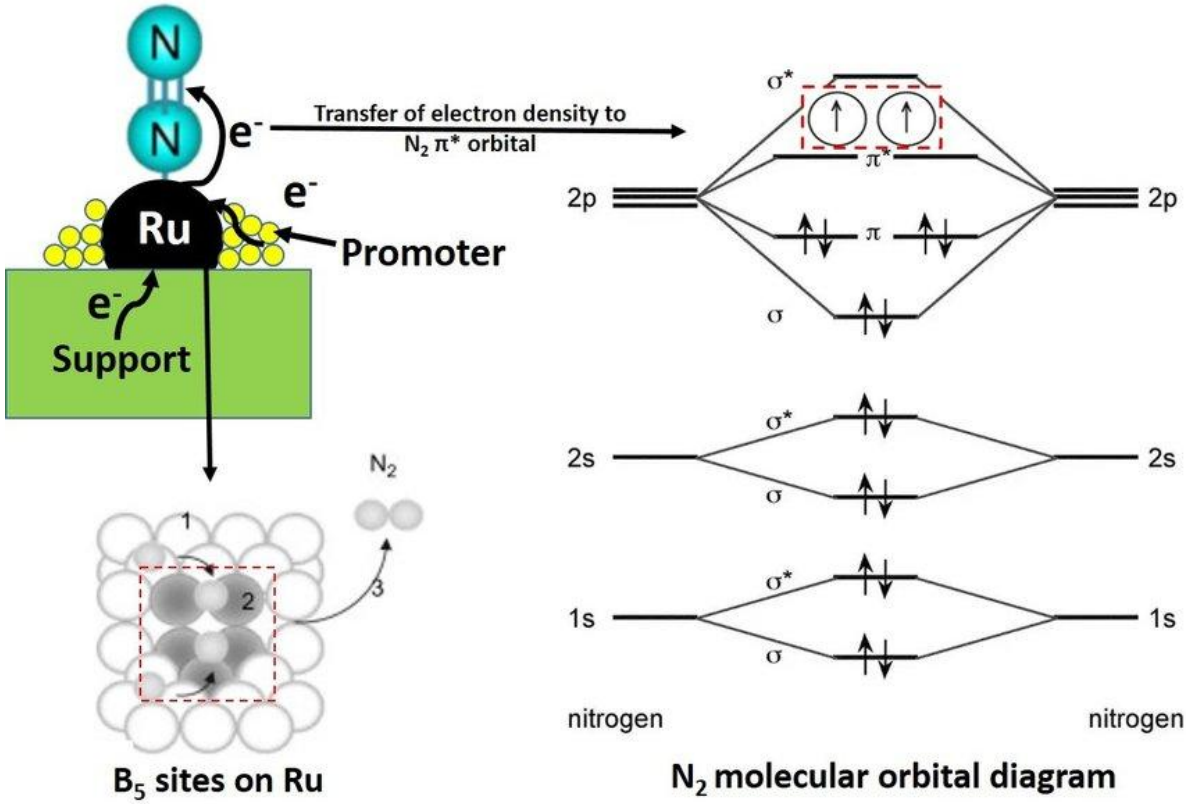


Figure 1.2: [19] Geometric assembly of catalytically active B5-sites on a ruthenium catalyst.

Geometric features play a significant role in the process as well. Ruthenium is often applied as a doting spot onto the support surface, being dots, several layers of ruthenium high, featuring edges and rifts. The edges feature so called B5-sites which are shown to be favorable for the activation process.[19]

1.2 Probing elementary steps in the catalytic activation of nitrogen

Clusters are agglomerates of molecules or atoms in the size range between 3 and ~100 units. Clusters show size dependent physical properties which can have an influence on their reactive behavior.[20] Transition metal clusters combined with ab initio quantum chemical modeling allow the study of geometrical and electronic features. In this work, we study size-selected transition metal clusters and their reaction with one or multiple dinitrogen molecules to further the understanding of elementary steps in the activation process found in catalytic processes.

To probe TM cluster – absorbate complexes we create charged transition metal clusters using a laser vaporization ion source and two subsequent cryo-traps for the absorption of nitrogen to the TM cluster and the selection and storage of a specific TM-cluster nitrogen complex. The setup allows the study of nitrogen uptake kinetics as well as IR-photo-dissociation action spectroscopy.[21–23]

The interaction of the TM cluster with the dinitrogen adsorbent will lead to a σ-donor – π-acceptor complex. In this process the anti-binding orbitals of the nitrogen molecule will be populated and lead to a weakening of the triple bond. Since the symmetry of the dinitrogen is broken after the absorption to the TM cluster surface, the stretching mode of the molecule becomes IR active. The weakening of the triple bond will result in a red shift of the IR signal and can give an insight into the activation of the bond by the interaction with the TM cluster.

This phenomenon has been described by Blyholder et al. In this work, carbon monoxide was adsorbed to bulk metal surfaces and probed with IR radiation.[24] The redshift of the stretching mode could be correlated with differing binding motives and gave a insight into the weakening of the carbon monoxide bond. Since dinitrogen is isoelectronic to carbon monoxide, the Blyholder model can be applied to the investigation of the TM cluster-dinitrogen complexes.

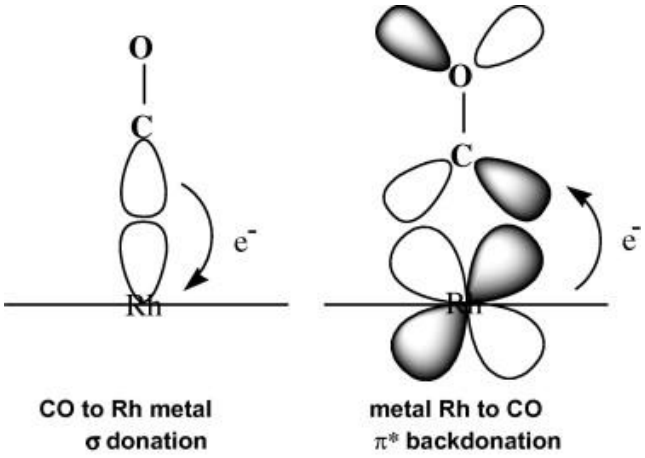


Figure 1.3: [25]The interaction of carbon monoxide with a ruthenium atom as described in the Blyholder model: The first step illustrates the σ-donation of electron density from the carbon towards the ruthenium. The second step shows the back donation of electron density from the ruthenium atom towards the anti-binding π*-orbital of the carbon monoxide.

Dewar, Chatt and Duncanson published a study on the reactions of olefines which resulted in the weakening of the double bond and correlated it with the population of anti-bonding π*-orbitals.[26] The weakening of the bonds was investigated with IR spectroscopy and showed a redshift in coherence with the weakening of the bond. Both models, Blyholder more prevalent in surface physics, Dewar-Chatt-Duncanson in organometallic chemistry, describe a similar phenomenon and build the basis for the study of the activation of molecular nitrogen in this work.

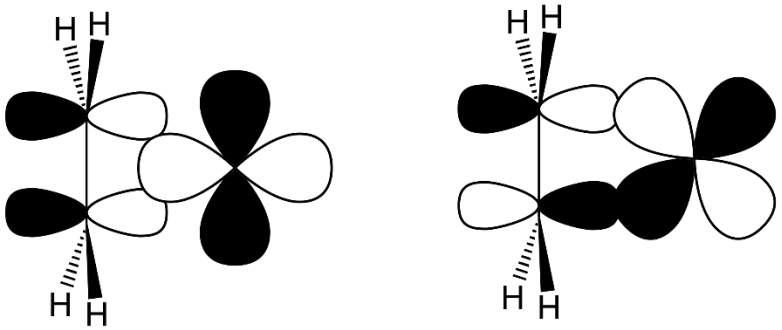


Figure 1.4: [26] The interaction of olefin double bonds with a transition metal atom as described by Dewar, Chatt and Duncanson. The first illustration shows the σ-donation from the binding π-orbital towards the transition metal atom. The second illustration depicts the backdonation of electron density from the transition metal atom towards the anti-binding π*-orbital of the olefine.

On top of the redshift observed in the stretching mode of diatomic absorbents according to the Blyholder model, a secondary effect can be observed in the study of TM cluster-adsorbate complexes. Fielicke et al. studied the redshift of adsorbent molecules in correlation with the charge of the cluster, as well as the cluster's size. The observed redshift is dependent on the charge of the cluster, negatively charged clusters being more effective at donating electron density into the anti-binding orbitals than clusters with no charge or even positive charge. Furthermore, the difference was larger when investigating smaller clusters than larger ones. This effect is called the "charge-dilution-effect". Here it is proposed that the charge relative to the size of the cluster has an impact on the electronic structure in the σ-donor – π-acceptor process and thus on the observed redshift of the stretching mode of the adsorbent.[27,28]

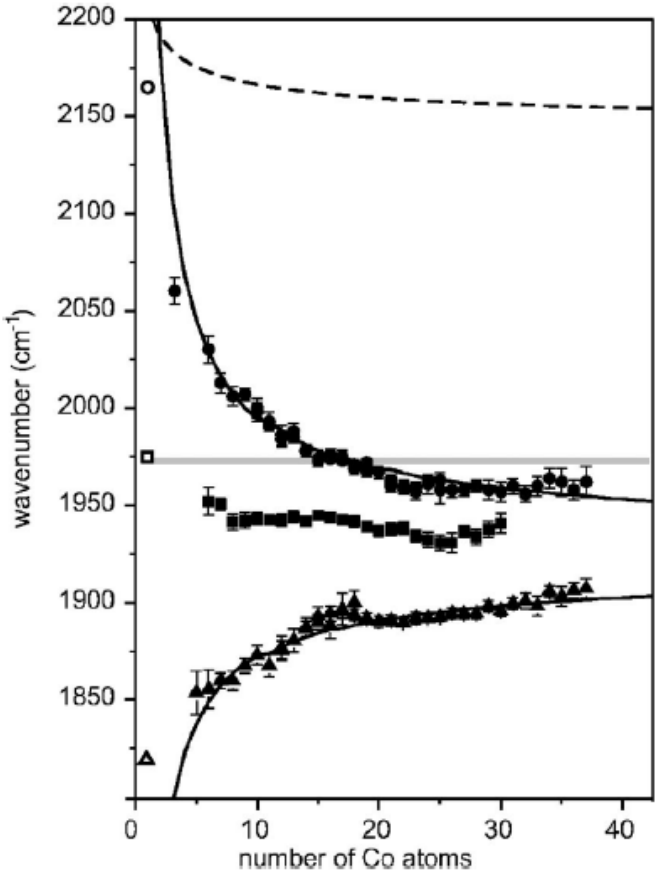


Figure 1.5: [27] Figure taken from Fielecke et al., displaying the IR signal shift depending on the charge state of the cluster – adsorbate complex. Cationic complexes are shown as circles, neutrals as squares, and anions as triangles. The general trend expected by the Blyholder model, as well as the secondary trend of according to the charge-dilution model are illustrated.

Previous studies using a similar experimental setup for cluster generation and tandem cryo-ion traps for the generation and isolation of TM cluster-adsorbate complexes were conducted for a large variety of transition metals.[21–23] The received IR-PD action spectra revealed similar trends in agreement with previously described models. In combination with ab initio quantum chemical modeling, it was also possible to identify single reaction steps, e.g., for the dinitrogen activation on tantalum clusters.

In this work molecular nitrogen size selected TM clusters to further the understanding of elementary steps in the catalytic activation. A focus will be set on the negatively charged clusters as those should be more likely to engage in the σ-donor – π-acceptor mechanism

due to a higher electron density. The results will be compared to previous studies conducted with the same experimental setup to find tendencies in the behavior of the same cluster size, but with a differing electronic structure. Tandem cryo techniques will be used to understand uptake kinetics of nitrogen on the selected cluster and isolation of TM cluster-adsorbate complexes. The isolated complexes will be investigated with IR action spectroscopy. Together with quantum chemical ab-initio modeling an understanding of the geometry, electronic structure of the complex will be studied alongside its' implications on the catalytic process of nitrogen activation.

1.3 Literature

[1] a) W. M. Haynes (Ed.) *CRC handbook of chemistry and physics*. *A ready-reference book of chemical and physical data*, CRC Press, Boca Raton, London, New York, **2017**; b) C. W. Allen, *Astrophysical quantities*, Athlone Pr, London, **1991**.

[2] T. L. Cottrell, *(No Title)* **1954**.

[3] J. B. Howard, D. C. Rees, *Chemical reviews* **1996**, *96*, 2965.

[4] a) D. Fowler, M. Coyle, U. Skiba, M. A. Sutton, J. N. Cape, S. Reis, L. J. Sheppard, A. Jenkins, B. Grizzetti, J. N. Galloway et al., *Philosophical transactions of the Royal Society of London. Series B, Biological sciences* **2013**, *368*, 20130164; b) B. M. Hoffman, D. Lukoyanov, D. R. Dean, L. C. Seefeldt, *Accounts of chemical research* **2013**, *46*, 587.

[5] P. H. Graham, C. P. Vance, *Field crops research* **2000**, *65*, 93.

[6] J. C. Gaby, D. H. Buckley, *Environmental microbiology* **2011**, *13*, 1790.

[7] R. H. Burris, P. W. Wilson **1945**.

[8] A. Hermann, *Phys. Bl.* **1965**, *21*, 168.

[9] M. Appl in *Ullmann's Encyclopedia of Industrial Chemistry*, Wiley-VCH Verlag GmbH & Co. KGaA, Weinheim, Germany, **2000**.

[10] J. W. Erisman, M. A. Sutton, J. Galloway, Z. Klimont, W. Winiwarter, *Nature Geosci* **2008**, *1*, 636.

[11] Badische Anilin- und Soda-Fabrik, DE235421C, **1908**.

[12] F. Haber, R. Le Rossignol, US971501, **1910**.

[13] M. Capdevila-Cortada, *Nat Catal* **2019**, *2*, 1055.

[14] G. Ertl, *Catalysis Reviews Science and Engineering* **1980**, *21*, 201.

[15] G. Ertl, *Reactions at solid surfaces*, Wiley, Hoboken, N.J., **2009**.

[16] G. Ertl, S. B. Lee, M. Weiss, *Surface Science* **1982**, *114*, 515.

[17] J. Humphreys, R. Lan, S. Tao, *Adv Energy and Sustain Res* **2021**, *2*, 2000043.

[18] a) H. Liu, *Chinese Journal of Catalysis* **2014**, *35*, 1619; b) Y. Tanabe, Y. Nishibayashi, *Coordination Chemistry Reviews* **2013**, *257*, 2551.

[19] J. Huang, M. Yuan, X. Li, Y. Wang, M. Li, J. Li, Z. You, *Applied Catalysis A: General* **2021**, *615*, 118058.

[20] a) M. B. Knickelbein, *Annual review of physical chemistry* **1999**, *50*, 79; b) G. E. Johnson, R. Mitrić, V. Bonačić-Koutecký, A. W. Castleman, *Chemical Physics Letters* **2009**, *475*, 1; c) S. M. Lang, T. M. Bernhardt, *Phys. Chem. Chem. Phys.* **2012**, *14*, 9255.

[21] S. Dillinger, M. P. Klein, A. Steiner, D. C. McDonald, M. A. Duncan, M. M. Kappes, G. Niedner-Schatteburg, *The journal of physical chemistry letters* **2018**, *9*, 914.

[22] S. Dillinger, J. Mohrbach, J. Hewer, M. Gaffga, G. Niedner-Schatteburg, *Phys. Chem. Chem. Phys.* **2015**, *17*, 10358.

[23] D. V. Fries, M. P. Klein, A. Steiner, M. H. Prosenc, G. Niedner-Schatteburg, *Phys. Chem. Chem. Phys.* **2021**, *23*, 11345.

[24] G. Blyholder, *J. Phys. Chem.* **1964**, *68*, 2772.

[25] J. E. House, *Descriptive Inorganic Chemistry*, Elsevier Science & Technology, San Diego, **2016**.

[26] J. Chatt, L. A. Duncanson, *J. Chem. Soc.* **1953**, 2939.

[27] A. Fielicke, P. Gruene, G. Meijer, D. M. Rayner, *Surface Science* **2009**, *603*, 1427.

[28] A. Fielicke, G. von Helden, G. Meijer, D. B. Pedersen, B. Simard, D. M. Rayner, *The Journal of chemical physics* **2006**, *124*.

2 Experimental setup and quantum chemical methods

The study of compounds in the gas phase at cryo temperatures requires experimental techniques to transfer samples into the gas phase. Experiments require both gas phase reactions at controlled temperatures and interaction with tunable light sources and analyzing the samples using mass spectrometry. In this chapter the experimental and theoretical methods, from sample generation to the final analysis are explained in detail.[1]

2.1 Laser Vaporization Cluster Source

For the generation of transition metal clusters in the gas phase, we use a home build Laser Vaporization Cluster Source (LVAP). This ion source has first been described by Bondybey, English[2] and Smalley.[3] The ion source consists of three main components (see figure 2.1); the piezoelectric valve[4], the expansion block and the expansion channel. It uses a metal or metal alloy target of 13 mm diameter and 0.1-0.5 mm thickness which is set up on a rotating mount. The target is irradiated with second harmonic generation Nd:YAG Laser (Innolas, Spitlight 300, 20 Hz, 25 mJ/pulse). The laser pulses generate a plasma containing neutral, cationic, and anionic species, while the rotation of the target provides continuous provision of a fresh metal surface within the circular trace of the target. After a set delay time, the piezoelectric valve opens for 40 µsec. The piezoelectric valve has a backing pressure of 12-15 bar, thus generating a short gas pulse expanding into the vacuum of the chamber. The metal plasma is cooled by this supersonic expansion, and clusters are formed in the expansion channel. The cluster size can be varied between 2 and 40 atoms by optimizing the backing pressure of the piezoelectric valve, the power of the ablation laser, the delay between irradiation and gas expansion as well as the applied

source voltages. It must be noted that no further ionization steps are required and both cationic and anionic clusters can be generated.

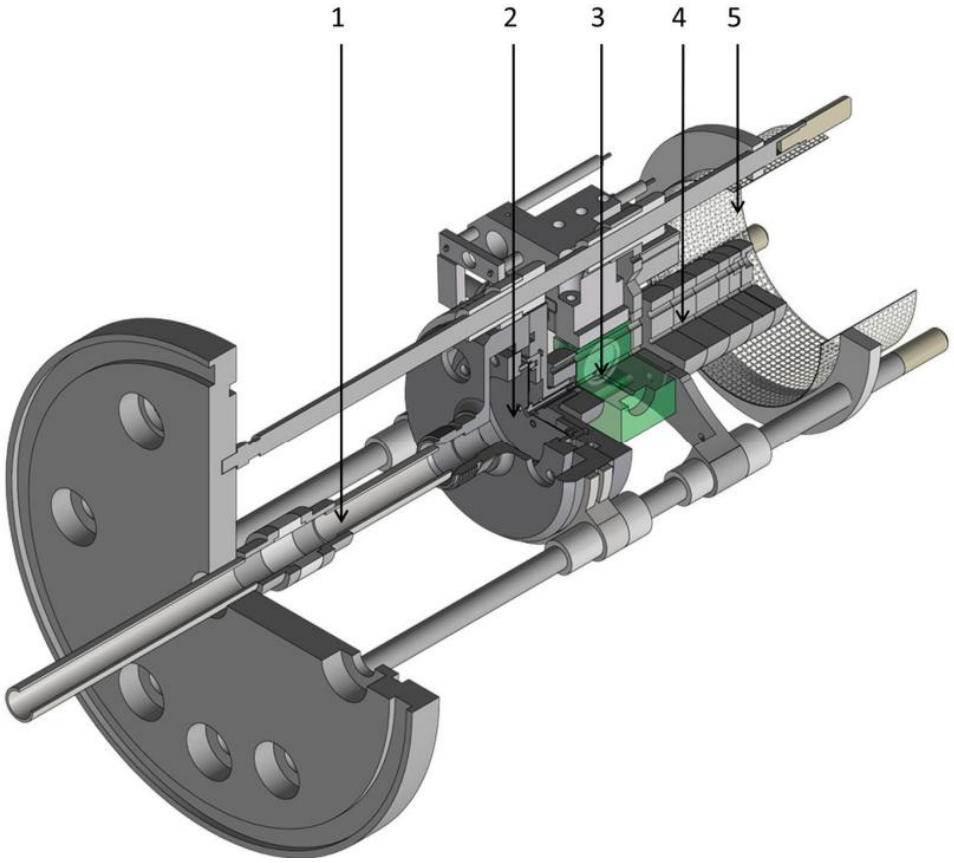


Figure 2.1: Schematic design of our LVAP source: expansion gas line (1), piezoelectric valve (2), expansion block (3), expansion channel (4), mesh (5).

Due to the piezoelectric valve used in this setup, we allow the utilization of relatively small metal or alloy targets in this ion source. Therefore, it is possible to investigate metal clusters of metal that are not widely available, such as mono isotopic ^{102}Ru or ^{58}Ni (Oak Ridge National Laboratory).

2.2 Electrospray Ionization Source

Electrospray Ionization (ESI) is a method based on developments by Zeleny in 1917[5] and was first realized by Dole in 1968.[6] The technique in combination with quadrupole mass spectrometry was widely established by Fenn[7], who has been awarded with a noble prize for his work in 2002.[8]

ESI is considered to be a "soft" ionization method and today is widely used for analysis of biomolecules[9], organic compounds[10], catalytic intermediates[11] and organometallic complexes[12]. The following paragraph will describe the technique used for the Apollo II ESI source by Bruker Daltonics. The general principle is applicable to most other ESI sources with minor variations in the design.

The ESI source has two major components, the sprayer assembly, generating the spray containing the ions in the ESI chamber and the transfer capillary bringing the ions into the gas phase. In the first step the substrate must be solved in an organic solvent, reaching from apolar Dichloromethane (DCM) to polar Water (H_2O). In the solvated states the ionic states of the substrates are supported by the solvation. The substrate is transferred to the sprayer needle. High voltage is applied from the needle into the ESI chamber, resulting in the attraction of anionic/cationic species towards the tip of the needle. The coulomb force of the ions results in the formation of a Taylor cone[13] at the tip of the needle, where little droplets containing the ions are evaporated into the chamber. The spraying process is aided by a nebulizer gas with is applied at the tip of the needle. The solvent molecules evaporate, leading to smaller droplets. The surface tension holding the droplets together has to withstand the rising Coulomb force with decreasing droplet size.(see figure 2.2) The specific point at which the droplets start to deteriorate is called the Reighley limit.[14] There are two mechanisms describing the following process: The ion evaporation model[15] expects single ions to be ejected directly into the gas phase out of relatively big droplets. The charge residue model[16] suggests successive Coulomb explosions of the droplets leading to a single ion per droplet. The single ions shed the remaining solvent molecules

and are effectively transferred into the gas phase. Both models are applicable depending on the type of molecule and solvent.

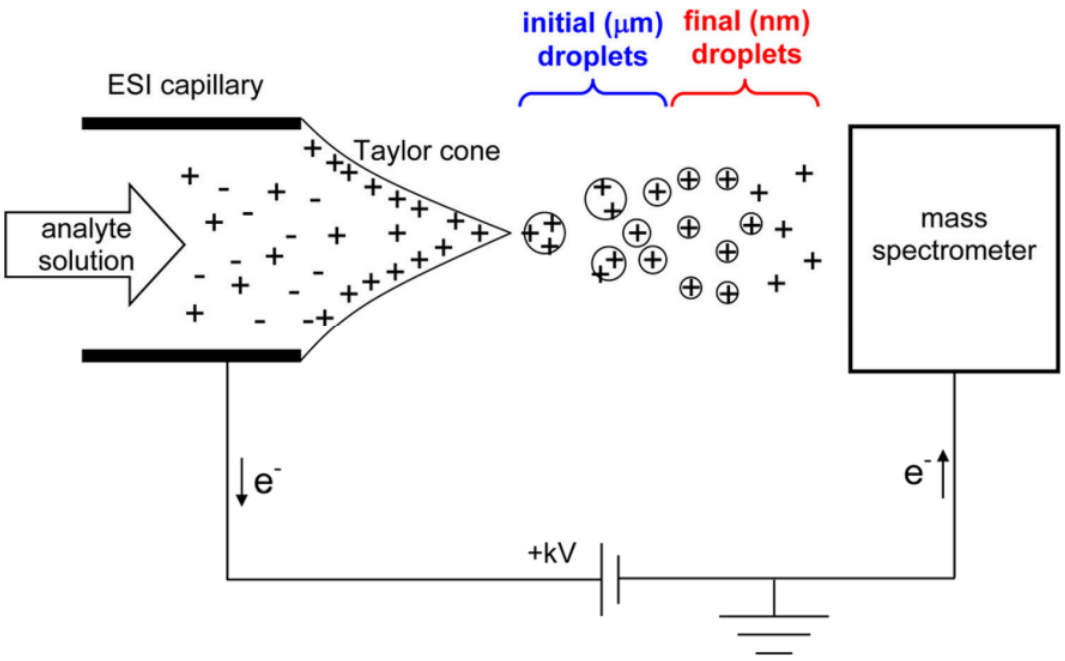


Figure 2.2:[17] Schematic process occurring at the ESI needle in an electric field, showing the Taylor cone and the charged droplets with decreasing size during the ESI process.

The ESI chamber at atmospheric pressure is connected to the evacuated mass spectrometer with a transfer capillary (see figure 2.3). The transfer capillary is heated to ca. 180 °C and is flushed with heated Nitrogen (N_2) in order to help with the evaporation of the surplus solvent molecules. The ions are transferred using an electric field which is applied between the end caps of transfer capillary.

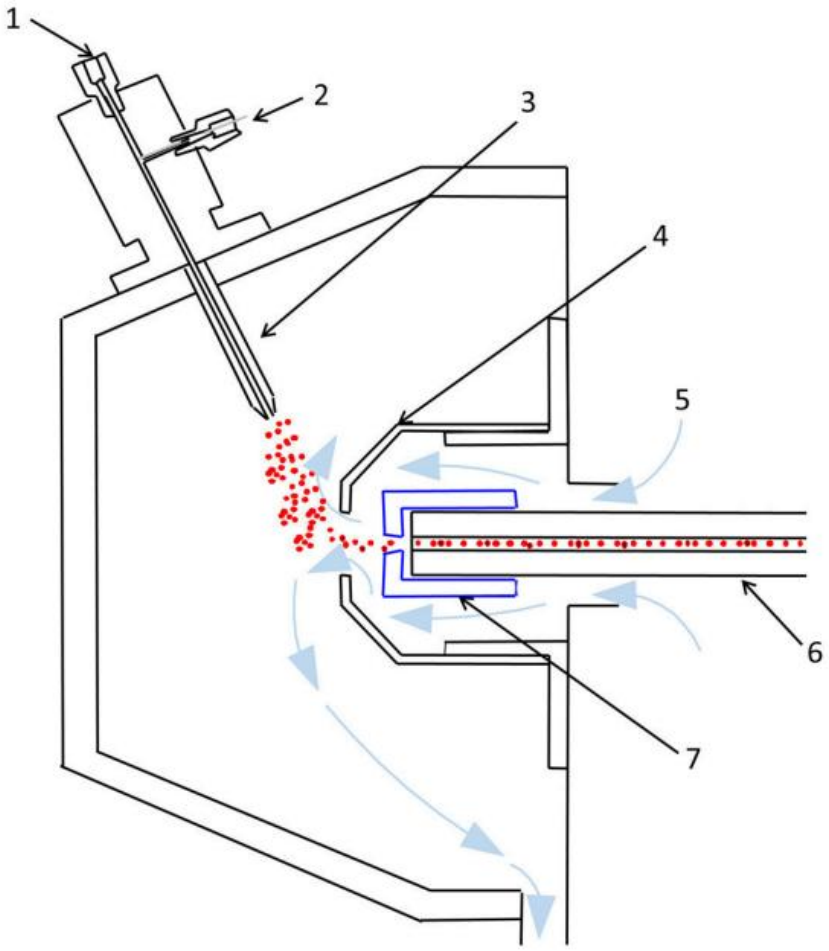


Figure 2.3[18]**:** Schematic design of the Apollo II ESI source by Bruker Daltonics. Syringe inlet (1), nebulizer gas inlet (2), sprayer needle (3), spray shield (4), heated dry gas (5), transfer capillary (6), capillary cap (7).

The Apollo II ESI source, which is used in the FRITZ setup (see chapter 2.4), also contains an accumulation hexapole. It has two purposes, first it sets up the ions onto a narrow axis, improving the handling of the ion beam in further experimental steps, second it can be used to accumulate ions and releasing them in a concentrated pulse. The pulse setting is improving the handling for signal detection, and it is a possibility to improve the relatively low ion yield of an ESI source compared to the LVAP source. In the used setup the accumulation function is not essential due to the integrated hexapole cryo trap, so the source is generally set to continuous operation unless described otherwise.

2.3 Fourier Transform Ion Cyclotron Resonance Mass Spectrometry

Ion cyclotron resonance mass spectrometry relies on the ion cyclotron resonance of ions observed in a magnetic field. The effect was first described by Lawrence in 1930.[19] The angular frequency of the ions in the magnetic field are described by:

$$\omega = 2\pi f = \frac{zeB}{m} \tag{2.1}$$

With ω being the angular velocity of the ion, f the angular frequency, z the number of charges either positive or negative, e the elementary charge (1.602 x 10^{-9} C), B the magnetic field strength and m the mass of the ion. It is therefore possible to relate the angular frequency with a mass to charge ratio (m/z).

$$\frac{m}{z} = \frac{eB}{2\pi f} \tag{2.2}$$

The relation of the angular frequency and the mass to charge ration is the foundation of Fourier transform ion cyclotron resonance mass spectrometry. The technique was established by Comisarow and Marshall in the early 1950s.[20] In order to accomplish the trapping, ICR cells or Penning traps were constructed. The following paragraph will describe the design of the Bruker infinity cell used in this thesis' experimental setup.

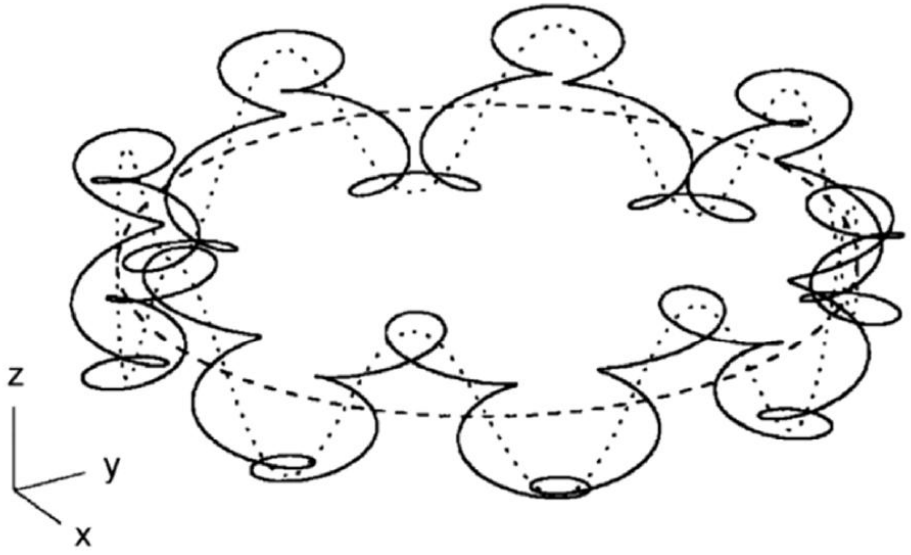


Figure 2.4:[21] Cyclotron resonance ion motion inside the ICR cell (solid line), comprising of the magnetron motion (dashed line) and the trapping motion (dotted line)

The ICR cell is constructed out of six plates, two trapping plates, two excitation plates and two detection plates. The trapping plates contain the ions within the z-axis in the magnetic field. The plates are intersected into symmetric compartments which are subject to a decreasing electrostatic field. This design leads to an apparently infinite length on the z-axis for the trapped ions, leading to minimal interference of the electrostatic trapping with the cyclotron resonance motion. The excitation plates enable the resonant excitation of the trapped ions using a rf-pulse. The excitation is elevating the trapped ions to higher orbits making detection by the third pair of plates, the detection plates, possible. The ions on these higher orbits pass closer to the detection plates on their circular motion around the z-axis. They induce an image current on the detection plates which is amplified, Fourier transformed and read out to obtain a mass spectrogram. It is also possible to eject ions with a determined mass-to-charge ratio out of the ICR cell using the excitation plates. The resonant rf-pulse is used to excite specific ions to unstable orbits, effectively ejecting them from the ICR cell.

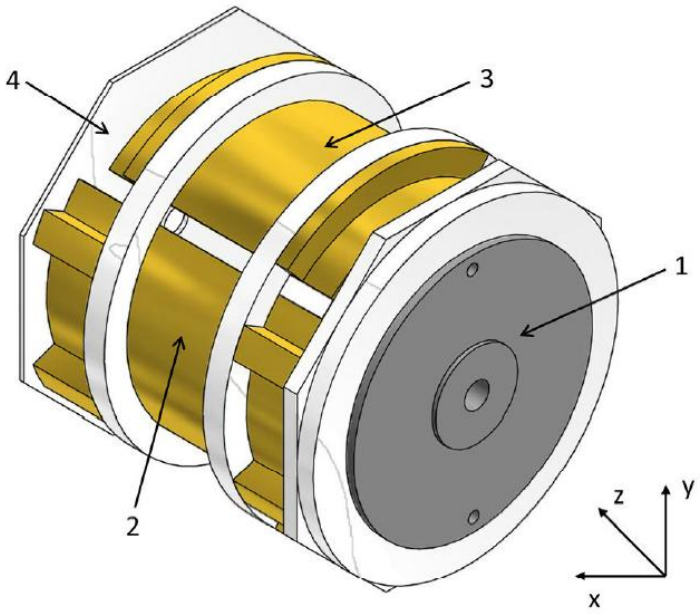


Figure 2.5: ICR infinity cell by Bruker Daltonics, comprised of the front trapping plate (1), excitation plates (2), detection plates (3), and the back trapping plate (4)

2.4 The FT-ICR mass spectrometer FRITZ

The Fouriertransform Reactive Investigation Test Zoo (FRITZ) is a modified Bruker Apex Ultra FT-ICR mass spectrometer. It assembles two ion sources, a commercial Apollo II electrospray ionization (ESI) source (Bruker) and a home-built Laser vaporization (LVAP) cluster source (described in chapters 2.1 and 2.2). Both ion sources are assembled on a 90° angle towards the magnetic field axis. The central chamber on the magnetic field axis contains a homebuilt quadrupole bender assembly, which guides the generated ions onto the principal experimental axis. Stacks of homebuilt ion optics are installed on three sides of the bender assembly, two for incoming ions, one for setting them onto the path for further use. The ion sources can be separated from the vacuum system with home-built gate valves, allowing for maintenance work and modifications on the ion sources without impeding the rest of the experiment. This setup allows for swift changes of the ion source, limiting the downtime of the experiment due to the switching of ion sources and maintenance.

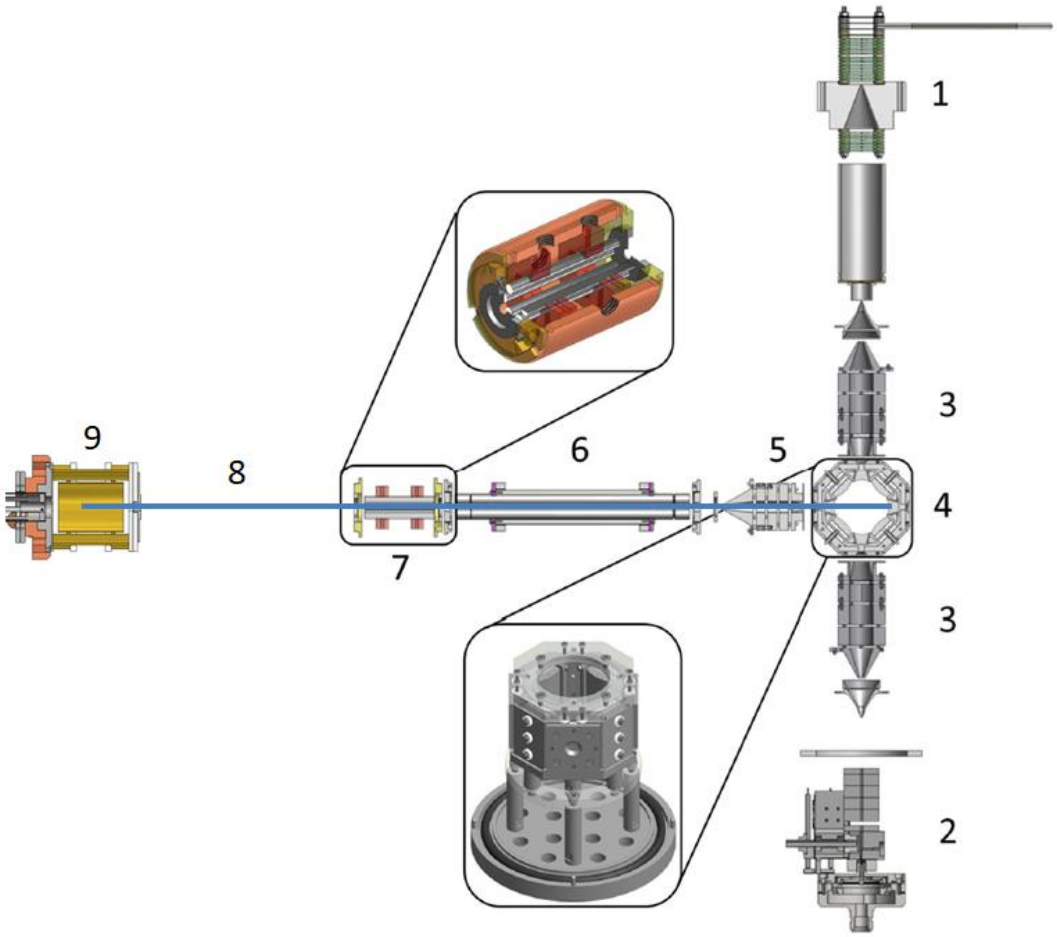


Figure 2.6: Schematic setup of the FRITZ setup from the sources to the reaction cell, with the Apollo II ESI source (1), the LVAP cluster ion source (2), ion optics (3)and (5), the quadrupole ion bender (4), the quadrupole mass filter (6), the hexapole cryo ion trap (7), the magnetic field axis (8) and the ICR cell (9). The distances are not to scale.

The next vacuum chamber contains the quadrupole mass filter and cryo hexapole reaction chamber. The quadrupole mass filter is part of the original Apex Ultra setup and is handled by the commanding software provided by Bruker. It can be set to allow a wide range of mass-to-charge ratios to pass, as well as selecting single kinds of ions. The separation step is essential for the following experimental techniques which are reliant on the exclusion of adducts (e.g., oxygen adducts on clusters or solvent adducts on TM-complexes).

The cryo hexapole reaction chamber consists of the Bruker built hexapole ion trap which has been equipped with a cryogenic closed circuit helium cooling head. (Sumitomo SRDK-101E with a HC-4E compressing unit). The hexapole trap can be cooled down to 15 K. The temperature is monitored by two temperature sensors (LakeShore, CernoxTM CX-

1060-CO-HT-P-1.4M) Two heater resistors (Cartridge Heater, Janis Research, R = 50 Ω) allow for adjusting the temperature in the hexapole cell. Two gas inlets provide buffer and/or reaction gas to the chamber. The pressure is observed by hot cathode pressure gauge. The reaction time in the hexapole cell can be set from 0 to 30 seconds. This setup allows for the studies of isothermal cryo kinetics explained further in chapter 2.2.2.

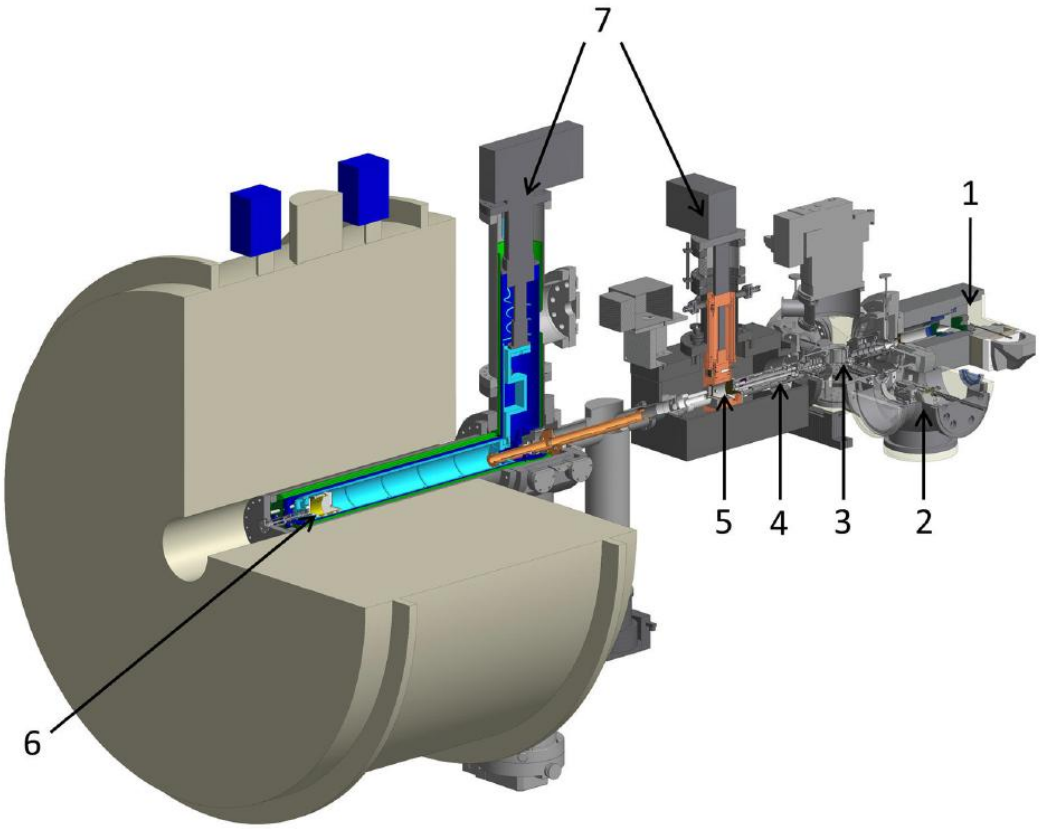


Figure 2.7: Schematic design of the FRITZ setup at TUK, with the Apollo II ESI source (1), located opposite the LVAP cluster ion source (2), but displayed linear for clarity, the quadrupole ion bender assembly (3), the quadrupole mass filter (4), the hexapole reaction cell (5), the ICR cell (6) and the two closed circuit Helium cryostats (7)

After the hexapole reaction cell, the ions are accelerated into the ultra-high vacuum of the ICR chamber. The ultra-high vacuum section is separated by a beam valve. The ICR cell is located in the center of a superconducting magnet (5T). The ICR cell is connected to a cryostat, allowing for temperatures as low as 6.5 K, measured at the back plate of the cell. The function of the ICR cell is described in chapter 2.3 It allows for both selecting and trapping ions in the cell. Additionally, reaction gases can be introduced into the ultra-high

vacuum chamber, making the ICR cell a second reaction cell in the process. The ions can then be irradiated with an available light source, allowing for action spectroscopy, e.g., IR-PD (described in chapter 2.6).

2.5 OPO/OPA IR Laser system

The IR laser setup is installed at the FRITZ lab at TUK. It is made up of two major components, the pump laser and the OPA/OPA system.

The Continuum Powerlight DLS 8000 is a Nd:Yag laser with a fixed frequency at 1064 nm. A seed laser is used to stabilize the pulses and shorten the pulse width to 5-7 ns. It provides laser pulses with a power between 500 and 700 mJ/puls at a 10 Hz frequency. The beam has a width of 8 mm with an even distribution to prevent local energy spikes which may damage the following crystals in the OPO/OPA system. We monitor the quality of the seed laser using a fast photodiode for the pulse width and seeder stability, a camera for the beam profile and a power meter for the energy per pulse.

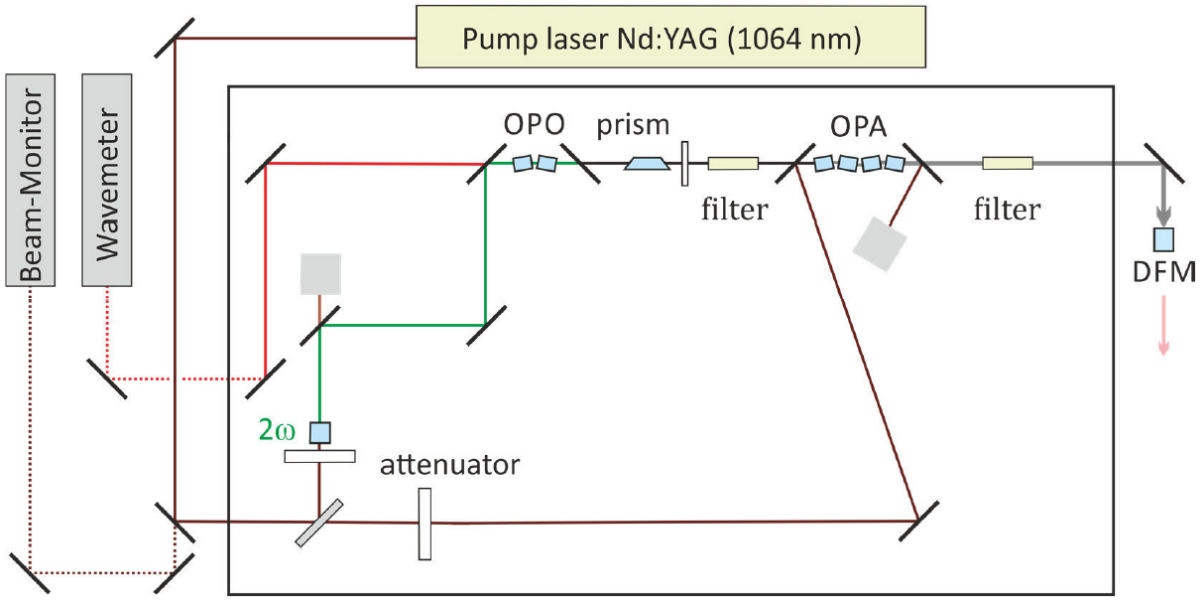


Figure 2.8: Schematic setup of the IR OPO/OPA laser system by LaserVision

The Optical Parametric Oscillator/Amplifier (OPO/OPA) IR laser system is a product of LaserVision. In a first step the 1064 nm fundamental beam of the seed laser is split into

one third lead to the oscillator and two thirds lead to the amplifier. The beam entering the oscillator is frequency doubled (second harmonic generation SHG) by a potassium titanyl phosphate (KTP) crystal and the remaining fundamental is dumped. The cavity of the oscillator is set by the output mirror and either the back mirror or the tuning mirror and grating. When using the tuning mirror and grating as the resonator, the laser is operated in the narrowband mode, which provides a narrower bandwidth of the output wavelength. On the other hand, using the back mirror for the resonator sets the laser to the broadband mode, providing a wider output wavelength. We have found that the broadband mode provides better energy stability when the laser is tuning through frequencies at operation. For this reason, we are using the broadband mode unless states otherwise. Two KTP crystals are positioned in the cavity of the oscillator. They split the 532 nm pump radiation into Signal 1 and Idler 1 waves. The frequency of these waves can be tuned by changing the angle of the two crystals in the cavity. Signal 1 and Idler 1 leave the oscillator and Signal 1 is dumped using a silicone filter. Idler 1 is guided to the OPA stage. The OPA consists of four potassium titanyl arsenate (KTA) crystals. Here the incoming Idler 1 wave is overlapped with the remaining two thirds of the fundamental 1064 nm wave. This leads to the generation of Signal 2 and Idler 2 waves. The remaining fundamental is dumped and the two waves, Signal 2 vertically polarized and Idler 2 horizontally polarized, are emitted. If we want to use the Signal 2 or Idler 2 radiation, a filter can be installed to pass either the horizontal or vertical polarized wave. Additionally, a difference frequency generation (DFM) stage can be equipped. It contains a silver gallium diselenide ($AgGaSe_2$) crystal. Here both Signal 2 and Idler 2 waves are overlapped on the crystal, generating the DFM wave.[22] The remaining Idler 2 radiation is dumped by a zinc selenide (ZnSe) filter.

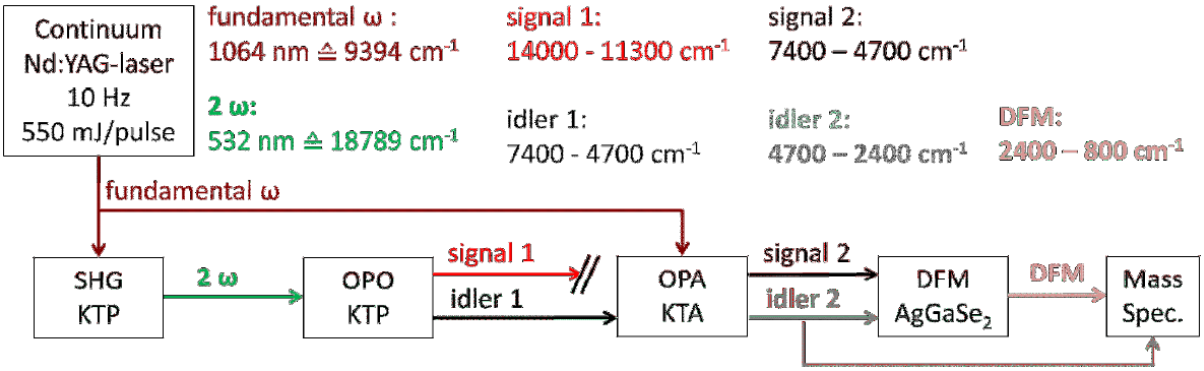


Figure 2.9: Overview of nonlinear optical processes and frequency conversions within the OPO/OPA laser system yielding the respective IR photons.

2.6 Infrared-multiple photon dissociation

Infrared (IR) absorption spectra are a valuable tool in the characterization of chemical compounds. However, classical absorption spectroscopy methods are not feasible in the gas phase due to the low particle density. For this reason, action spectroscopy methods are used for gas phase IR spectroscopy. In this case we are not focusing on the effect the sample has on the IR light, but rather what effect the IR light has on the sample. Due to the low particle density, tunable laser systems are used to irradiate the samples.

IR-(multiple) photon dissociation action spectroscopy is an established method for gas phase spectroscopy.[23] If we irradiate an ion in the gas phase with an IR photon, the ion is able to absorb the photon if the photon energy matches a vibrational mode of the ion. The vibrational energy is then redistributed throughout the ion.[24] After the redistribution it is possible the resonantly excite the vibrational mode again. The redistributed energy throughout the ion will cause the dissociation of the weakest bond of the structure.[25] The dissociation leads to a change of the mass to charge ratio of the ion in the gas phase and thus can be detected. The IR(M)PD spectrum can be obtained by plotting fragmentation efficiency against the IR-laser frequency.

$$frag.eff. = \frac{\sum_i I_i^{fr}}{\sum_i I_i^{fr} + \sum_i I_i^{p}} \quad (2.3)$$

With I_i^{fr} : intensity of the fragment ions

and I_i^{p} : intensity of the parent ions

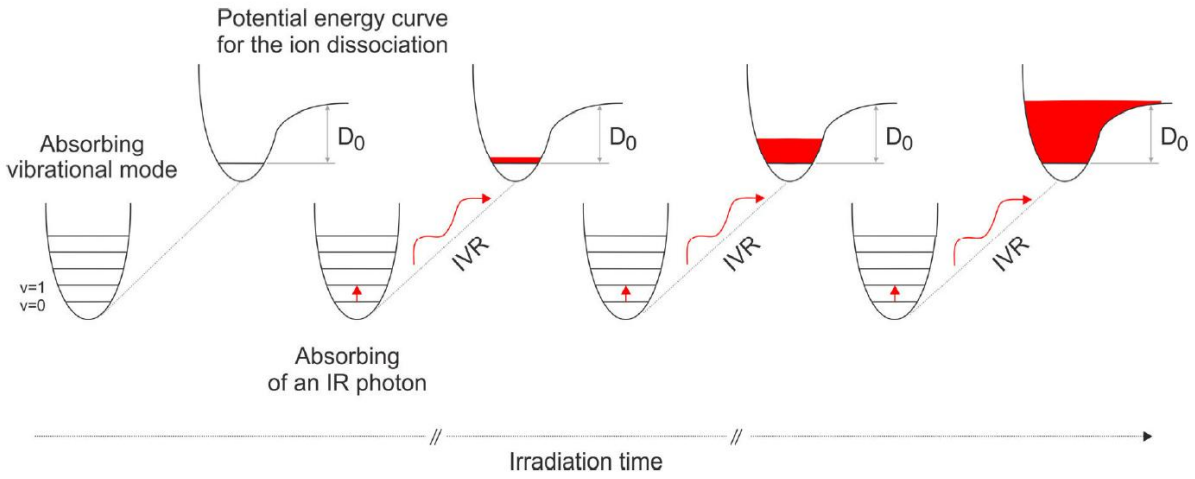


Figure 2.10:[26] Schematic mechanism of the IRMPD process. An IR photon is absorbed, and the energy is distributed via IVR into the system. This process can repeat multiple times, until the dissociation threshold is surpassed and the ion dissociates.

In order for this method to work, a weakly bound adduct is needed as a messenger. This can either be a weakly bound ligand which is usually the case for TM complexes, or a physisorbed tag. Here a common technique is using an argon atom which can be tagged to a ion at low temperatures.[27] The noble gas atom is not altering the structure of the sample and is easily evaporated in the IR-PD process.

2.7 Quantum chemical methods

The interpretation of IR-PD spectra requires intensive study of the sample geometry and of the resulting vibrational frequencies associated with the geometric features. Quantum chemical calculations determine energetically favorable geometries, as well as the vibrational energies of these structures and thus make it an invaluable tool in the interpretation of IR-PD spectra.[28,29] In our experimental setup, the samples are cryogenically cooled in the gas phase, making a comparison to calculated geometries even more attractive, since inaccuracies due to packing or solvation effects are excluded.

The fundamental principle of the density functional theorem (DFT) approach is the availability of all information regarding a molecule in its' electron density $\rho\ (\vec{r})$, as described by Thomas and Fermi.[30] This principle was proven by Hohenberg and Kohn in their first theorem.[31] In their second theorem they showed the applicability of the variational principle to the approach which led to the energy minimization as described by Kohn and Sham.[32] This leads to the following expression for the energy as a function of the of the electron density:

$$E(\rho) = T_0(\rho) + \int dr\rho(\vec{r}) \left(V_{eff}(\vec{r}) + \frac{1}{2}\varphi(\vec{r}) \right) + E_{XC}(\rho) \qquad (2.4)$$

$T_0(\rho)$	kinetic energy
$V_{eff}(\vec{r})$	effective potential
$\varphi(\vec{r})$	Coulomb potential
$E_{XC}(\rho)$	exchange correlation energy

The corresponding Kohn-Sham wavefunction is a single Slater determinant and is constructed from a set of orbitals that are the lowest energy solution to:

$$\left(-\frac{h^2}{2m}\nabla^2 + V_{eff}(\vec{r})\right)\phi_i(r) = \varepsilon_i\phi_i(r) \quad (2.5)$$

$\phi_i(r)$ Kohn-Sham orbital i

ε_i orbital energy

The electron density of the system can be described as:

$$\rho(\vec{r}) = \sum_i^N |\phi_i(r)|^2 \quad (2.6)$$

The exchange correlation energy is the contains all the unknown factors of the function and has significant influence on the results of the calculation. Therefore, it is a key component to reach a good approximation using DFT calculation. Common approach to estimate the exchange correlation energy are the local density approximation (LDA)[29] or the generalized gradient approximation (GGA).[33] They are used in hybrid functionals which have proven to deliver accurate results in broad range of applications.

To find the energetically most favorable structures, a number of structures must be calculated to scan the potential energy surface.

2.8 Literature

[1] J. H. Gross, *Mass spectrometry: a textbook*, Springer Science & Business Media, **2006**.

[2] a) V. E. Bondybey, J. H. English, *The Journal of chemical physics* **1981**, *74*, 6978; b) C. Berg, T. Schindler, G. Niedner-Schatteburg, V. E. Bondybey, *The Journal of chemical physics* **1995**, *102*, 4870.

[3] a) S. Maruyama, L. R. Anderson, R. E. Smalley, *Review of scientific instruments* **1990**, *61*, 3686; b) T. G. Dietz, M. A. Duncan, D. E. Powers, R. E. Smalley, *The Journal of chemical physics* **1981**, *74*, 6511.

[4] D. Proch, T. Trickl, *Review of scientific instruments* **1989**, *60*, 713.

[5] J. Zeleny, *Physical review* **1917**, *10*, 1.

[6] M. Dole, L. L. Mack, R. L. Hines, R. C. Mobley, L. D. Ferguson, M. B. Alice, *The Journal of chemical physics* **1968**, *49*, 2240.

[7] J. B. Fenn, M. Mann, C. K. Meng, S. F. Wong, C. M. Whitehouse, *Science* **1989**, *246*, 64.

[8] J. B. Fenn, *Angewandte Chemie International Edition* **2003**, *42*, 3871.

[9] R. Aebersold, D. R. Goodlett, *Chemical reviews* **2001**, *101*, 269.

[10] B. N. Pramanik, P. L. Bartner, U. A. Mirza, Y.-H. Liu, A. K. Ganguly, *Journal of Mass Spectrometry* **1998**, *33*, 911.

[11] a) D. Schröder, *Accounts of chemical research* **2012**, *45*, 1521; b) K. L. Vikse, Z. Ahmadi, J. S. McIndoe, *Coordination Chemistry Reviews* **2014**, *279*, 96.

[12] V. Katta, S. K. Chowdhury, B. T. Chait, *Journal of the American Chemical Society* **1990**, *112*, 5348.

[13] a) M. S. Wilm, M. Mann, *International Journal of Mass Spectrometry and Ion Processes* **1994**, *136*, 167; b) G. I. Taylor, *Proceedings of the Royal Society of London. Series A. Mathematical and Physical Sciences* **1964**, *280*, 383.

[14] Rayleigh, *The London, Edinburgh, and Dublin Philosophical Magazine and Journal of Science* **1882**, *14*, 184.

[15] a) B. A. Thomson, J. V. Iribarne, *The Journal of chemical physics* **1979**, *71*, 4451; b) J. V. Iribarne, B. A. Thomson, *The Journal of chemical physics* **1976**, *64*, 2287.

[16] a) A. T. Iavarone, E. R. Williams, *Journal of the American Chemical Society* **2003**, *125*, 2319; b) G. Schmelzeisen-Redeker, L. Bütfering, F. W. Röllgen, *International Journal of Mass Spectrometry and Ion Processes* **1989**, *90*, 139.

[17] L. Konermann, E. Ahadi, A. D. Rodriguez, S. Vahidi, *Unraveling the mechanism of electrospray ionization*, **2013**, ACS Publications.

[18] Bruker Daltonics GmbH (Ed.), **2006**.

[19] a) E. O. Lawrence, M. S. Livingston, *Physical review* **1932**, *40*, 19; b) E. O. Lawrence, N. E. Edlefsen, *Science* **1930**, *72*, 376; c) E. O. Lawrence, D. Cooksey, *Physical review* **1936**, *50*, 1131.

[20] a) H. Sommer, H. A. Thomas, J. A. Hipple, *Physical review* **1951**, *82*, 697; b) A. G. Marshall, *International Journal of Mass Spectrometry* **2000**, *200*, 331; c) A. G. Marshall, C. L. Hendrickson, G. S. Jackson, *Mass spectrometry reviews* **1998**, *17*, 1; d) M. B. Comisarow, A. G. Marshall, *Chemical Physics Letters* **1974**, *26*, 489; e) M. B. Comisarow, A. G. Marshall, *Chemical Physics Letters* **1974**, *25*, 282.

[21] L. Schweikhard, J. Ziegler, H. Bopp, K. Lützenkirchen, *International Journal of Mass Spectrometry and Ion Processes* **1995**, *141*, 77.

[22] M. Gerhards, *Optics communications* **2004**, *241*, 493.

[23] N. C. Polfer, *Chemical Society Reviews* **2011**, *40*, 2211.

[24] Y. M. E. Fung, F. Kjeldsen, O. A. Silivra, T. W. D. Chan, R. A. Zubarev, *Angewandte Chemie International Edition* **2005**.

[25] a) D. W. Lupo, M. Quack, *Chemical reviews* **1987**, *87*, 181; b) E. R. Grant, P. A. Schulz, A. S. Sudbo, Y. R. Shen, Y.-T. Lee, *Physical Review Letters* **1978**, *40*, 115.

[26] J. Roithová, *Chemical Society Reviews* **2012**, *41*, 547.

[27] a) M. Z. Kamrath, E. Garand, P. A. Jordan, C. M. Leavitt, A. B. Wolk, M. J. van Stipdonk, S. J. Miller, M. A. Johnson, *Journal of the American Chemical Society* **2011**, *133*, 6440; b) N. R. Walker, R. S. Walters, M.-K. Tsai, K. D. Jordan, M. A. Duncan, *The Journal of Physical Chemistry A* **2005**, *109*, 7057; c) A. B. Wolk, C. M. Leavitt, E. Garand, M. A. Johnson, *Accounts of chemical research* **2014**, *47*, 202.

[28] a) R. G. Parr, W. Yang, *Annual review of physical chemistry* **1995**, *46*, 701; b) A. Szabo, N. S. Ostlund, *Modern quantum chemistry: introduction to advanced electronic structure theory*, Courier Corporation, **1996**.

[29] W. Kohn, A. D. Becke, R. G. Parr, *The journal of physical chemistry* **1996**, *100*, 12974.

[30] a) *The calculation of atomic fields*, Cambridge University Press, **1927**; b) E. Fermi, *Zeitschrift für Physik* **1928**, *48*, 73.

[31] P. Hohenberg, W. Kohn, *Physical review* **1964**, *136*, B864.

[32] W. Kohn, L. J. Sham, *Physical review* **1965**, *140*, A1133.

[33] a) A. D. Becke, *The Journal of chemical physics* **1993**, *98*, 1372; b) A. D. Becke, *The Journal of chemical physics* **1992**, *96*, 2155.

3 Influence of the charge state on the N_2 adsorption on size selected cobalt cluster ions in isolation

Christopher Wiehn[a,b], Maximilian Luczak[a,c] , Katharina Rediger[a] and Gereon Niedner-Schatteburg[a,d]

[a]Department of Chemistry, RPTU, 67663 Kaiserslautern, Germany

[b]present address: Defense Logistics Agency, Rhine Ordnance Barracks, 67663 Kaiserslautern, Germany

[c] present address: Math2Market GmbH, 67655 Kaiserslautern, Germany

[d]State Research Center OPTIMAS, RPTU, 67663 Kaiserslautern, Germany

3.1 Preamble

The experiments in this work have been conducted by Maximilian Luczak and Christopher Wiehn in equal parts at RPTU Kaiserslautern's FRITZ lab. The quantum chemical models have been performed by Christopher Wiehn, using Gaussian 16 software package run on the RPTU Kaiserslautern computing center. The results were discussed among Maximilian Luczak, Christopher Wiehn and Prof. Gereon Niedner-Schatteburg. The following paper was drafted by Maximilian Luczak and Gereon Niedner-Schatteburg.

3.2 Abstract

In this study we presented the IR-PD spectra of adsorbed dinitrogen on anionic Cobalt clusters with a size range from 11 to 20 atoms. The recorded spectra reveal a trend in accordance with both the Blyholder and charge-dilution model. We found an unexpected rise in spin multiplicity upon N_2 uptake suggested by DFT calculations which can be explained with previous XMCD studies concerning icosahedral 3d clusters in the gas phase. Further on a significant deviation from the trend concerning the redshift of the IR-PD signals was found for $[Co_{20}]^-$ which connects with the isotropic polarizability of the

cluster. We compared the IR-PD spectra of both cationic and anionic cluster species displaying inverted behavior concerning the charge state. From the fitted results we predict the signal frequency of a N_2 absorbed to a neutral Cobalt cluster surface.

3.3 Introduction

Often, heterogeneously catalyzed multistep reactions, as e.g. the Haber Bosch process, find the initial bond activation as the rate determining step [1], and it starts from adsorbate catalyst complexes as precursor states [1]. Cluster studies provide insights into transition metal (TM) – adsorbate interactions which are complementary to bulk surface studies.[2]

Carbon monoxide (CO) adsorption to the surfaces of transition metal has been characterized intensely by kinetic studies.[3] Observed CO stretching mode frequency shifts have revealed some evidence on prospective coordination sites, namely the on top (μ_1), on bridge (μ_2) and on hollow (μ_3) motives, and these observations led the path towards tentative interaction strength and charge effects.[4] According studies of isolated clusters revealed preferences of end on CO coordination.[5]

The electrostatic interaction of the adsorbed reactant molecules with a metal catalyst surface has been depicted by the Blyholder model, that proposes a σ-electron donor and π-acceptor synergism.[6] An analogous synergism was found in single transition metal atom ligand interactions by Dewar, Chatt and Duncanson[6], and current cluster research point towards similar effects.[7,8]

The surface morphologies of transition metal clusters governs binding, activation and conceivable cleavage of adsorbates.[9] Variations arise by the chemical composition and the prevailing charge state, and icosahedral, various cubic or hexagonal motifs dominate.[10] All of these properties scale with cluster size, and non-scalable exemptions prevail.[9,11] In particular, the cluster surface morphology determines the interaction of the adsorbate with transition metal cluster's surface and its local adsorption sites. This

[1] [1] Often, one is tempted to invoke empirical concepts such as physisorption and chemisorption. However, there is no clear and unambiguous definition of these terms, and various communities of researchers may associate different attributes. We refrain from utilizing these terms.

reflects in recordable features such as eigenmode shifts in IR photon dissociation (IR-PD) spectra.[8,12,13]

The charge state of the transition metal clusters has a large effect on the adsorbate-surface interaction. In accordance with the Blyholder model the electron density of the transition metal cluster determines σ-donor and π-acceptor interactions, together with the size and composition of the cluster. Electrophilic adsorbates, such as carbon monoxide, deplete some electron density at the cluster, as far as available. In this regard small anions serve best, and small cations worse. The larger the cluster become the less influence arises from a net surplus of single charges of any polarity; they dilute. This behavior has been summarized by the charge-dilution model.[14] and we subsequently referenced this model multiple times before. [8,13]

Spectroscopic experiments and quantum chemical modelling often meet to augment each other in a mutual favor. Here, we combine IR-PD spectroscopy with ab initio DFT calculations and thereby learn about electronic, geometric and vibrational structures of the investigated cluster adsorbate complexes.

In the current study we chose to expose anionic cobalt clusters $[Co_n]^-$ (n = 11 – 20) to dinitrogen, N_2 and we checked for its uptake under cryo conditions. The notation in the following paragraphs will follow the abbreviation $[Co_m(N_2)_n]^-$ = (m,n). We put the obtained results from the recorded IR-PD spectra into perspective with previous results on cationic cobalt clusters. Since previous studies in our group were conducted with the same experimental setup, we are able to compare the results with regard to the charge dilution model more precisely.

3.4 Experimental & computational methods

experimental

We conducted all experiments with a customized Fourier-Ion Cyclotron Resonance (FT-ICR)-mass spectrometer (Apex Ultra, Bruker Daltonics), including cluster production, isolation, N_2 condensation, InfraRed Photon Dissociation (IR-PD) and mass analysis. We generated the metal clusters using a home-built laser vaporization cluster ion source,

where cobalt atoms are evaporated from a rotating cobalt target (thickness 1 mm) by a second harmonic pulsed Nd:YAG ablation laser (20 Hz, 20 mJ/pulse). The resulting plasma expanded with a He gas pulse (40 µs, 15 bar) provided by a piezoelectric valve into the vacuum chamber. In the jet expansion atoms and ions were cooled and aggregated into clusters. The charged cluster were turned 90° onto the prime experimental axis by a quadrupole bender. A quadrupole mass filter isolated the desired cluster size and guided the clusters into a hexapole ion trap which is connected to a closed circle He cryostat. The ion trap was cooled to 26 K and filled with both He as a buffer gas and the reaction gas, in this case N_2. After a variable storage time (0-1 s) the adsorbate complexes were accelerated to the FT-ICR infinity cell. The cell was cooled by a closed circuit He cryostat to 10 K to prevent heating of the cluster by black body radiation. The generated ions were trapped in the ICR cell and irradiated with IR photons. The ICR cell was also used to detect the ions and determine the mass to charge (m/z) ratio.

As a light source a ND:Yag pump laser (Continuum DLS 8000, 10 Hz, 0,55 J/pulse) was coupled with an OPO/OPA tunable IR laser (LaserVision, KTP/KTA). The resulting Idler 2 and signal 2 radiation generated a difference frequency radiation using an $AgGaSe_2$ crystal. This results in IR-radiation in a range of 1000-2400 cm^{-1}. The IR spectra are obtained with the action spectroscopy method. The IR-PD signal was evaluated as $\Sigma_i F_i/(\Sigma_i F_i + \Sigma_i P_i)$, where F_i indicates fragment ion signal and P_i the parent ion signal. By plotting the fragmentation efficiency as a function of the laser frequency we received an IR-PD spectrum. In this work we recorded IR-PD spectra in the $1870 - 2210$ cm^{-1} of the $[Co_n(N_2)_m]^-$ (n = 11 – 20, m = 1, 2) species.

computational methods

DFT calculations were performed using the hybrid functional PBE014, the cc-pVTZ basis set15(N) and the effective core potential ecp28mdf16 provided by the Stuttgart/Cologne group[15] and the Gaussian 16 program package17[16]. All calculations were checked for imaginary frequencies and calculated using the standard convergence criterion (10-8). cc-pVDZ & ecp10mdf.

3.5 Results and discussion

The recorded IR-PD of the cryogenically cooled $[Co_n(N_2)_m]^-$ cluster adsorbate complexes reveal mostly well resolved bands in the range of 2000 – 2100 cm^{-1} (cf. Fig. 1), and all of the recorded bands are red shifted with respect to the IR inactive stretching mode of free N_2 (2330 cm^{-1}). There are some sharp bands ($\Delta\tilde{\nu}$ ~ 25 cm^{-1}), and some other bands are somewhat broader ($\Delta\tilde{\nu}$ ~ 100 cm^{-1}). Some broadening may be expected from coexisting N_2 binding site isomers. Cobalt anion clusters thus come with a largely smooth surface morphology of almost equivalent binding sites.

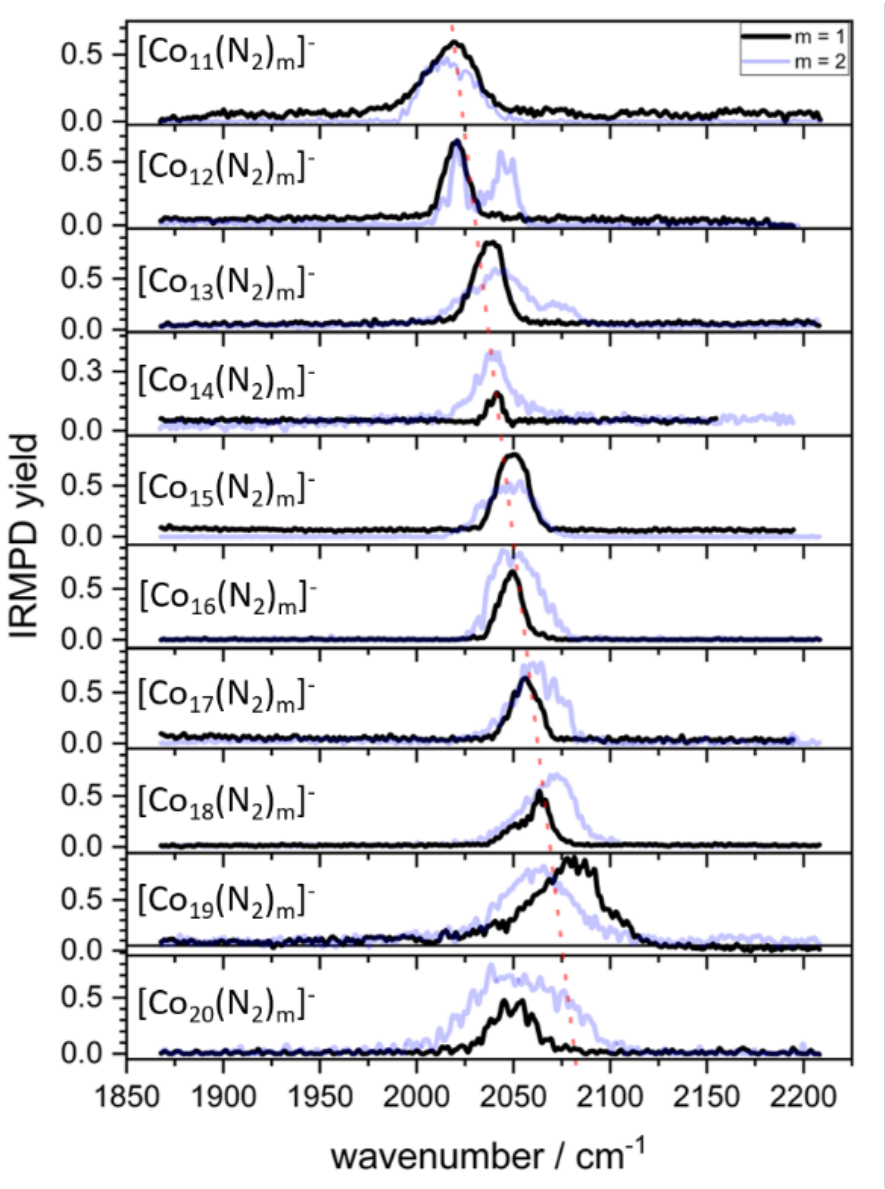


Figure 3.1: IR-PD spectra of $[Co_n(N_2)_m]^-$ for n = 11 – 20 and m = 1, 2. The dotted red line serves to guide the eye. The prevailing linear trend in the decreasing red shift of the N_2

stretching vibration frequency with increasing size of the cluster aligns with the decreasing charge per atom of the cobalt clusters. The spectrum of the first N_2 adsorbate of each cluster size shows only one peak, which indicates only one predominant isomer. (20,1) shows a stronger red shift compared to (17-19,1) which might hint to a reorganization of the cluster core.

The remarkable double peak feature in the IR-PD spectrum of (12,2) most likely reflects a symmetric-asymmetric stretching mode coupling amongst two adjacent N_2 adsorbates. We find no evidence for spontaneous N_2 activation or even cleavage, and the vast majority of N_2 adsorbates – if not all of them – reveal spectral fingerprints of likely end on coordination to single Co centers. The alternative side-on coordination, as evidenced in other cases of our investigations, does not show here. Fingerprints of nitride formation fall outside our range of investigations and would need future investigations by application of other non-table-top photon light sources such as e.g. an IR-FEL.

As evidenced by the red dotted line, depicted to guide the eye, the recorded band positions reveal a diminishing red shift upon an increase of cluster sizes. This trend is in line with the aforementioned charge dilution mode: The increasing cluster size dilutes the net negative charge per cluster atom, and it thereby hampers pi-backdonation from the TM cluster to the N2 adsorbate ligand.

Our DFT modelling suggests an icosahedral structure of the (13,0) cluster which provides for a “smooth” cluster surface with all equivalent surface sites. In accord the recorded IR-PD spectrum reveals a single vibrational band. The predicted electronic structure is most remarkable. The naked icosahedron shall comprise an electronic state of multiplicity M = 23. That would indicate 11 unpaired electrons. Upon N_2 adsorption the DFT modelling predicts a significant rise in multiplicity up to M = 29, which would indicate 14 unpaired electrons[-]. Our current DFT methodology fails to recover such effects, and a superior broken symmetry DFT modelling is out of reach in the present context.

The ab initio calculations propose a rise in the spin multiplicity from M = 23 to M = 29 after the first N_2 adsorption. DFT results identify relative changes in spin multiplicity more accurately than absolute values, so this proposition seems to have some significance.

Since the structure is supposed to be an icosahedron there exist possible explanations for this behavior. For cationic species Lau et all. analyzed XMCD spectra in terms of an icosahedral $[Fe_{13}]^+$ cluster configuration where the central atom is coupled antiferromagnetic to the 12 atom containing surrounding shell.[17] A similar effect occurs in $[Co_{13}]^+$.[18] It is well conceivable that such detailed spin coupling arises from a subtle balance that may shift e.g. by single N_2 adsorption and thereby increases spin multiplicity.

The recorded N_2 stretching bands in the IR-PD spectra of (n,1) and (n,2), n = 11-19 show a reduction of the redshift with increasing size of the Co clusters, which is roughly in accordance with the charge-dilution model. However, we see a slightly increased red shift of the N2 stretching band in (20,m) which breaks with this trend.

The proposed structure of (20,0) indicates an isotropic polarizability of 684.12 Bor^3, compared to 661.88 Bor^3 of (19,0). As a consequence, the ability to form a π-donor bond towards the attached Nitrogen molecule is enhanced, thus resulting in a stronger redshift of the recorded N_2 stretching band in the IR-PD spectrum of (20,1).

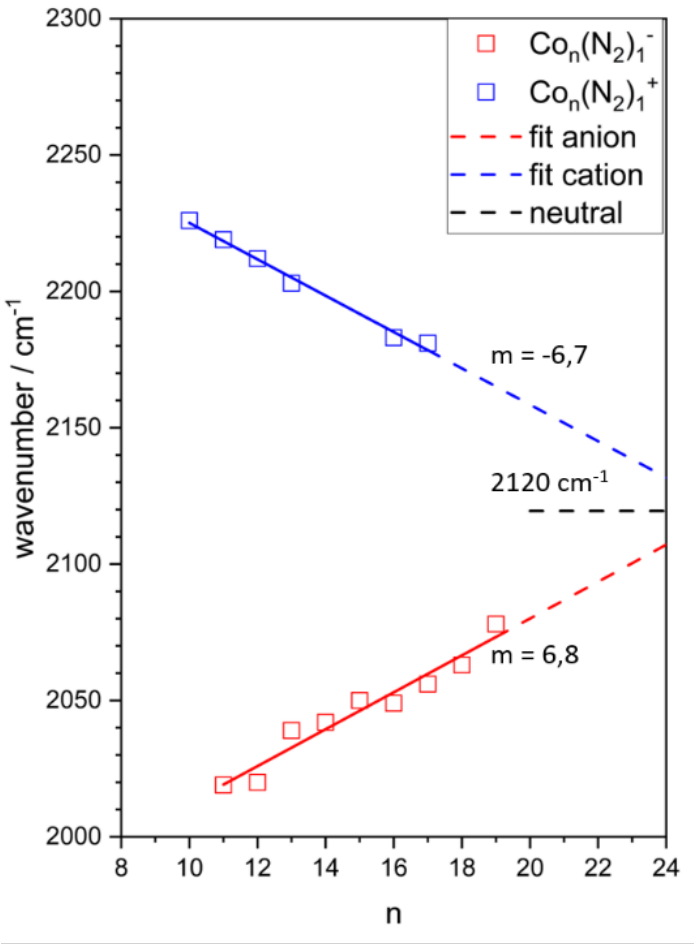


Figure 3.2: Recorded IR frequencies of $[Co_n(N_2)_1]^{+/-}$ for n = 10 – 19, cations in blue[13], anions in red. The dashed lines represent a linear fit of the data. The black line represents a hypothetical frequency of N_2 adsorbed onto a neutral cobalt surface. In both charge states a linear change in frequency with increasing cluster size is observed. The absolute value of both gradients is approximate.

It is most instructive to inspect the N_2 stretching band positions of cationic Cobalt cluster adsorbate complexes as well.[13] They experience an increase of red shift with increasing size of clusters – as opposed to those of the anionic clusters, which reveal a reduction of red shift with increasing cluster size. Total red shifts of N_2 stretching bands in cationic cluster complexes are smaller than in cationic cluster complexes which are in accordance with the Blyholder model: It is the total electron density which enables N_2 triple bond weakening π-backdonation. Anions donate better than cations. When increasing the size of the clusters net charge effects "dilute" and start to diminish in the asymptote, but for higher order effects such as static polarizability. Such ideas where largely conceived before, and they were summarized in the so called "charge dilution

model". According trends in the current data are visualized by the red and blue solid fits and extrapolated somewhat in Figure 3.2. Note the gradients of - 6.8 and + 6.7 cm^{-1}/n which are surprisingly close. One may dare to speculate about a common asymptote around 2120 cm^{-1} which may indicate the stretching mode band position of an N_2 ligand that is end-on adsorbed on a neutral cobalt cluster surface. As of now, we are not aware of any report on such experimental values.

The electronic structure of Cobalt clusters in the size regime n = 11-20 has significant influence on the Dinitrogen bond characteristics after absorption to the cluster surface. The charge of the clusters has a major effect summarized in the comparison of cationic and anionic cluster adsorbate N_2 stretching bonds in the IR-PD spectra. The charge to size ratio has a significant influence on the redshift of the bands in accordance with both the Blyholder – and charge dilution models. Additionally, the isotropic polarizability seems to explain the minor deviations from the general trend. The changes in electronic structure resulting in enhanced or depleted polarizability are strongly dependent on the cluster composition, size and geometry. Analyzing these effects requires more comparative studies.

3.6 Conclusion

In this study we presented the IR-PD spectra of adsorbed dinitrogen on anionic Cobalt clusters with a size range from 11 to 20 atoms. The recorded spectra reveal a trend in accordance with both the Blyholder and charge-dilution model. We found an unexpected rise in spin multiplicity upon N_2 uptake suggested by DFT calculations which can be explained with previous XMCD studies concerning icosahedral 3d clusters in the gas phase. Further on a significant deviation from the trend concerning the redshift of the IR-PD signals was found for $[Co_{20}]^-$ which can be explained with the isotropic polarizability of the cluster. We compared the IR-PD spectra of both cationic and anionic cluster species displaying inverted behavior concerning the charge state. From the fitted results we predict the signal frequency of a N_2 absorbed to a neutral Cobalt cluster surface.

3.7 Literature

[1] G. Ertl, M. Huber, N. Thiele, *Zeitschrift für Naturforschung A* **106**, 30.

[2] a) E. L. Muetterties, *Science* **1977**, *196*, 839; b) E. L. Muetterties, T. N. Rhodin, E. Band, C. F. Brucker, W. R. Pretzer, *Chem. Rev.* **1979**, *79*, 91; c) G. Ertl, *Angewandte Chemie* **2008**, *120*, 3578; d) E. Shustorovich in *Quantum Chemistry: The Challenge of Transition Metals and Coordination Chemistry*, Springer, Dordrecht, **1986**, pp. 445–464.

[3] a) D. M. Cox, K. C. Reichmann, D. J. Trevor, A. Kaldor, *J. Chem. Phys.* **1988**, *88*, 111; b) G. Somorjai, *Surface Science* **1994**, *299-300*, 849; c) G. Ertl, M. Neumann, K. M. Streit, *Surface Science* **1977**, *64*, 393; d) A. Nilsson, L. G. Pettersson, J. Norskov, *Chemical Bonding at Surfaces and Interfaces*, Elsevier, **2011**.

[4] a) A. Crossley, D. A. King, *Surface Science* **1977**, *68*, 528; b) R. M. Hammaker, S. A. Francis, R. P. Eischens, *Spectrochimica Acta* **1965**, *21*, 1295; c) F. Hoffmann, *Surface Science Reports* **1983**, *3*, 107.

[5] a) P. Gruene, D. M. Rayner, B. Redlich, A. F. G. van der Meer, J. T. Lyon, G. Meijer, A. Fielicke, *Science* **2008**, *321*, 674; b) A. Fielicke, P. Gruene, G. Meijer, D. M. Rayner, *Surface Science* **2009**, *603*, 1427.

[6] G. J. Kubas, *Journal of Organometallic Chemistry* **2001**, *635*, 37.

[7] a) A. Straßner, C. Wiehn, M. P. Klein, D. V. Fries, S. Dillinger, J. Mohrbach, M. H. Prosenc, P. B. Armentrout, G. Niedner-Schatteburg, *J. Chem. Phys.* **2021**, *155*, 244305; b) D. V. Fries, M. P. Klein, A. Steiner, M. H. Prosenc, G. Niedner-Schatteburg, *Phys. Chem. Chem. Phys.* **2021**, *23*, 11345.

[8] M. P. Klein, A. A. Ehrhard, M. E. Huber, A. Straßner, D. V. Fries, S. Dillinger, J. Mohrbach, G. Niedner-Schatteburg, *J. Chem. Phys.* **2022**, *156*, 14302.

[9] J. Mohrbach, S. Dillinger, G. Niedner-Schatteburg, *J. Phys. Chem. C* **2017**, *121*, 10907.

[10] a) A. S. Chaves, M. J. Piotrowski, J. L. F. Da Silva, *Phys. Chem. Chem. Phys.* **2017**, *19*, 15484; b) E. Waldt, A.-S. Hehn, R. Ahlrichs, M. M. Kappes, D. Schooss, *J. Chem. Phys.* **2015**, *142*, 24319; c) D. Schooss, M. N. Blom, J. H. Parks, B. v Issendorff, H. Haberland, M. M. Kappes, *Nano letters* **2005**, *5*, 1972.

[11] S. Dillinger, J. Mohrbach, G. Niedner-Schatteburg, *J. Chem. Phys.* **2017**, *147*, 184305.

[12] a) M. P. Klein, A. A. Ehrhard, J. Mohrbach, S. Dillinger, G. Niedner-Schatteburg, *Top Catal* **2018**, *61*, 106; b) S. Dillinger, M. P. Klein, A. Steiner, D. C. McDonald, M. A. Duncan, M. M. Kappes, G. Niedner-Schatteburg, *The journal of physical chemistry letters* **2018**, *9*, 914.

[13] S. Dillinger, J. Mohrbach, J. Hewer, M. Gaffga, G. Niedner-Schatteburg, *Phys. Chem. Chem. Phys.* **2015**, *17*, 10358.

[14] A. Fielicke, G. von Helden, G. Meijer, D. B. Pedersen, B. Simard, D. M. Rayner, *J. Chem. Phys.* **2006**, *124*, 194305.

[15] *Energy-adjusted ab initio pseudopotentials for the first row transition elements*, **1987**.

[16] M. J. Frisch, G. W. Trucks, H. B. Schlegel, G. E. Scuseria, M. A. Robb, J. R. Cheeseman, G. Scalmani, V. Barone, G. A. Petersson, H. Nakatsuji et al., *Gaussian 16*, Gaussian Inc., Wallingford CT, **2016**.

[17] M. Niemeyer, K. Hirsch, V. Zamudio-Bayer, A. Langenberg, M. Vogel, M. Kossick, C. Ebrecht, K. Egashira, A. Terasaki, T. Möller et al., *Phys. Rev. Lett.* **2012**, *108*, 57201.

[18] a) A. Langenberg, K. Hirsch, A. Ławicki, V. Zamudio-Bayer, M. Niemeyer, P. Chmiela, B. Langbehn, A. Terasaki, B. V. Issendorff, J. T. Lau, *Phys. Rev. B* **2014**, *90*; b) J. Meyer, M. Tombers, C. van Wüllen, G. Niedner-Schatteburg, S. Peredkov, W. Eberhardt, M. Neeb, S. Palutke, M. Martins, W. Wurth, *J. Chem. Phys.* **2015**, *143*, 104302.

3.8 Supporting information

The following structures have been calculated according to the methods described in the paper's experimental section. Abbreviations: $[Co_n(N_2)_m]^-$ = (n, m), multiplicity = M

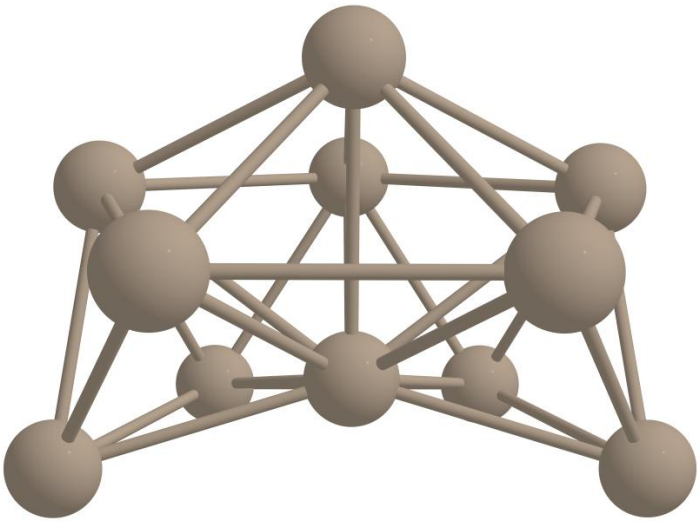


Figure SI.1: (11,0), M = 23

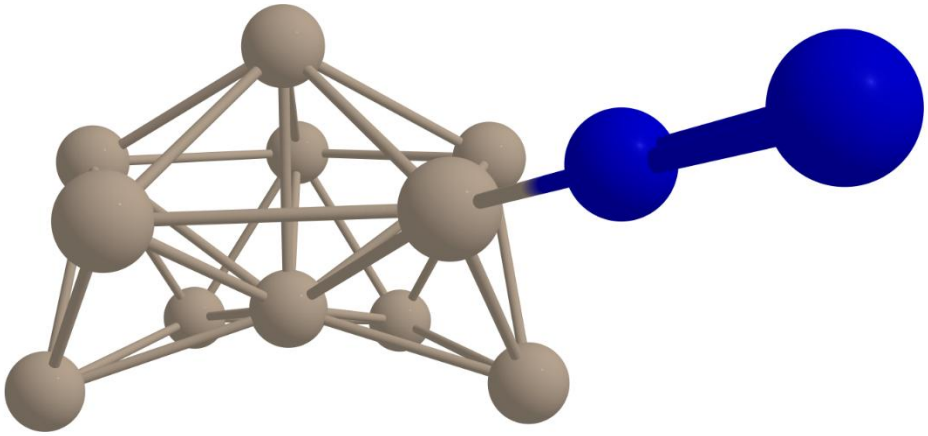


Figure SI.2: (11,1), M = 21

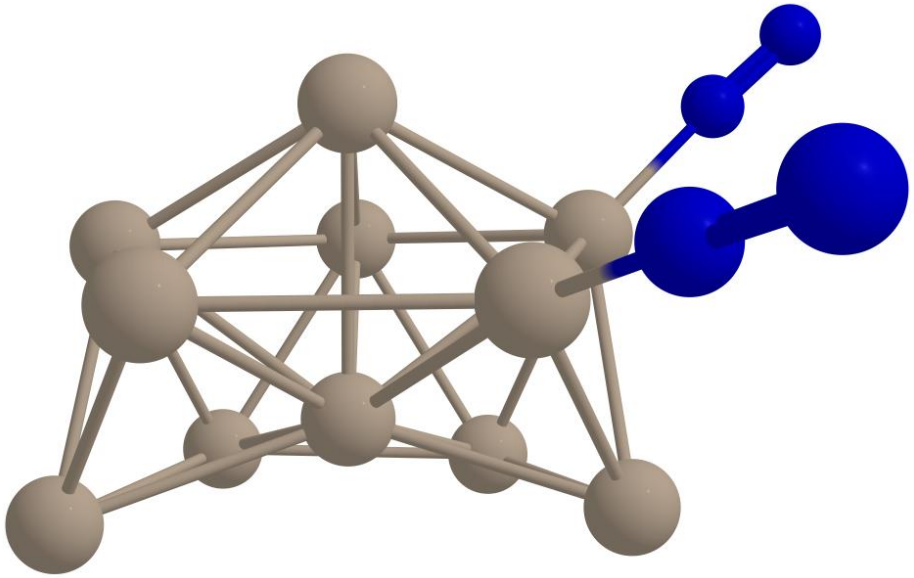


Figure SI.3: (11,2), M = 19

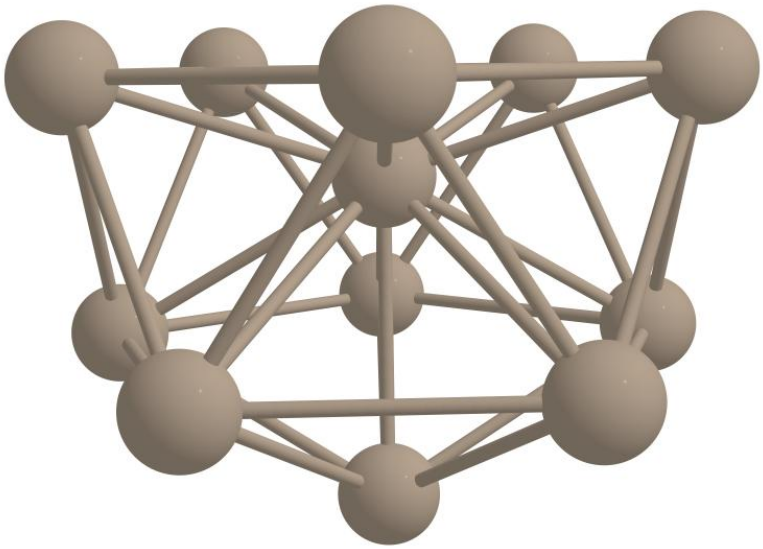


Figure SI.4: (12,0), M = 24

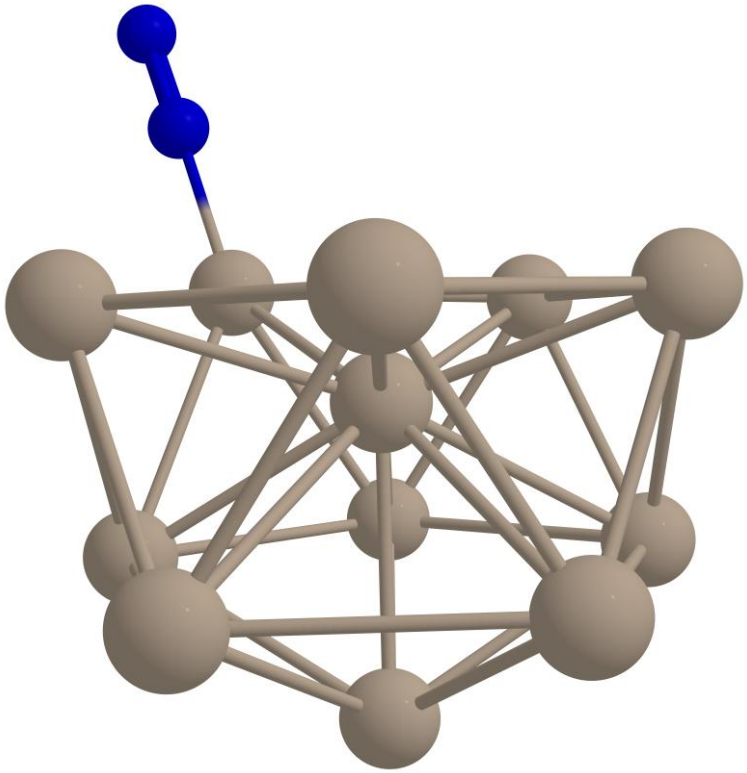


Figure SI.5: (12,1), M = 24

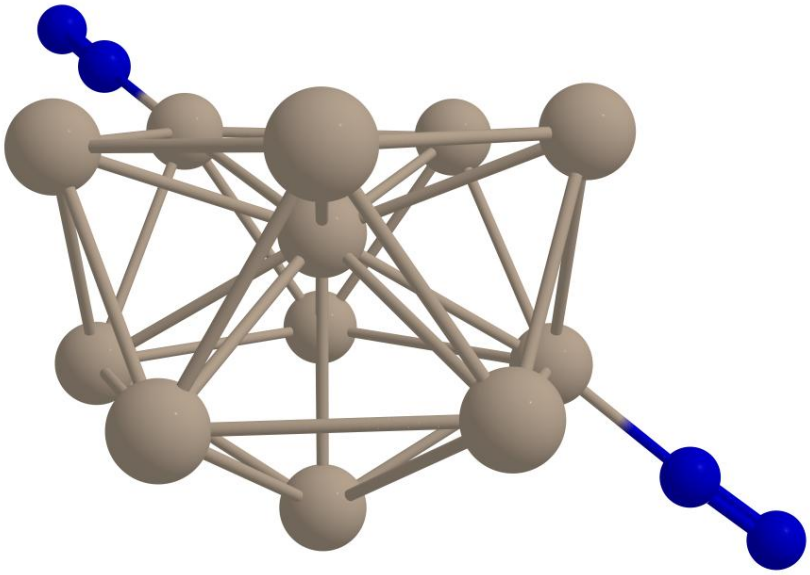


Figure SI.6: (12,2), M = 22

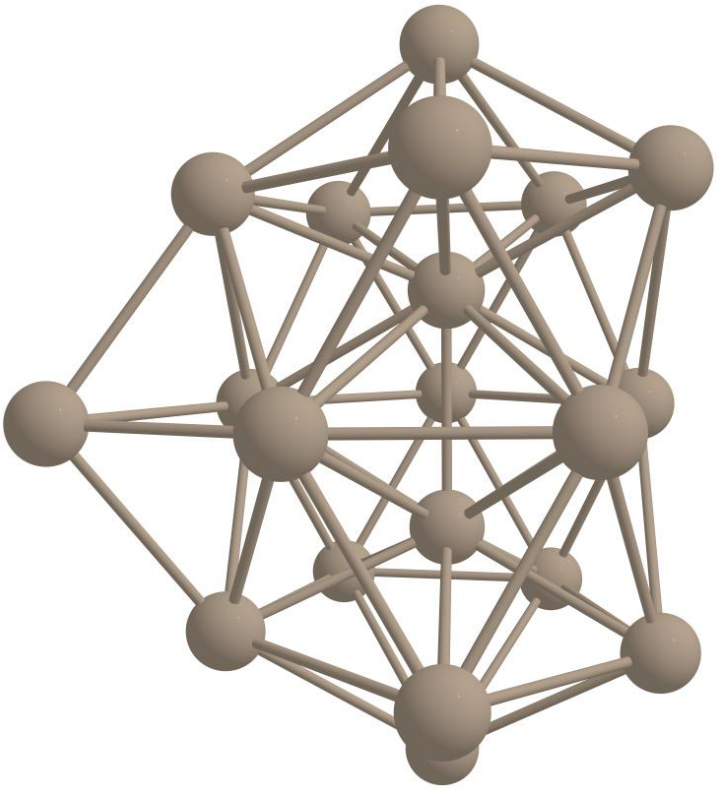
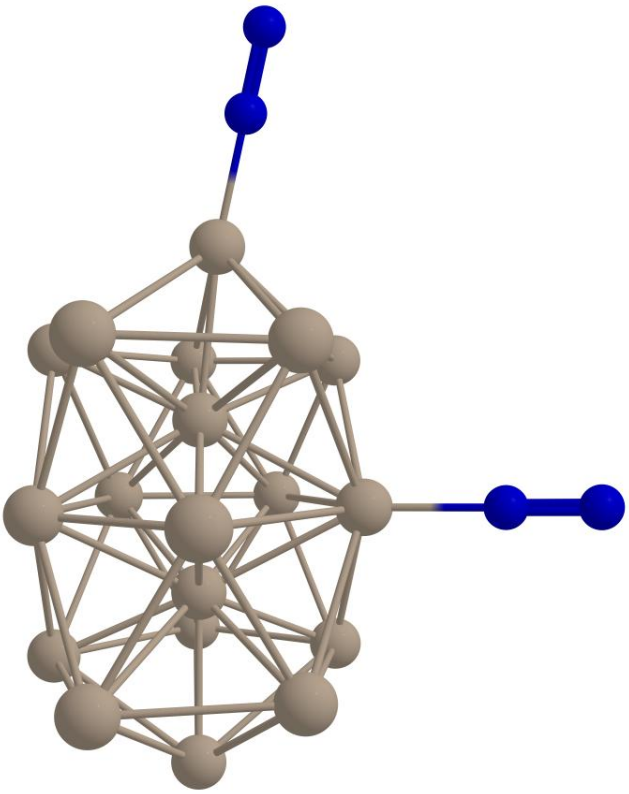


Figure SI.7: (13,0), M = 24



:

(12,2), M = 22

4 Nickel Cluster Anions in the gas phase at cryo conditions

Christopher Wiehn[a,b], Maximilian Luczak[a,c], Katharina Rediger[a] and Gereon Niedner-Schatteburg[a,d]

[a]Department of Chemistry, RPTU, 67663 Kaiserslautern, Germany

[b]present address: Defense Logistics Agency, Rhine Ordnance Barracks, 67663 Kaiserslautern, Germany

[c] present address: Math2Market GmbH, 67655 Kaiserslautern, Germany

[d]State Research Center OPTIMAS, RPTU, 67663 Kaiserslautern, Germany

4.1 Preamble

The experiments in this work have been conducted by Maximilian Luczak and Christopher Wiehn in equal parts at RPTU Kaiserslautern's FRITZ lab. The quantum chemical models have been performed by Christopher Wiehn, using Gaussian 16 software package run on the RPTU Kaiserslautern computing center. The results were discussed among Maximilian Luczak, Christopher Wiehn and Prof. Gereon Niedner-Schatteburg. The following paper was drafted by Maximilian Luczak and Gereon Niedner-Schatteburg.

4.2 Abstract

In this study we present IR-PD spectra of the anionic Ni11(N2)n- (n = 1-11) cluster-adsorbate complex at cryo-conditions. We recorded every nitrogen adsorption step and evaluated the results regarding the single fragmentation channels of the complex. The IR-PD spectra indicate a icosahedral structure of the nickel cluster, lacking two atoms on one side. This pocket-like structure offers an absorption side for a dinitrogen molecule in

a bridged configuration. The bridged configuration leads to a highly activated dinitrogen structure with its' stretching mode recorded at 1895 cm^{-1}.

4.3 Introduction

Important chemical processes such as the Sabatier reaction[1] or Raney nickel hydration reactions[2] rely on nickel for its' catalytic activity. Studies on the catalytic processes are often confined to either bulk materials or organometallic experiments using a single nickel metal center. Isolated nickel clusters can pick up reaction gases at cryo-temperatures and can present insights complementary to abovementioned studies.[3] In this study molecular dinitrogen is brought into reaction with a size selected anionic Ni_{11} cluster to investigate both the cluster's structure and the influence of the geometry on the absorbed dinitrogen molecules with IR-photodissociation action spectroscopy.

The adsorption process of gaseous dinitrogen to transition metal (TM) clusters at cryo conditions can be described by a σ-donor - π-acceptor synergism. This mechanism has been proposed by Blyholder[4] for the absorption of carbon monoxide to bulk surfaces. He postulated three binding motives: the on top (μ_1), on bridge (μ_2) and on hollow (μ_3) motives. In his work he was able to determine the different motives by their IR absorption bands. The interaction of the carbon monoxide with the metal surface according to the σ-donor - π-acceptor synergism results in the weakening of the central bond of the adsorbent and thus in a red shift of the observed IR bands. Since dinitrogen is isoelectronic to carbon monoxide, the same synergism and redshift of the IR active stretching mode at 2330 cm^{-1} can be expected and has been observed in the past. In organometallic chemistry the concept of Dewar, Chatt and Duncanson[5] is predominantly cited to explain a redshift in stretching modes of multi bonded atoms after the π*-antibonding orbital has been populated by electrons. Both models, Blyholder derived from surface physics and Dewar-Chatt-Duncanson from organometallic chemistry conclude in the same results and can be referred to in this study.

The interaction of nitrogen with TM clusters has been excessively studied by our group in the past. Tantal cationic[6], ruthenium[7], cobalt, rhodium both cationic and anionic. Nikel has been studied both cationic and anionic.[8] The experimental methods include both

kinetic studies of the uptake of dinitrogen under cryo temperatures as well as IR-PD action spectroscopy to probe isolated cluster-absorbate complexes. These studies highlighted the influence of geometry, charge state, cluster size and electronic structure of the TM cluster for both uptake and activation of nitrogen absorbents. The previous broader study of anionic nickel clusters (see chapter 4) in the range from Ni_{10}^- to Ni_{21}^- - dinitrogen complexes revealed a particularly big redshift in the Ni_{11}^- structure as well as a very complex IR-PD spectrum. In this study the focus will be on the sequential uptake of dinitrogen by the Ni_{11}^- cluster to identify both the structure of the structure of the cluster as well as the binding situation leading to this strongly activated dinitrogen adsorbate. A suggestion for the anionic Ni_{11}^- cluster has been provided by K. M. Ho et al.,[9] relying on computational methods to determine the geometric and electronic structure. They propose a fourfold capped pentagonal bipyramid structure with D_{3h} symmetry. However, this highly symmetrical geometry seems to be unlikely to explain the complex IR-PD spectrum of the fully saturated $Ni_{11}(N_2)_{11}^-$ cluster depicted in our previous study. In this work we will try to provide evidence for alternative geometries which allow for an explanation of the complex nature of beforementioned spectrum.

4.4 Experimental & computational methods

experimental We conducted all experiments with a customized Fourier-Ion Cyclotron Resonance (FT-ICR)-mass spectrometer (Apex Ultra, Bruker Daltonics), including cluster production, isolation, N_2 condensation, InfraRed Photon Dissociation (IR-PD) and mass analysis. We generated the metal clusters using a home-built laser vaporization cluster ion source, where cobalt atoms are evaporated from a rotating cobalt target (thickness 1 mm) by a second harmonic pulsed Nd:YAG ablation laser (20 Hz, 20 mJ/pulse). The resulting plasma expanded with a He gas pulse (40 µs, 15 bar) provided by a piezoelectric valve into the vacuum chamber. In the jet expansion atoms and ions were cooled and aggregated into clusters. The charged cluster were turned 90° onto the prime experimental axis by a quadrupole bender. A quadrupole mass filter isolated the desired cluster size and guided the clusters into a hexapole ion trap which is connected to a closed circle He cryostat. The ion trap was cooled to 26 K and filled with both He as a buffer gas and the reaction gas, in this case N_2. After a variable storage time (0-1 s) the

adsorbate complexes were accelerated to the FT-ICR infinity cell. The cell was cooled by a closed circuit He cryostat to 10 K to prevent heating of the cluster by black body radiation. The generated ions were trapped in the ICR cell and irradiated with IR photons. The ICR cell was also used to detect the ions and determine the mass to charge (m/z) ratio.

As a light source a ND:Yag pump laser (Continuum DLS 8000, 10 Hz, 0,55 J/pulse) was coupled with an OPO/OPA tunable IR laser (LaserVision, KTP/KTA). The resulting Idler 2 and signal 2 radiation generated a difference frequency radiation using an $AgGaSe_2$ crystal. This results in IR-radiation in a range of 1000-2400 cm^{-1}. The IR spectra are obtained with the action spectroscopy method. The IR-PD signal was evaluated as $\Sigma_i F_i/(\Sigma_i F_i + \Sigma_i P_i)$, where F_i indicates fragment ion signal and P_i the parent ion signal. By plotting the fragmentation efficiency as a function of the laser frequency we received an IR-PD spectrum. In this work we recorded IR-PD spectra in the 1870 – 2210 cm^{-1} of the $[Ni_n(N_2)_m]^-$ (n = 10 – 21, m = 1, 2) species.

computational methods DFT calculations were performed using the hybrid functional PBE0[14] and the effective core potential ecp10mdf[10] provided by the Stuttgart/Cologne group and the Gaussian 16 program package[11]. All calculations were checked for imaginary frequencies and calculated using the standard convergence criterion (10^{-8}).

4.5 Results & Discussion

The recorded IR-PD spectra of cryogenically cooled Ni11(N2)y- (y = 1-11) complexes in the range of v = 1870-2210 cm^{-1} are depicted in figure 1 in solid black lines. Alle recorded IR-modes are redshifted from the theoretical free stretching mode of dinitrogen at 2330 cm^{-1}, which is not IR active and could not be detected without a breach in symmetry occuring after the adsorption to the nickel cluster. We observe a broader main signal starting from 2025 to 2050 cm^{-1} for the Ni11(N2)1- complex, with the prak at 2040 cm^{-1}. This main signal is present in all successive complexes. The redshift observed of these main signals is less pronounced with every uptake of dinitrogen. The main signal of Ni11(N2)10 is recorded at 2075 cm^{-1} to 2125 cm^{-1} with the main peaks at 2095 cm^{-1} and 2110 cm^{-1}. The reduced

redshift is in accordance with the charge dilution model, which proposes a reduced ability to populate the pi* orbital of the dinitrogen tripple bond when the negative charge of the cluster is spread over a larger cluster-absorbates complex.

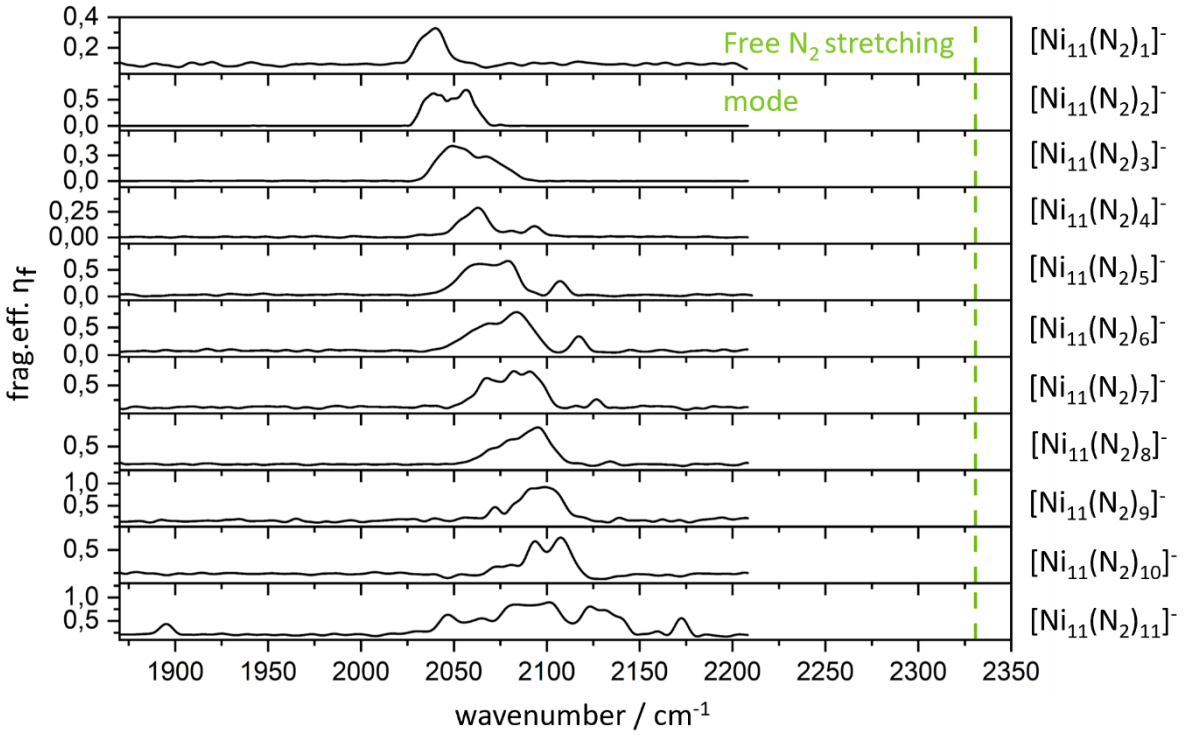


Figure 4.1: Thefigure displays the IR-PD spectra of Ni11(N2)n- (n=1-11) in the range of 1870 -2210 cm^{-1}. The total fragment yield is displayed in black solid lines. The location of the free dinitrogen streching mode at 2330 cm^{-1} is displayed in a dashed green line.

The IR-PD spectrum of Ni11(N2)2- shows two distinguishable IR signals at 2040 cm^{-1} and 2060 cm^{-1}. Several signals like this can be atrributed either to a split in symmetric and asymmetric stretching modes, or two geometrical different adsorption sites on the cluster and thus a slight difference in the electronical interaction between the cluster and the absorbed dinitrogen. To gain a better understanding of this phenomenon, we will look at the fragmentaion channels individually to see which part of the total fragment yield is contributed by each complex.

In Figure 2 the single fragmentaion channels of the IR-PD spectra of $Ni_{11}(N_2)_2^-$ and $Ni_{11}(N_2)_3^-$ are depicted in the colored lines. The total fragment yield is shown in a solid black line.

The figure on the left shows the two distinct features at 2040 cm^{-1} and 2060 cm^{-1}. The purple line shows the IR-PD spectra which corresponds to the loss of the first dinitrogen adsorbate, the blue line with the loss of both dinitrogen. The loss of the first dinitrogen is reponsible for the IR-PD signal at 2060 cm^{-1}. The blue line, representing the loss of the second dinitrogen and is more akin to the IR-PD spectrum of $Ni_{11}(N_2)_1^-$. This observation is suggesting that the absorption of the second dinitrogen is not equivalent to the absorption of the first dinitrogen. Therefore the two observed signals do not stem from a symmetrical and asymmetrical coupling of the two absorbed dinitrogen molecules, but from two nitrogen which have differences in their electronnical structure and therefore have a differnece in the IR-streching mode of each dinitrogen absorband.

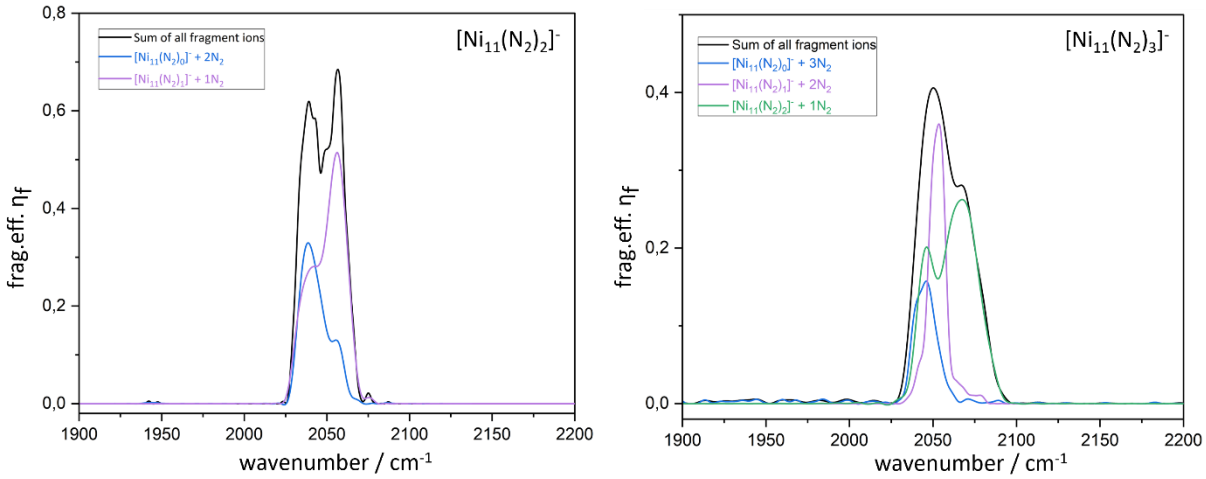


Figure 4.2: Figure 2 displays IR-PD spectra of Ni11(N2)n- (n = 2,3). The total fragmentation yield is depicted as a solid black line, additionally the single fragment channels are shown as colored solid lines.

A similar observation is made with the single fragment channels of the IR-PD spectrum of $Ni_{11}(N_2)_3^-$. The loss of the first dinitrogen, depicted in the solid green line is responsible for the shoulder observed at 2075 cm^{-1}. The loss of the second and third dinitrogen show a similar behavior as discussed in the spectrum of $Ni_{11}(N_2)_2^-$, both peaks being at the same positions at 2060 cm^{-1} for the loss of the second dinitrogen depicted in purple and 2040 cm^{-1} for the loss of the final dinitrogen depicted in blue.

The IR-PD spectra of $Ni_{11}(N_2)_y^-$ (y = 4-9) in figure 1 show a distinct signal to a higher vibrational energy from the main band. It does not have a high fragmentaion yield, but is

distinctive and comparatively narrow. The blueshift of the distinct feature to the first observed peak in the main band is increasing from 30 cm^{-1} to 40 cm^{-1}. To further the understanding of the origin of this feature we will again look at the multi fragment channel depictions. (See figure 3) We exemplarary study the multichannel fragment spectrum of $Ni_{11}(N_2)_5^-$.

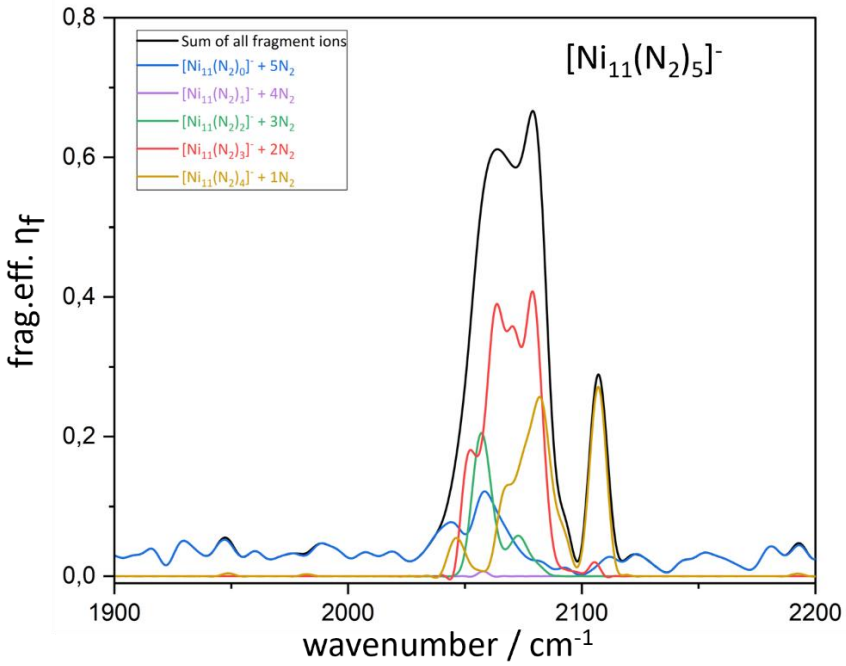


Figure 4.3: Figure 3 displays IR-PD spectra of $Ni_{11}(N_2)_5^-$. The total fragmentation yield is depicted as a solid black line, additionally the single fragment channels are shown as colored solid lines. The yellow solid line depicts the intensity of the $Ni_{11}(N_2)_4^-$ fragment channel, resulting from the loss of one absorbed dinitrogen molecules from the cluster-adsorbate complex. The red solid line shows the intensity of the $Ni_{11}(N_2)_3^-$ fragment channel, resulting from the loss of two absorbed dinitrogen molecules from the cluster-adsorbate complex.

The multichannel fragment spectrum of $Ni_{11}(N_2)_5^-$ shows the fragmentation yield of the first dinitrogen as a solid yellow line, the total fragment yield is depicted as a solid black line. The distinctive feature at 2110 cm^{-1} is shown to be entirely originating from the loss of the first dinitrogen molecule. The remaining dinitrogen adsorbates to not have a IR

active mode corresponding to this wavenumber. The structure of the main band can be entirely depicted by the fragmentation channels of the second dinitrogen loss. This observation is also present at the other multichannel spectra of $Ni_{11}(N_2)_y^-$ (y = 4-9).

We can interpred the blueshifted features with the σ-electron donor and π-acceptor synergism as proposed by Blyholder et al. Since the last adsorbed dinitrogen molecule shows an IR signal of a stronger dinitrogen stretching frequency, we can assume that there is less electron density transferred to the π* anti-binding orbital. The result therefore is a incomplete activation of the last absorbed dinitrogen. The adsorption of the next dinitrogen with the σ-electron donation increases the electron density in the cluster-adsorbate complex again. This increase in electron density allows the complex to complete the activation process of the previously absorbed dinitrogen, but results in the insufficient activation of the current absorption process. Since the cluster – adsorbate complex is increasing in size, the deficit becomes larger with every absorption step and the gap between the main signal and the feature of the last absorbed dinitrogen with every additional dinitrogen adsorption. The situation seems to change with the adsorption of the 10th dinitrogen. The IR-PD spectrum of $Ni_{11}(N_2)_2^-$ does not show a distinctive feature.

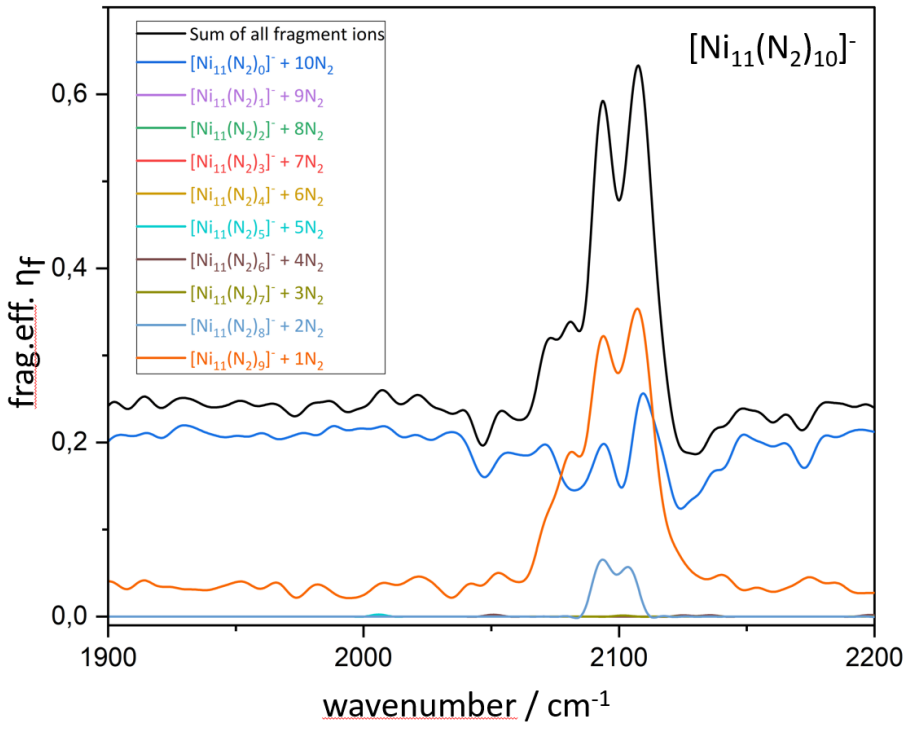


Figure 4.4: Figure 4 displays IR-PD spectra of $Ni_{11}(N_2)_{10}^-$. The total fragmentation yield is depicted as a solid black line, additionally the single fragment channels are shown as colored solid lines. The red solid line depicts the intensity of the $Ni_{11}(N_2)_9^-$ fragment channel, resulting from the loss of one absorbed dinitrogen molecules from the cluster-adsorbate complex.

The multifragment channel IR-PD spectrum of $Ni_{11}(N_2)_{10}^-$ shows two peaks in the main band at 2095 cm^{-1} and 2110 cm^{-1}. The loss of the first dinitrogen molecule is depicted as a solid red line. All the features present in the total fragment yield shown as a solid black line are present in the first fragment channel. The spectrum reveals three features, the two peaks in the main band and a shoulder at 2075 cm^{-1}. This indicates that $Ni_{11}(N_2)_{10}^-$ is a highly symmetrical structure, having three absorption sites at most. We keep this information in mind for the discussion of the cluster structure.

The $Ni_{11}(N_2)_{11}^-$ IR-PD spectrum shows a multitude of IR signals and features. Most notably two distinct features, one blueshifted to the main band at 2170 cm^{-1} and one far redshifted at 1895 cm^{-1}. Since the spectrum of $Ni_{11}(N_2)_{10}^-$ has shown very few signals and thus indicated a highly symmetrical structure, the symmetry is broken by the absorption of the 11th dinitrogen.

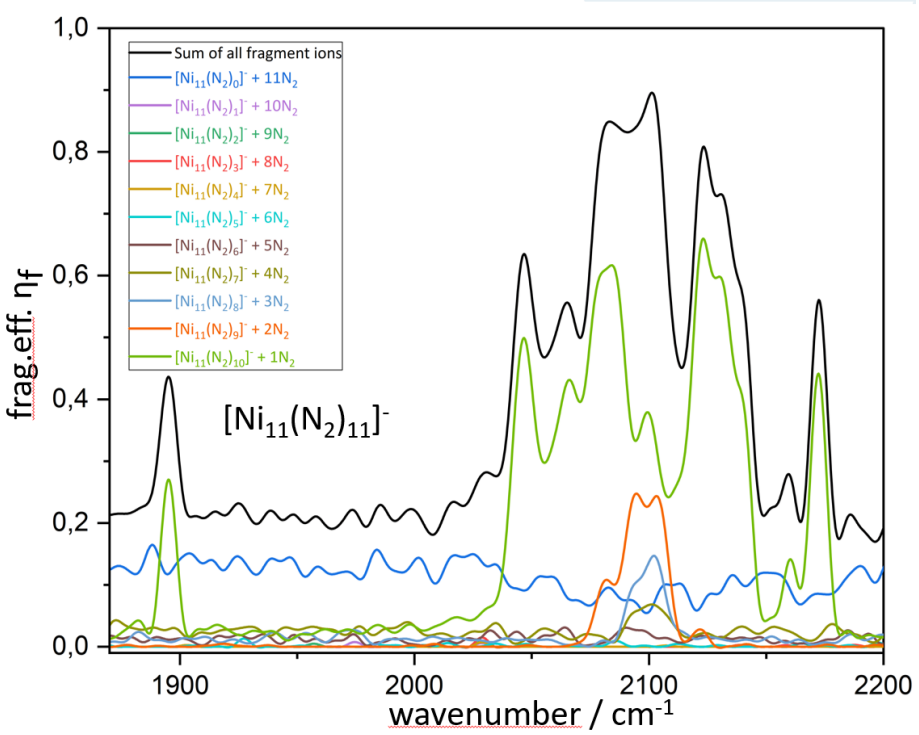


Figure. 4.5: Figure 5 displays IR-PD spectra of $Ni_{11}(N_2)_{11}^-$. The total fragmentation yield is depicted as a solid black line, additionally the single fragment channels are shown as colored solid lines. The green solid line depicts the intensity of the $Ni_{11}(N_2)_{10}^-$ fragment channel, resulting from the loss of one absorbed dinitrogen molecules from the cluster-adsorbate complex. The red solid line shows the intensity of the $Ni_{11}(N_2)_9^-$ fragment channel, resulting from the loss of two absorbed dinitrogen molecules from the cluster-adsorbate complex.

The multifragment channel IR-PD spectrum reveals that the the loss of the first, symmetry breaking dinitrogen, depicted in a solid green line is responsible for most of the IR signals of the total fragment yield IR-PD spectrum shown in a solid black line. The loss of the second dinitrogen absorbate, the remaining cluster – absorbate complex being $Ni_{11}(N_2)_{10}^-$ as discussed previously, is depicted as a solid red line and has the same features as the previous spectrum.

The observations make the cluster geometry proposed by K. M. Ho et al. unlikely. The proposed four-fold capped pentagonal bipyramid structure with D_{3h} symmetry has all eleven nickel atoms being on the cluster surface. Therefore, it is unlikely for the 11^{th} dinitrogen adsorbate to break the symmetry while the 10 dinitrogen previously adsorbed lead to a highly symmetrical structure. Furthermore, there is no geometric feature allowing to explain the significant activation of the final dinitrogen adsorbate.

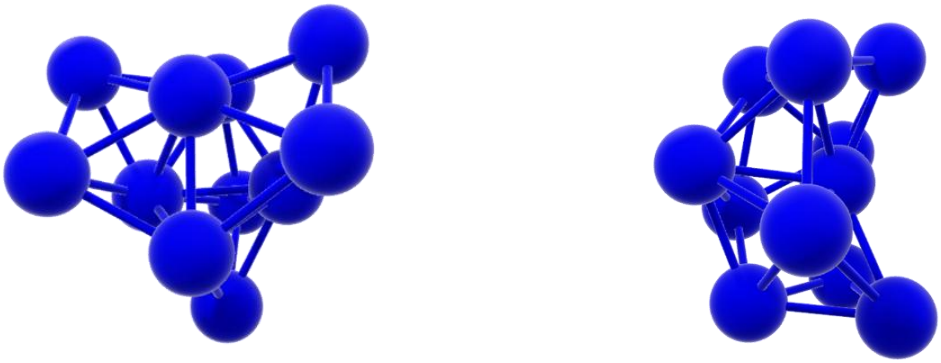


Figure 4.6: On the left handside the anionic Ni11- cluster is depicted as proposed by K.M. Ho et al.[9]. On the right handside our suggestion for a anionic Ni11- cluster is displayed.

We propose as a possible structure an Icosahedron lacking two atoms forming pocket-like structure. This structure has C_{2v} symmetry and has 10 nickel atoms on the surface and a 11th one in the pocket. It would allow for an μ_1 end-on adsorption of the first 10 dinitrogen molecules. This would result in a highly symmetrical structure with two distinguishable binding sites, four being on the icosahedral face of the cluster and six on the rim of the pocket. This structure explains the two peaks in the main band observed in the $Ni_{11}(N_2)_{10}^-$ spectrum. The 11th dinitrogen would locate in the pocket and probably end up in μ_2 bridge position. This disrupts the symmetry of the cluster – adsorbate complex and also explains the IR signal at 1895 cm^{-1}, yielding from a highly activated dinitrogen stretching mode.

Even though our observations are in favor of the “pocket”-structure, the difference to the published structure by K. M. Ho et al. does not disproof the quantum chemical models used in the study. It rather emphasizes the role of the ion source in given experiment which can lead to structures differing from setup to setup and being worth investigating.

4.6 Conclusion

The IR-PD spectra of $Ni_{11}(N_2)_y^-$ (y = 1-11) indicate a icosahedral structure, lacking two atoms forming a pocket like structure. The stepwise adsorption of dinitrogen molecules indicates a incomplete activation of the final adsorbed dinitrogen molecule. This effect is observed in the adsorption steps of $Ni_{11}(N_2)_y^-$ - (y = 4-9). The absorption of the 10th leads to a highly symmetrical structure of the cluster – adsorbate complex. This indicates a end-on adsorption of dinitrogen on the cluster surface. The final dinitrogen is adsorbed to the pocket structure, breaking the symmetry of the structure. The final dinitrogen forms a bridge adsorption structure in the pocket, leading to a highly activated dinitrogen.

4.7 Literature

[1] *Direct hydrogenation of oxides of carbon in presence of various finely divided metals*, **1902**.

[2] *Method of producing finely-divided nickel*, **1927**.

[3] a) F. Hoffmann, *Surface Science Reports* **1983**, *3*, 107; b) E. L. Muetterties, T. N. Rhodin, E. Band, C. F. Brucker, W. R. Pretzer, *Chem. Rev.* **1979**, *79*, 91.

[4] G. Blyholder, *J. Phys. Chem.* **1964**, *68*, 2772.

[5] J. Chatt, L. A. Duncanson, *J. Chem. Soc.* **1953**, 2939.

[6] D. V. Fries, M. P. Klein, A. Steiner, M. H. Prosenc, G. Niedner-Schatteburg, *Phys. Chem. Chem. Phys.* **2021**, *23*, 11345.

[7] S. Dillinger, M. P. Klein, A. Steiner, D. C. McDonald, M. A. Duncan, M. M. Kappes, G. Niedner-Schatteburg, *The journal of physical chemistry letters* **2018**, *9*, 914.

[8] a) J. Mohrbach, S. Dillinger, G. Niedner-Schatteburg, *J. Phys. Chem. C* **2017**, *121*, 10907; b) S. Dillinger, J. Mohrbach, G. Niedner-Schatteburg, *J. Chem. Phys.* **2017**, *147*, 184305.

[9] W. Song, W.-C. Lu, C. Z. Wang, K. M. Ho, *Computational and Theoretical Chemistry* **2011**, *978*, 41.

[10] *Energy-adjusted ab initio pseudopotentials for the first row transition elements*, **1987**.

[11] M. J. Frisch, G. W. Trucks, H. B. Schlegel, G. E. Scuseria, M. A. Robb, J. R. Cheeseman, G. Scalmani, V. Barone, G. A. Petersson, H. Nakatsuji et al., *Gaussian 16*, Gaussian Inc., Wallingford CT, **2016**.

5 Nickel cluster cations in the gas phase at cryo conditions

Christopher Wiehn[a,b], Maximilian Luczak[a,c] , Katharina Rediger[a] and Gereon Niedner-Schatteburg[a,d]

[a]Department of Chemistry, RPTU, 67663 Kaiserslautern, Germany

[b]present address: Defense Logistics Agency, Rhine Ordnance Barracks, 67663 Kaiserslautern, Germany

[c] present address: Math2Market GmbH, 67655 Kaiserslautern, Germany

[d]State Research Center OPTIMAS, RPTU, 67663 Kaiserslautern, Germany

5.1 Preamble

The experiments in this work have been conducted by Maximilian Luczak and Christopher Wiehn in equal parts at RPTU Kaiserslautern's FRITZ lab. The quantum chemical models have been performed by Christopher Wiehn, using Gaussian 16 software package run on the RPTU Kaiserslautern computing center. The results were discussed among Maximilian Luczak, Christopher Wiehn and Prof. Gereon Niedner-Schatteburg. The following paper was drafted by Maximilian Luczak and Gereon Niedner-Schatteburg.

5.2 Abstract

In this study we presented the IRPD spectra of adsorbed dinitrogen on anionic Nickel clusters with a size range from 10 to 21 atoms. The recorded spectra reveal a motive of asymptotic midigation towards a stable frequency of dinitrogen stretching mode for the cluster-adsobate complexes. We compared the IRPD spectra of both cationic and anionic cluster species displaying inverted behavior concerning the charge state. From the fitted results we predict the signal frequency of a N_2 absorbed to a neutral Nickel cluster surface.

5.3 Introduction

Nickel showcases catalytic activity in many chemical processes such as the Sabatier reaction [1], and Raney-Nickel hydration reactions.[2] Isolated nickel clusters at cryo temperatures are able to pick up dinitrogen and can be used as complementary studies to bulk surface and organometallic single atom metal center experiments.

Dinitrogen being isoelectronic to carbon monoxide shows similar properties regarding their coordination to transition metal atoms or bulk structures. The coordination can be described with a σ-donor - π-acceptor synergism postulated by Blyholder[3] and Dewar-Chatt Duncanson[4]. The level of coordination, the N-N triple bond strength and its possible activation have been studied using infrared photodissociation (IR-PD) action spectroscopy. A redshift from the nitrogen-nitrogen frequency at 2330 cm^{-1} indicates the activation of the nitrogen adsorbate on the cluster surface and reveals information on the binding motive of the adsorbate.

Geometry, charge state, cluster size and electronic structure of the transition metal cluster influence both the uptake and activation of nitrogen absorbents.[5] Previous studies exemplified the use of IR-PD spectra with the assistance of ab initio DFT-modeling to draw conclusions on the transition metal cluster-adsorbate complexes properties.[6,7–9] The properties of nickel cluster nitrogen complexes have been studied for cationic clusters of the size range n = 10-17.[9,10] In this paper we present IR-PD spectra of anionic nickel cluster nitrogen complexes in the n = 11-20 comparing the found properties to draw further conclusions on the effect of the charge state with regards to the size dependent changes in electronic structure.

5.4 Experimental & computational methods

We conducted all experiments with a customized Fourier-Ion Cyclotron Resonance (FT-ICR)-mass spectrometer (Apex Ultra, Bruker Daltonics), including cluster production, isolation, N_2 condensation, InfraRed Photon Dissociation (IR-PD) and mass analysis. We generated the metal clusters using a home-built laser vaporization cluster ion source, where cobalt atoms are evaporated from a rotating cobalt target (thickness 1 mm) by a second harmonic pulsed Nd:YAG ablation laser (20 Hz, 20 mJ/pulse). The resulting

plasma expanded with a He gas pulse (40 µs, 15 bar) provided by a piezoelectric valve into the vacuum chamber. In the jet expansion atoms and ions were cooled and aggregated into clusters. The charged cluster were turned 90° onto the prime experimental axis by a quadrupole bender. A quadrupole mass filter isolated the desired cluster size and guided the clusters into a hexapole ion trap which is connected to a closed circle He cryostat. The ion trap was cooled to 26 K and filled with both He as a buffer gas and the reaction gas, in this case N_2. After a variable storage time (0-1 s) the adsorbate complexes were accelerated to the FT-ICR infinity cell. The cell was cooled by a closed circuit He cryostat to 10 K to prevent heating of the cluster by black body radiation. The generated ions were trapped in the ICR cell and irradiated with IR photons. The ICR cell was also used to detect the ions and determine the mass to charge (m/z) ratio.

As a light source a ND:Yag pump laser (Continuum DLS 8000, 10 Hz, 0,55 J/pulse) was coupled with an OPO/OPA tunable IR laser (LaserVision, KTP/KTA). The resulting Idler 2 and signal 2 radiation generated a difference frequency radiation using an $AgGaSe_2$ crystal. This results in IR-radiation in a range of 1000-2400 cm^{-1}. The IR spectra are obtained with the action spectroscopy method. The IRPD signal was evaluated as $\Sigma_i F_i/(\Sigma_i F_i + \Sigma_i P_i)$, where F_i indicates fragment ion signal and P_i the parent ion signal. By plotting the fragmentation efficiency as a function of the laser frequency we received an IRPD spectrum. In this work we recorded IRPD spectra in the 1870 – 2210 cm^{-1} of the $[Co_n(N_2)_m]^-$ (n = 11 – 20, m = 1, 2) species.

computational methods DFT calculations were performed using the hybrid functional PBE014, the cc-pVTZ basis set15(N) and the effective core potential ecp28mdf16 provided by the Stuttgart/Cologne group[11] and the Gaussian 16 program package17[12]. All calculations were checked for imaginary frequencies and calculated using the standard convergence criterion (10-8). cc-pVDZ & ecp10mdf.

5.5 Results & Discussion

The recorded IR-PD spectra of cryogenically cooled $[Ni_n(N_2)_1]^-$ reveal mostly well resolved bands in the range of 2040 – 2095 cm^{-1} (cf. Fig. 1, black solid line). The absorption limit for the presented nickel clusters range from m = 9 - 18. The resulting IR-PD spectra range from

1890 – 2175 cm^{-1} (cf. Fig 1, blue solid line). All IR signals are red shifted with respect to the IR inactive stretching mode of free N_2 (2330 cm^{-1}).

The IR signals of the N_2 stretching mode of the first adsorbed Nitrogen molecule are red shifted to 2040 cm^{-1} for the n = 10, 11 size clusters. With increasing cluster size, the red shift decreases from 2040 cm^{-1} to 2095 cm^{-1}. The decreasing red shift with the increasing cluster size can be interpreted with the charge-dilution model[13], postulating a diminishing electron density surplus in larger systems resulting in weaker contribution to the anti-binding π-π* orbital. The recorded spectra do not show a linear trend however, which has been observed in previous experiments on Co, Ru and Rh clusters[7–10]. Previous experiments with nitrogen adsorbed on cationic nickel clusters have shown a similar, but mirrored trend of red shift and cluster size dependency (cf. Fig. 2).[9] Considering IR band signal positions of both cationic and anionic species, both trendlines are parallel at a sufficiently large cluster size. This observation is in accordance with the charge-dilution model.

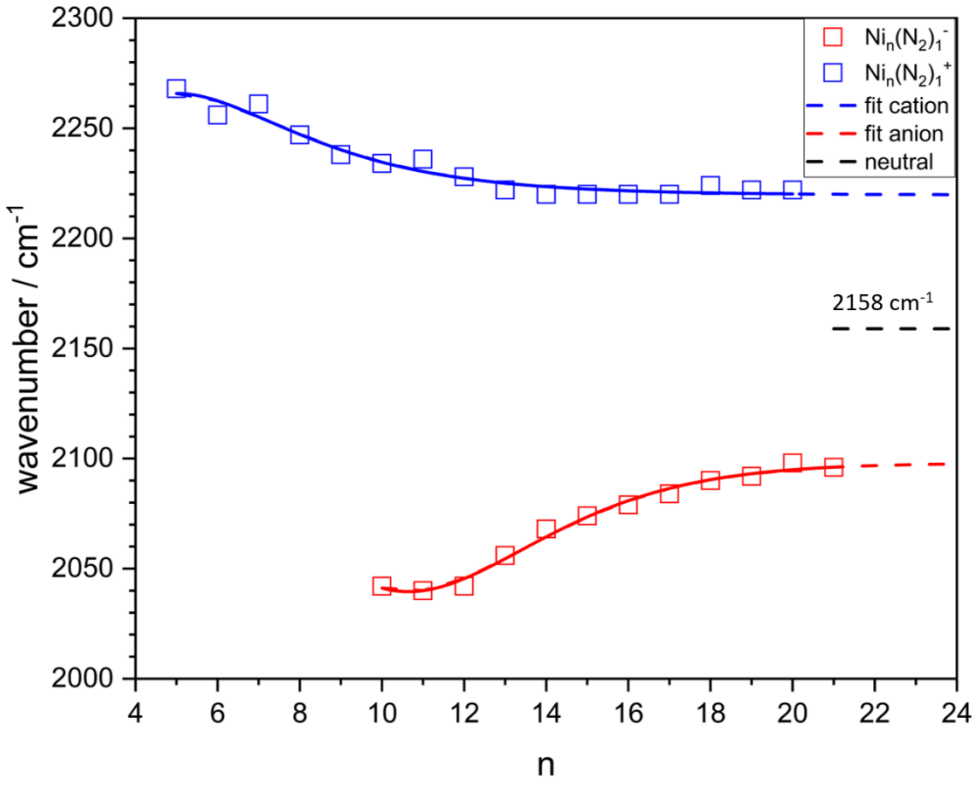


Figure 5.1: IR-PD frequencies of the N_2 stretching band of cationic cluster dinitrogen complexes $[Ni_n(N_2)_1]^+$ (n = 5-20) and anionic cluster dinitrogen complexes $[Ni_n(N_2)_1]^-$ (n = 10-21) are depicted in blue and red respectively. All frequencies are red shifted to the neutral N_2 stretching band at 2330 cm^{-1}, cationic species to 2270 cm^{-1} to 2225 cm^{-1},

anionic species to 2040 cm^{-1} to 2095 cm^{-1}. Both reveal a asymptotic solution toward 2158 cm^{-1} with increasing cluster size, where we propose the neutral cluster dinitrogen complex N_2 IR stretching band to be located.

The IR signals of the anionic nickel clusters with the maximum amount of dinitrogen attachable at cryo-conditions are displayed as solid blue lines in fig. 1. Here we can see a general trend of all IR signals being less redshifted than the signal for the single dinitrogen absorption complex. This is again in accordance with the charge-dilution model. Since the cluster – adsorbate complexes are larger with more adsorbed dinitrogen the negative charge becomes more diluted and is not available for the pi-backdonation into the anti-bonding π-π* orbitals of the dinitrogen triple bonds. The only exception to this trend can be observed for the $[Ni_{11}(N_2)_{11}]^-$ cluster – adsorbate complex. Here, a IR signal at 1895 cm-1 is detected. The nature of this feature is discussed in detail in its' own chapter.

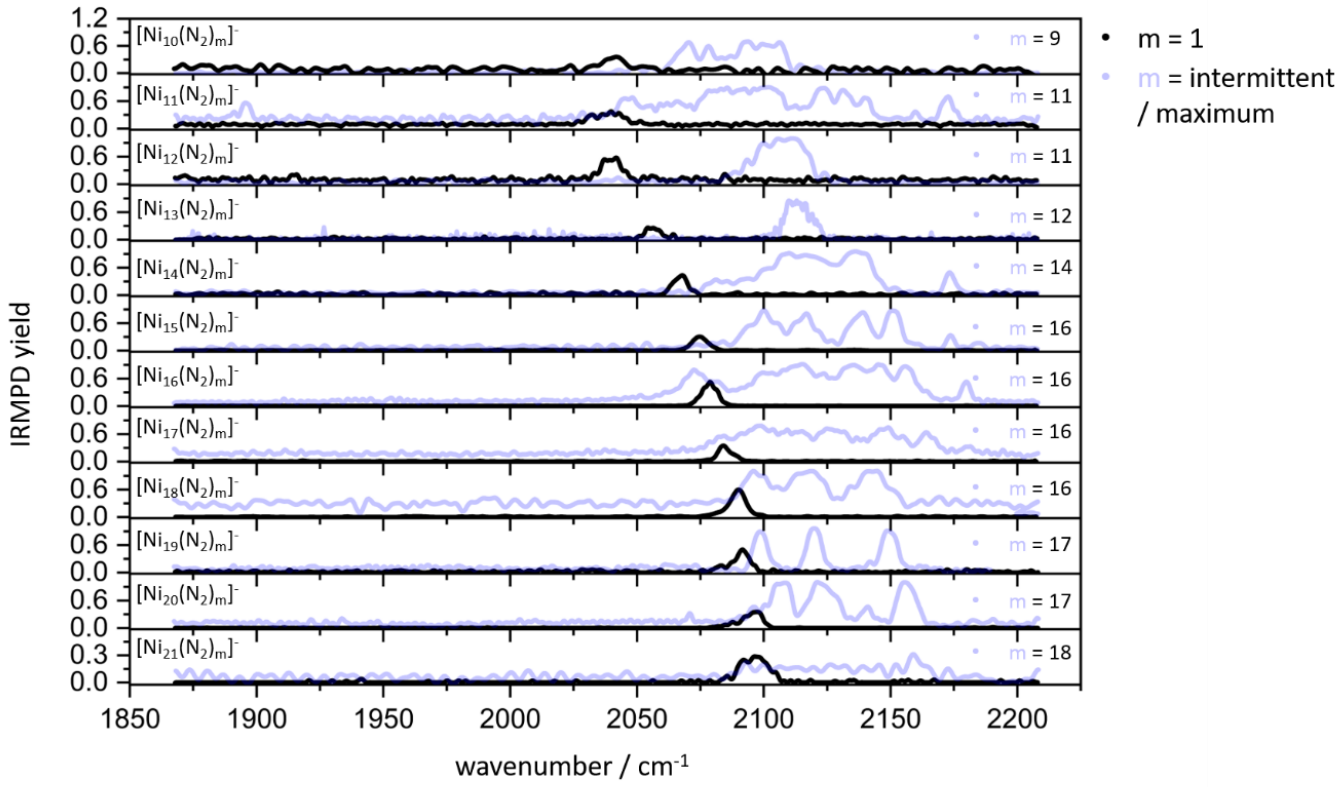


Figure 5.2: IR-PD spectra of $[Ni_n(N_2)_m]^-$ (n = 10-21; n = 1, intermittent/maximum N_2 uptake) from 1870 cm^{-1} to 2210 cm^{-1}. The recorded N_2 streching bands in the IR-PD spectra for the

$[Ni_n(N_2)_1]^-$ (n = 10-21) (black line) reveal a red shift from the free N_2 stretching band (2330 cm^{-1}) ranging from 2040 cm^{-1} to 2095 cm^{-1} decreasing with the size of the cluster. This gradual change does not follow a linear trend. The recorded N_2 streching bands in the IR-PD spectra for the $[Ni_n(N_2)_m]^-$ (n = 10-21, m = intermittent/maximum) (blue line) show significantly more features with the exeption of $[Ni_n(N_2)_m]^-$ (n = 12, 13) which show only one dominant feature.

The structure of the maximum absorption IR-PD spectra can give us some advice on the cluster geometry of anionic nickel clusters. The first observation is the single IR signal recorded for the $[Ni_{13}(N_2)_{12}]^-$ cluster – adsorbate complex at 2115 cm-1. This is indicating a highly symmetrical structure. 13 nickel atoms can form a icosahedron, presenting 12 equal nickel atoms on the surface and one atom in the center of the structure. Assuming the dinitrogen molecules are adsorbed in an end-on configuration, or μ_1 configuration as it is described by Blyholder et. al., twelve equivalent IR active chromophores are to be expected.

Following the cluster growth pattern, we can predict the formation of a double icosahedral structure for the anionic Ni_{19}- cluster. A double icosahedron has 17 atoms on the surface and two enveloped in the structure. A maximum pickup of 17 dinitrogen molecule supports this assumption. The IR-PD spectrum of $[Ni_{19}(N_2)_{17}]^-$ reveals three distinct IR signals at 2100 cm-1, 2120 cm-1 and 2150 cm-1. An icosahedral structure offers three different absorption sites. Two are located at the top and bottom ends of the structure, five are at the equator of the structure and ten are located between the equator and the ends of the structure. Therefore, the three distinct signals can be explained by the proposed geometric structure.

The in-depth examination of the $[Ni_{11}(N_2)_n]^-$ (n = 1-11)cluster – adsorbate complex indicated an icosahedral structure missing two atoms on one side, forming a pocket-like structure and thus a precursor to the icosahedral structure suggested for the $[Ni_{13}(N_2)_n]^-$ (n = 1-12) complex. Additionally, the appearance of the far redshifted IR signal was assigned to a bridged μ_2 adsorption to the pocket position.

5.6 Conclusion

In this work, we compare the IR-PD spectra of anionic nickel cluster-dinitrogen complexes with cationic species. The results can be interpreted with the Blyholder model as a primary effect and the charge dilution model as a secondary effect. The position of the IR signal for the neutral cluster-dinitrogen complex can be extrapolated from the data.

5.7 References

[1] a) *Direct hydrogenation of oxides of carbon in presence of various finely divided metals*, **1902**; b) *Ullmann's Encyclopedia of Industrial Chemistry*, Wiley-VCH Verlag GmbH & Co. KGaA, Weinheim, Germany, **2000**.

[2] a) *Preparation of solid catalysts*, Wiley-VCH, Weinheim, New York, **2010**; b) *Method of producing finely-divided nickel*, **1927**.

[3] G. Blyholder, *J. Phys. Chem.* **1964**, *68*, 2772.

[4] J. Chatt, L. A. Duncanson, *J. Chem. Soc.* **1953**, 2939.

[5] E. L. Muetterties, T. N. Rhodin, E. Band, C. F. Brucker, W. R. Pretzer, *Chem. Rev.* **1979**, *79*, 91.

[6] a) F. Hoffmann, *Surface Science Reports* **1983**, *3*, 107; b) D. M. Cox, K. C. Reichmann, D. J. Trevor, A. Kaldor, *J. Chem. Phys.* **1988**, *88*, 111.

[7] D. V. Fries, M. P. Klein, A. Steiner, M. H. Prosenc, G. Niedner-Schatteburg, *Phys. Chem. Chem. Phys.* **2021**, *23*, 11345.

[8] S. Dillinger, M. P. Klein, A. Steiner, D. C. McDonald, M. A. Duncan, M. M. Kappes, G. Niedner-Schatteburg, *The journal of physical chemistry letters* **2018**, *9*, 914.

[9] S. Dillinger, J. Mohrbach, G. Niedner-Schatteburg, *J. Chem. Phys.* **2017**, *147*, 184305.

[10] J. Mohrbach, S. Dillinger, G. Niedner-Schatteburg, *J. Phys. Chem. C* **2017**, *121*, 10907.

[11] *Energy-adjusted ab initio pseudopotentials for the first row transition elements*, **1987**.

[12] M. J. Frisch, G. W. Trucks, H. B. Schlegel, G. E. Scuseria, M. A. Robb, J. R. Cheeseman, G. Scalmani, V. Barone, G. A. Petersson, H. Nakatsuji et al., *Gaussian 16*, Gaussian Inc., Wallingford CT, **2016**.

[13] A. Fielicke, G. von Helden, G. Meijer, D. B. Pedersen, B. Simard, D. M. Rayner, *J. Chem. Phys.* **2006**, *124*, 194305.

6 Nitrogen adsorption and activation on size selected ruthenium cluster anions under cryo conditions in isolation

Christopher Wiehn[a,b], Maximilian Luczak[a,c] and Gereon Niedner-Schatteburg[a,d]

[a]Department of Chemistry, RPTU, 67663 Kaiserslautern, Germany

[b]present address: Defense Logistics Agency, Rhine Ordnance Barracks, 67663 Kaiserslautern, Germany

[c] present address: Math2Market GmbH, 67655 Kaiserslautern, Germany

[d]State Research Center OPTIMAS, RPTU, 67663 Kaiserslautern, Germany

6.1 Preamble

The experiments in this work have been conducted by Maximilian Luczak and Christopher Wiehn in equal parts at RPTU Kaiserslautern's FRITZ lab. The quantum chemical models have been performed by Christopher Wiehn, using Gaussian 16 software package run on the RPTU Kaiserslautern computing center. The results were discussed among Maximilian Luczak, Christopher Wiehn and Prof. Gereon Niedner-Schatteburg. The following paper was drafted by Maximilian Luczak and Gereon Niedner-Schatteburg.

6.2 Abstract

This study presents N_2 uptake kinetics at 26 K of anionic Ruthenium clusters $[Ru_n]^-$, n = 7-12 and IR Photon Dissociation (IR-PD) spectra of selected Ruthenium cluster – adsorbate complexes, $[Ru_n(N_2)_m]^-$, n = 7-12, m = 1-3, together with DFT modelling of selected cases. The uptake kinetics reveal large variations of the adsorption limit m_{max} by cluster size n, and some evidence for N_2 desorption. The recorded IR-PD bands correspond to red shifted stretching modes of end on coordinated N_2 adsorbates, and the band positions correlate with the calculated polarizability of the host clusters, varying by cluster size and structure, interpreted as σ acceptor – π donor action amongst clusters and adsorbates. IR-PD spectra of $[Ru_9(N_2)_2]^-$ require a DFT modelling in terms of an activated di-nitrido motif, which gives rise to further work in progress. N_2 stretching band positions in cationic

and anionic Ruthenium cluster – single N2 adsorbate complexes extrapolate well to published values of large neutral Ruthenium clusters.

6.3 Introduction

Industrial catalysis. The enduring quest for most effective reduction catalysis has found Ruthenium-based catalysts which operate with remarkable activity.[1-3] It is possible to operate them at mild conditions, as e.g. in the ammonia synthesis by the Kellogg Advanced Ammonia Process (KAAP), in contrast to iron-based catalysts as in use by the Haber-Bosch process.[4, 5] In KAAP, the rate determining step is the activation of dinitrogen [6, 7], which is mediated by highly coordinated sub surface atoms, so called B5 sites.[8] This finding hints to a structure sensitive cleavage of the N_2 bond. However, the reaction mechanism is not yet fully understood.

Ru surface science studies. Ruthenium compounds and their reactivity received repeated attention and characterization. Stern-Gerlach deflection studies reveal small magnetic moments of neutral ruthenium clusters.[9] IRMPD studies on Ruthenium-CO adsorbate complexes found size dependent adsorption motives, either end–on or bridged coordination.[10] Combined spectroscopic investigations of N_2/Ru(001) at low temperatures depict an end on coordination of the dinitrogen.[11, 12] Electron energy loss spectroscopy (EELS) and thermal desorption spectroscopy (TDS) studies showed preferentially dissociative adsorption of nitrogen onto a Ru(0001) surface at elevated temperatures.[13] Ru loaded Ca-Al-oxide electride materials showed capable to donate electrons and to receive hydrides whereby N_2 activation is enhanced and hydrogen poisoning suppressed.[14]

Gas phase ion chemistry and cryo ion trapping. The long time established research on gas phase ion spectroscopy and kinetics had largely focused in the past onto atmospheric chemistry and astrochemistry, and on related fundamental processes. Not so long ago, it received an eminent push forward by the advent of new ion generation schemes and – equally important – by the advance of ion trapping under well controlled cryo conditions which opened up new routes of research. There were established two

routes of cryo ion research by either cryo RF ion traps [15] [16-20] or by cryo penning traps [21-24], as reviewed recently [25]. It was the group of Peter Chen which achieved a high definition nominal 4 Kelvin isothermal trapping of isolated ions [24], and who managed to conduct trail blazing studies on isolated organic and metalorganic complexes [26, 27].

Elementary steps by cluster research. Considerable effort had been spent on the generation and characterization of isolated transition metal clusters, which proved well-suitable as model systems to investigate initial elementary steps of catalytic mechanisms, such as adsorption and adsorbate activation. [28] Our laboratory has contributed through cryo IR spectroscopy and cryo kinetic investigations of N_2 adsorption and activation by various 3d TM cluster cations [21, 29-34], and by case studies of selected 6d TM clusters [35-37].

Ruthenium clusters. Research on size selected Ruthenium clusters is sparse, however. Trapped ion electron diffraction (TIED) and Far-IR studies in conjunction with DFT modelling revealed cubic structure motives of some small anionic ruthenium clusters Ru_n^-, n = 8 - 13.[38, 39] Our previous case study on the coadsorption of H_2/N_2 onto an cationic ruthenium cluster revealed IR spectra that suggest a dissociative adsorption of the hydrogen as well as a migration of the hydride on the cluster surface that experiences some hindrance by N_2 adsorbates. [40]

The present study is first in a row of upcoming investigations on the characterization of like processes by *anionic* TM clusters. We chose to characterize anionic Ru clusters for their N_2 uptake and activation, by recording IR-PD spectra of size selected anionic Ruthenium cluster dinitrogen adsorbate complexes, n = 7 – 12, m ≤ 3, and by recording isothermal stepwise N_2 uptake kinetics under cryogenic conditions. Quantum chemical modelling at DFT level augments the experimental findings and allows for some structural conclusions.

6.4 Experimental and Computational Details

All experiments were conducted at a customized Fourier transform-ion cyclotron resonance (FT-ICR) mass spectrometer (Apex Ultra Bruker Daltonics), specifically: cluster

generation, isolation and selection, N_2 adsorption, infrared photodissociation (IR-PD) spectroscopy, and mass analysis. The metal cluster ions were generated from a monoisotopic ^{102}Ru target (99.38%, Oak Ridge National Laboratories) by a home-built laser vaporization source. We were able to generate clusters Ru_n^-, n = 4 – 12, with n = 5 missing. Following mass selection through an RF quadrupole, Ru clusters of sizes n = 7, 8, 9, 10, 11, or 12 were stored and thermalized in a cryogenic hexapole ion trap (at 26 K with Helium buffer gas at 4.0×10^{-6} mbar). The reaction gas (in this case N_2) was continuously introduced up to a pressure of 4.0 × 10−7 mbar, in order to yield sufficient amount of cluster adsorbate complexes. After a variable storage time (0–2.5 s), the ions were guided into the FT-ICR analysis cell, which was held at a temperature below 10 K. This cell was used for second MS selection, further storage, IR-PD spectroscopy and for ultimate ion detection.

When recording adsorption kinetics, the formed $[Ru_8(N_2)_m]^-$ cluster adsorbate complexes – originating from the prior RF hexapole cell - were detected in the downstream FT-ICR cell upon variation of their storage time in the RF hexapole cell. We fit the obtained kinetic data to a pseudo-first-order kinetic model, and thereby we determine pseudo-first-order rate constants for the individual adsorption steps. For a more detailed description of the kinetic data recording and analysis refer to Ref 22. We found cases were it showed necessary to invoke noticeable N_2 desorption in order to obtain a fit of the recorded data. For the sake of brevity, we utilize our previously introduced abbreviation $[Ru_n(N_2)_m]^-$ =: (n,m) wherever appropriate.

The recording of IR-PD spectra required application of a Nd: YAG laser (Continuum DLS 8000, 10 Hz, 0,55 J/pulse) pumped OPO/OPA setup (LaserVision, KTP/KTA) with a subsequent difference frequency mixing (DFM) stage to generate intense pulsed IR radiation in the range of 1000 – 2400 cm^{-1}. The IR-PD spectra were obtained by exposure of the selected cluster adsorbate complex to the IR radiation (2 – 4 laser shots at 10 Hz) and by recording the fragment ion intensities within the FT-IC trap while continuously scanning the IR frequency. The IRPD signal was evaluated as $\Sigma_i F_i / (\Sigma_i F_i + \Sigma_i P_i)$, where F_i indicates the fragment ion signal and P_i is the parent ion signal. By plotting the fragmentation efficiency as a function of the laser frequency, we obtain the IR-PD spectra.

In this work we recorded IR-PD spectra in the range of 1870 – 2210 cm^{-1} of the $[Ru_n(N_2)_m]^-$ (n = 7 – 12, m = 1 – 3 for n = 7 – 9 and m = 1 for n = 10 - 12) species. By utilizing the narrowband setup of our laser system (δv = 0.9 cm^{-1}) we obtain sharp bands.

We performed exploratory DFT calculations with the hybrid functional PBE0[41], the cc-pVTZ basis set (N) [42] and the effective core potential ecp28mdf (Ru)[43], as provided by the Stuttgart/Cologne group. We utilized the Gaussian 16 program package[44]. All calculations were obtained by application of standard convergence criterion (10^{-8}) and checked for absence of imaginary vibrational frequencies. Harmonic frequencies were scaled by a factor of 0.93 in order to match the experimental value of the N_2 stretching frequency in $[Ru_7(N_2)_1]^-$.

6.5 Results and Discussion

The recorded IR-PD spectra of $[Ru_n(N_2)_1]^-$ with n = 7 – 12 revealed well-resolved bands which locate in the region of 1990 – 2075 cm^{-1} (cf. Figure 1). All of the observed bands are significantly red-shifted with respect to the IR inactive stretching mode of free N_2 at 2330 cm^{-1}. In the cases of $[Ru_n(N_2)_m]^-$, m = 7 – 9, 12, we find single IR-PD bands. It is only the IR-PD spectra of $[Ru_{10}(N_2)_1]^-$ and $[Ru_{11}(N_2)_1]^-$, where we find two distinct bands. We attribute these either to two N_2 adsorption isomers, or to two Ru cluster-core isomers. In any case, the observed band positions indicate a most likely end-on μ_1 coordination of the adsorbed N_2 onto single atoms of the anionic Ru clusters, and this this assumption finds support by all of our DFT modelling, to be discussed in the following.

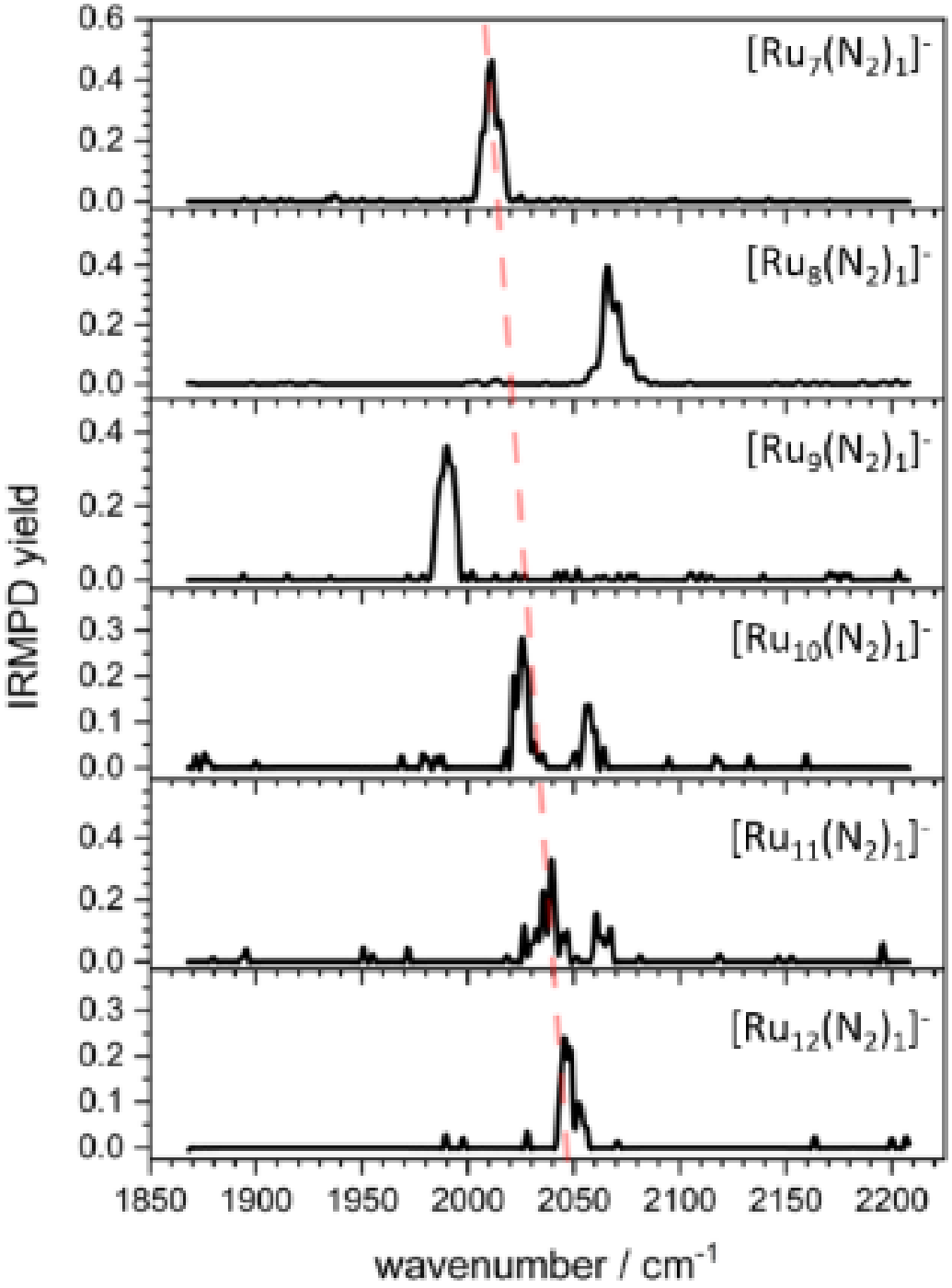


Fig. 6.1 Experimental IR-PD spectra of $[Ru_n(N_2)_1]^-$, n = 7 – 12. The dashed red line depicts a linear trend of slightly declining red shifts, with respect to the free N_2 vibration at 2330 cm^{-1} (not indicated). Obvious outliers are the single IR-PD bands of $[Ru_8(N_2)_1]^-$ and $[Ru_9(N_2)_1]^-$, and additional bands of $[Ru_{10}(N_2)_1]^-$ and $[Ru_{11}(N_2)_1]^-$. See text for further discussion.

The observed IR-PD band positions – besides the two cases of significant splittings – clearly indicate some overall trend: There is a systematic decrease of red shift with

increasing cluster size, as depicted by the dashed red line in Fig. 1, which we will discuss in more detail later on. Nevertheless, there are two outliers, $[Ru_8(N_2)_1]^-$ and $[Ru_9(N_2)_1]^-$, which reveal a smaller and higher red shift, respectively, than expected by a strictly linear trend.

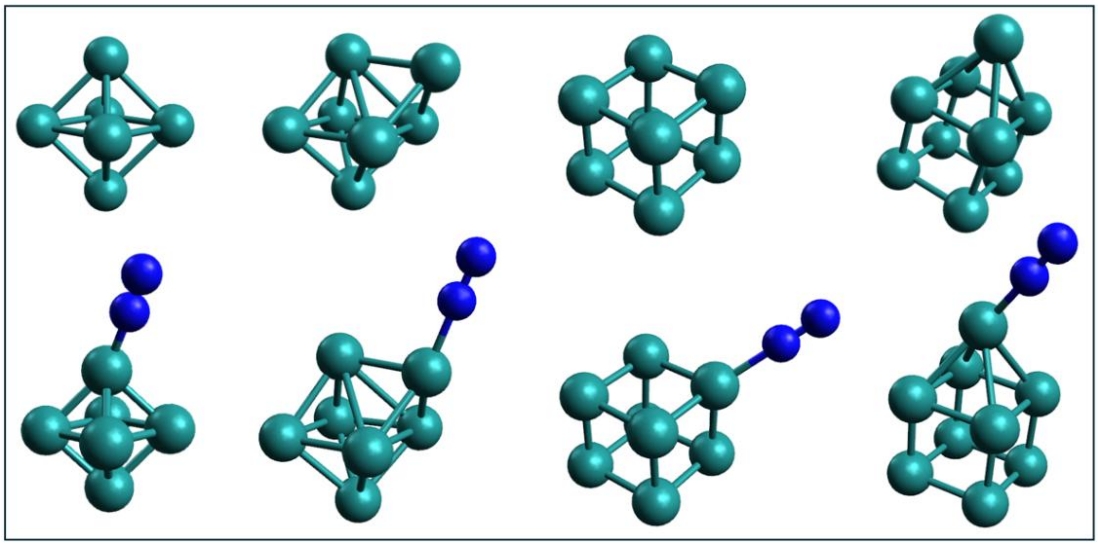


Fig. 6.2 Calculated most stable structures of $[Ru_n(N_2)_m]^-$, n=6-9, m = 0 (top row) and m=1 (bottom row), at the PBE0/cc-pVDZ(N)/ ecp28mdf(Ru) level of theory. Obviously, the N_2 coordination induces little structural relaxation of Ru cluster cores.

The n = 8 case could be due to a homogenous distribution of the net charge across a highly symmetric D_{4h} geometry of the Ru_8 cluster core (cf. Figure 4). The second outlier, $[Ru_9(N_2)_1]^-$, reveals an opposite deviation from the trend, an increased red shift, which amounts to -340 cm^{-1} with respect to uncoordinated, free N2, which is record holding amongst all likely end-on coordinated TM cluster – N_2 adsorbate complexes in a μ_1-κN1 coordination. It would take a μ_2-κN1:κN1,N2 tilted side on motif to yield even higher red shifts of N_2 bands, to as low as 1400 cm^{-1}as observed in the case of Ta_4^+ before [31].

Interestingly, our DFT modelling suggests a rough correlation of both IR-PD band positions – both with respect to the trend and to the two outliers - with the static isotropic polarizabilities of the reactant Ru cluster cations (cf. Tab. 1). When assuming an electron exchange interaction amongst Ru cluster and N_2 substrate, it comes to our mind a σ donor

π acceptor synergism as initially devised for metal olefin interactions [45]. Such Dewar-Chatt-Duncanson (DCD) stabilization would affect N_2 bond strength' largely through the π back donation into an antibinding N_2 π* orbital, while the σ donation from an N_2 terminal lone pair orbital into partially filled d orbitals of the Ru cluster has little effect on the N_2 bond strength'. Further discussion of charge and cluster size effects occur in the following (cf. Fig. 7 and text below).

There are to discuss the reduced and enhanced redshifts of the N_2 chromophore vibrations in $[Ru_8(N_2)_1]^-$, and $[Ru_9(N_2)_1]^-$, respectively. They correlate with the variations in the isotropic polarizabilities of the naked Ru clusters (Tab. 1). The larger the polarizabilities the larger the π back donation, and thereby the larger the N_2 redshift, and visa versa.

Table 6.1 By DFT calculated isotropic polarizabilities of $[Ru_n]^-$ and IR-PD band positions in $[Ru_n(N_2)_1]^-$

	Ru_n^-			$[Ru_n(N_2)_1]^-$	
n	Isotrop. Polarizability [Bohr^3]	Intensive polarizability per atom	Most stable multiplicity	IR-PD band position [cm^{-1}]	Most stable multiplicity
6	380	63.3	18	-	18
7	412	58.9	22	2010	22
8	365	45.6	6	2070	6
9	483	53.7	8	1990	8

Beyond single N_2 adsorption we checked for stepwise addition of up to three N_2 ligands, and the according IR-PD spectra show an increasing degree of complexity. The IR-PD spectrum of $[Ru_7(N_2)_2]^-$ reveals a sharp band at 2005 cm^{-1} (FWHM: 8 cm^{-1}) and an inhomogeneous broad band peaking at 2030 cm^{-1} (FWHM: 20 cm^{-1}). The magnitude of this splitting – about 25 cm^{-1} - resembles that of previous observations[29], which we interpreted as a likely symmetric / antisymmetric coupling of adjacent N_2 oscillators. Such interpretation might hold in the present case as well. The inhomogeneous broadening of the latter band at 2030 cm^{-1} points towards an additional adsorption site isomerism.

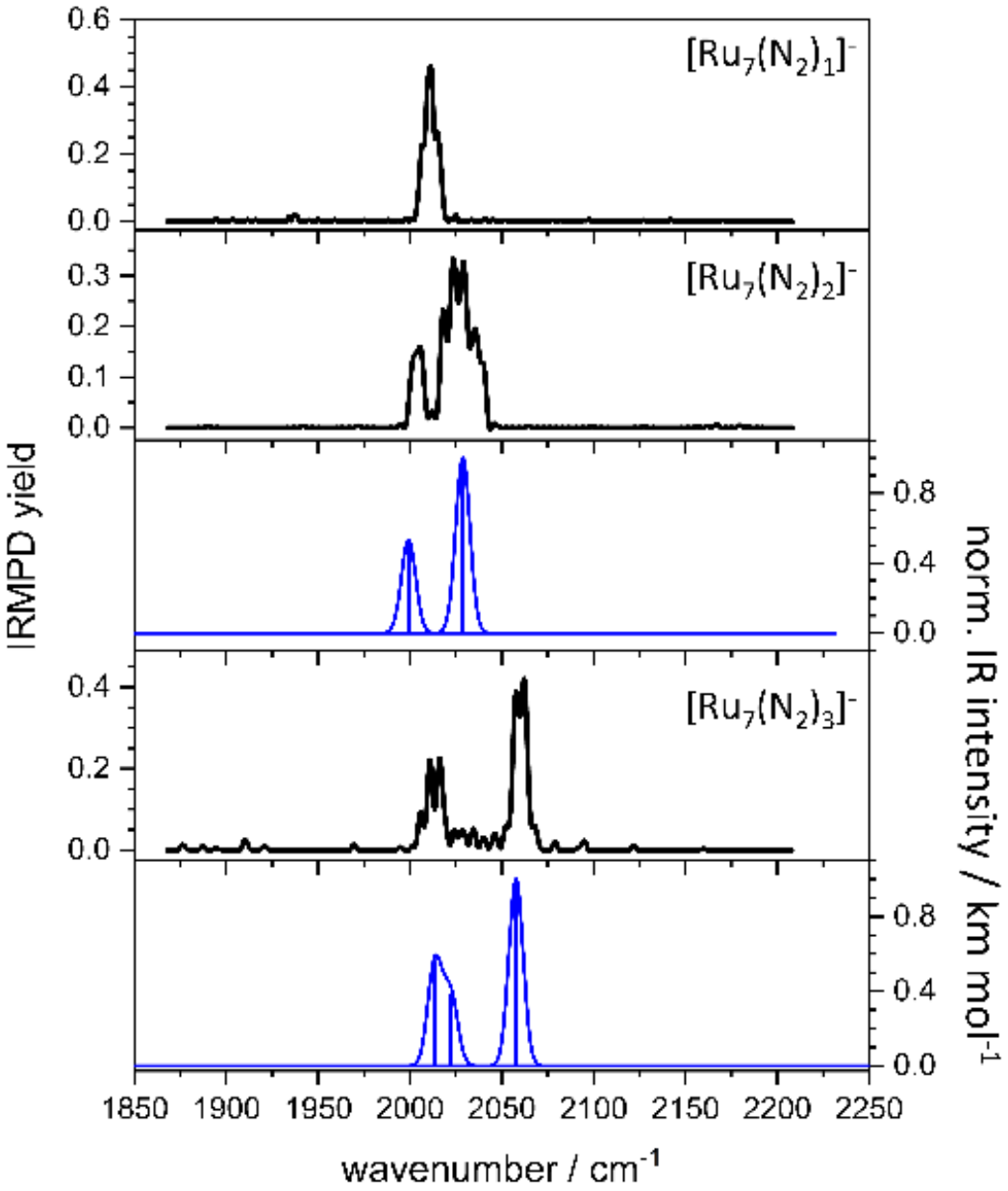


Fig. 6.3 Experimental IR-PD spectra of $[Ru_7(N_2)_m]^-$, m = 1 – 3 (in black) and calculated IR spectra of m = 2, 3 (in blue). The single observed IR-PD band of m = 1 at 2010 cm^{-1} seems to evolve into multiple bands in cases of m= 2 and 3 which finds an interpretation through DFT modelling. For further details refer to the text.

The IR-PD spectrum of $[Ru_7(N_2)_3]^-$ has two bands with an enhanced splitting of 50 cm^{-1} – twice as large as that of $[Ru_7(N_2)_2]^-$ - and neither of the two observed IR-PD bands are broadened. Both bands are quite sharp with a FWHM of merely 10 and 8 cm^{-1}, respectively. One may wonder about a structural and dynamic reasoning for such

complex behavior. It seems most likely that the first N_2 ligand occupies a site of highest polarizability. In the C_s structure of Fig. 3 there is the fivefold coordinated tip atom on top, which might serve for such reasoning. A high red shift of the N_2 stretching vibration results. The polarizability of the $[Ru_m(N_2)_n]^-$ =: (m,n) = (7,2) complex is reduced with respect to the naked (7,0) one, cf. Tab. 1. The second N_2 thus achieves less red shift upon coordination – no matter where it coordinates. The lowest coordinated Ru site comes to our mind, which is that tippy site which is the merely threefold coordinated adatom to the octahedral scaffold, the second tippy atom at the top of Fig. 3. By virtue of its low coordination it might allow for more flexibility and a softer tilting or wagging of its N_2 adsorbate, and the resulting IR-PD band assumes a higher width. A third N_2 ligand might favorably choose the same low coordinated site – at the expense of some reduced red shift, and of mutual stiffing in the wagging coordinates of itself and of the prior ligand. The according IR-PD band gets narrow.

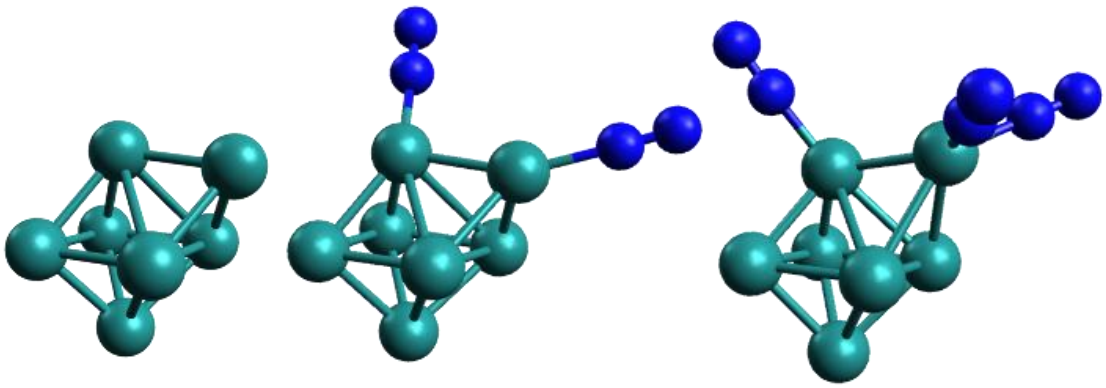


Fig.6.4 Stepwise N_2 adsorption in the case of $[Ru_7(N_2)_m]^-$ m = 0, 2, 3 as calculated at the PBE0/cc-pVDZ(N)/ecp28mdf(Ru) level of theory.

The recorded isothermal kinetics of the N_2 adsorption reveal a stepwise uptake (cf. Fig. S1 in the supplement) of up to six molecules. The kinetic fits (Fig. S2 in the supplement) indicate some modulation of the uptake rate, and an onset of competing N_2 desorption at m = 3, namely a significantly high desorption rate $k_{-(7,3)}$ of the third N_2 ligand, and of all subsequent ones. Such behavior is well in line with our interpretation of the recorded IR-PD spectrum of (7,3).

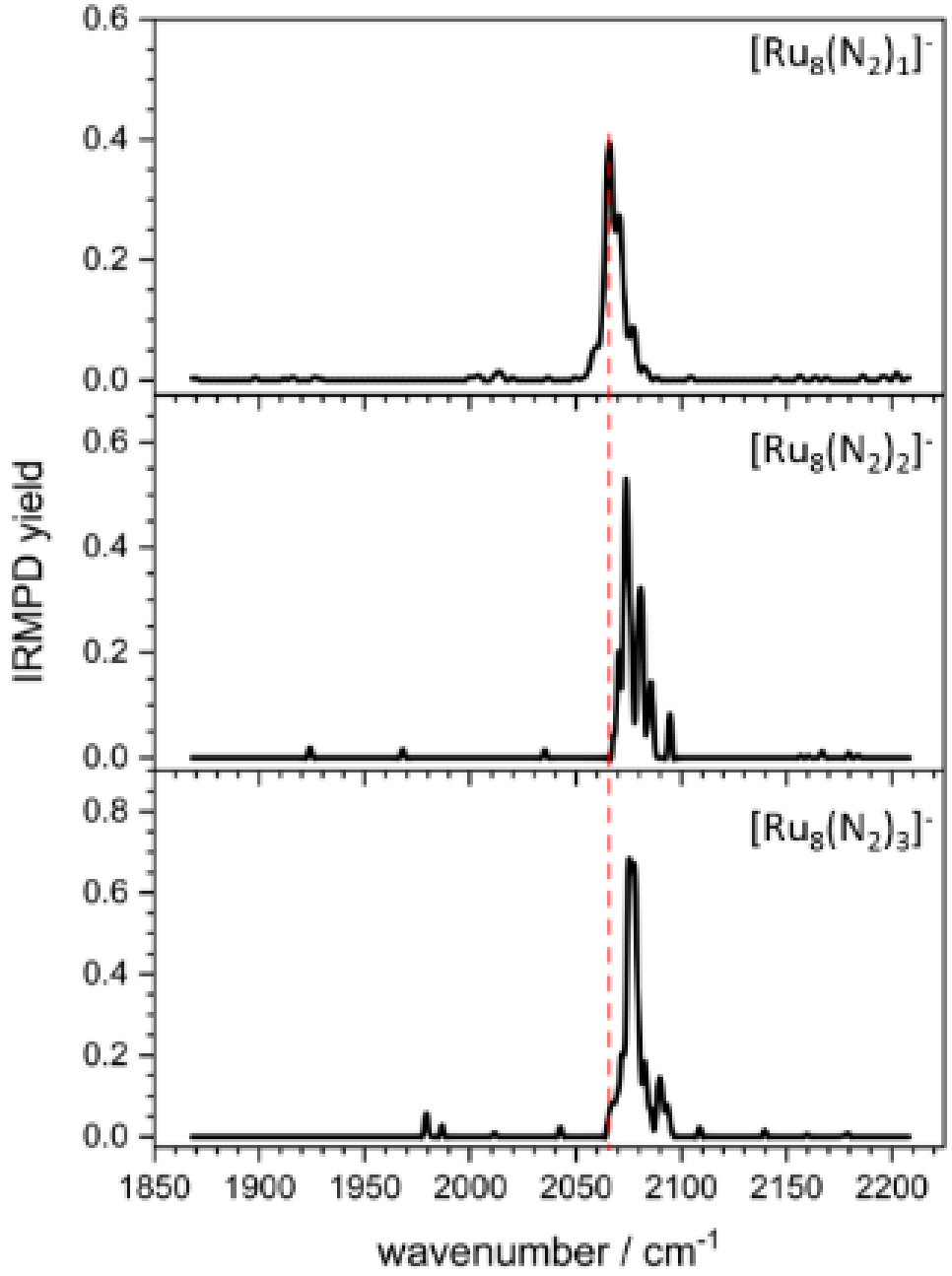


Fig. 6.5 IR-PD spectra of $[Ru_8(N_2)_m]^-$, m = 1 – 3. The dashed red line serves to recognize a small shift of the recorded IR bands with increasing m.

The structure of bare $[Ru_8]^-$ had been determined before by trapped ion electron diffraction experiments (TIED) [38], and it showed to be a highly symmetric D_{4h} cubic cluster with a slight Jahn-Teller distortion (Fig. 4). Note, that such a structure provides for all equivalent adsorption sites.

The recorded IR-PD spectra of $[Ru_8(N_2)_m]^-$ m = 1,..,3 reveal single, quite narrow, but inhomogeneous bands around 2070 cm^{-1} (Fig. 3). There is a minor blue shift of these bands with increasing m, about less than 10 cm^{-1}, per additional N_2. This finding is in

accordance with the predictions by a charge dilution model, which proposes a decrease in red shift with diminishing charge per cluster atom[10], as is the case with increasing number of adsorbates as well. However, the reduction in the red shift of the N_2 stretching frequency is less than expected, which we attribute to the high symmetry of the cluster core and its homogenous charge distribution.

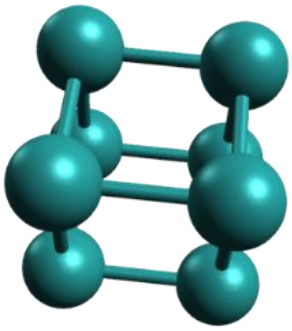


Fig. 6.6 Cubic structure of $[Ru_8]^-$ as calculated at the PBE0/ecp28mdf level of theory and confirmed by electron diffraction experiments [38]

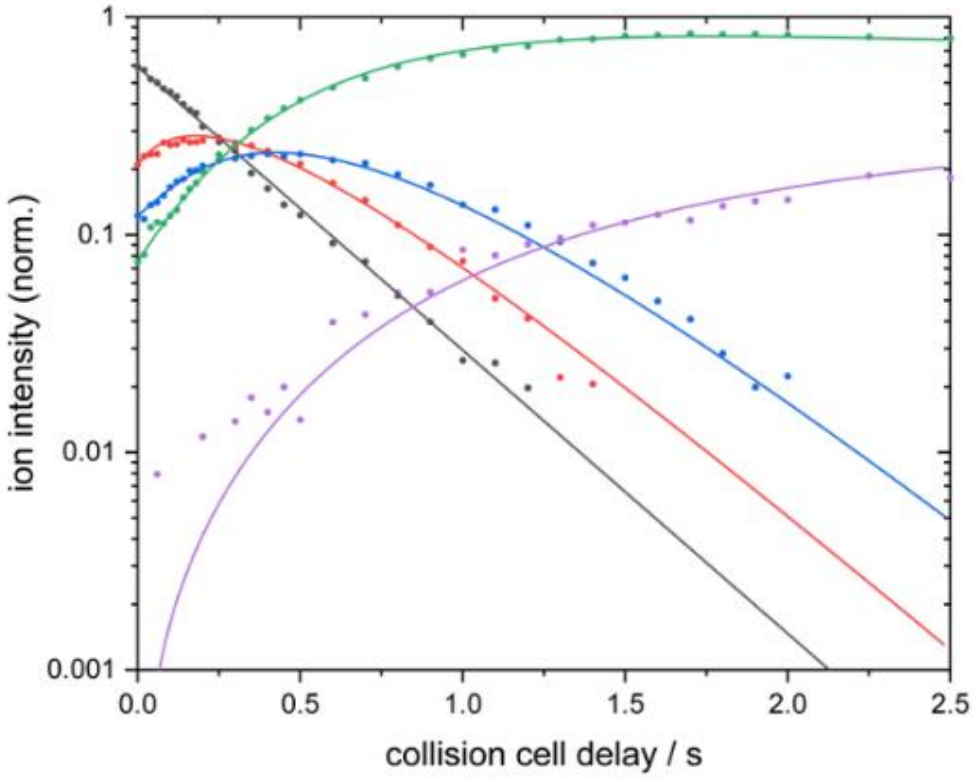


Fig. 6.7 Isothermal kinetics of the stepwise N_2 adsorption by $[Ru_8]^-$ within 26 K He buffer gas and 3.5 x 10^{-7} mbar of N_2 (solid points). Pseudo-first-order kinetic fits (solid

lines) were performed. The kinetic measurements reveal three fast adsorption steps, and the fourth one being particularly slow (cf. Fig. S3 in the SI).

The N_2 uptake kinetics of $[Ru_n]^-$ n = 7, 9 are stepwise and much in line with equivalent adsorption sites. (Figs. S1-S5) In contrast, the inspection of our recorded reaction kinetics, $[Ru_8]^-$ exhibited a rather unusual N_2 uptake performance (Fig. 5). There are three initial fast adsorption steps which are followed by a fourth one that proceeds exceptionally slowly (Figs. 5 and S3). The kinetic fits did not reveal any evidence for desorption of any of the first three N_2 molecules attached to the $[Ru_8]^-$ cluster. One may assume that the nitrogen molecules coordinate to the Ru atoms in a distal manner, that is such that they avoid direct neighborhood. Four such sites are possible at the edges of a cube. The net anionic charge of the cluster may localize at the fourth edge, distal to the three N_2 adsorbate bearing edges. Then adsorption of a fourth N_2 molecules would be significantly inhibited as unveiled by the indeed observed low adsorption rate $k_{(8,4)}$.

The IR-PD spectra of $[Ru_9(N_2)_m]^-$ m = 1,..,3 depict single N_2 adsorbate bands but shifted. The (9,1) IR-PD band at 1990 cm^{-1} reveals an exceptionally high red shift of 340 cm^{-1} with respect to the free N_2 vibration at 2330 cm^{-1}. This finds interpretation through a conceivable cubic structure of the bare cluster with an additional, less coordinated adatom that might serve as a preferred binding site for the first N_2 adsorbate. In accordance with the previous discussion of polarizabilities (cf. Tab. 1), it might be this less coordinated adatom which enhances polarizability, enables further π backdonation and causes the large red shift.

The more it comes as a surprise to find the large red shift of 340 cm^{-1} in (9,1) reducing to merely 260 cm^{-1} in $[Ru_9(N_2)_2]^-$ = (9,2). Note, that two potential N_2 ligands in (9,2) would signify through two IR-PD bands - but we find a single one. The experimental findings thus question the presences of two N_2 ligands in (9,2). Our DFT modelling managed to model (9,1) reasonably, cf. Fig. 6, but failed to find any $[Ru_9(N_2)_2]^-$ based structure that would yield a 2070 cm^{-1} vibration (scaled). However, this was found possible when exploring activated structures on the basis of di-nitride formation, namely $[Ru_9(N)_2(N_2)_1]^-$, see Fig.6. Apparently, the lowest coordinated Ru atom lost part of its local polarizability through the advent of two vicinal μ_2-bridged nitrido ligands next to it. Thereby, it allows for less

donation of electron density into the second N_2 entity and achieves less π back donation and thus reveals a significantly reduced red shift of the observed N_2 stretching vibration. Such an assumption is supported by the current, yet exploratory DFT calculations. Note, however, that it implies inert attachment of the first N_2 adsorbate and subsequent activation of the second one. Such a cooperative action amongst the N_2 adsorbates is conceivable but speculative at this point. It shall be elucidated in more detail by subsequent work.

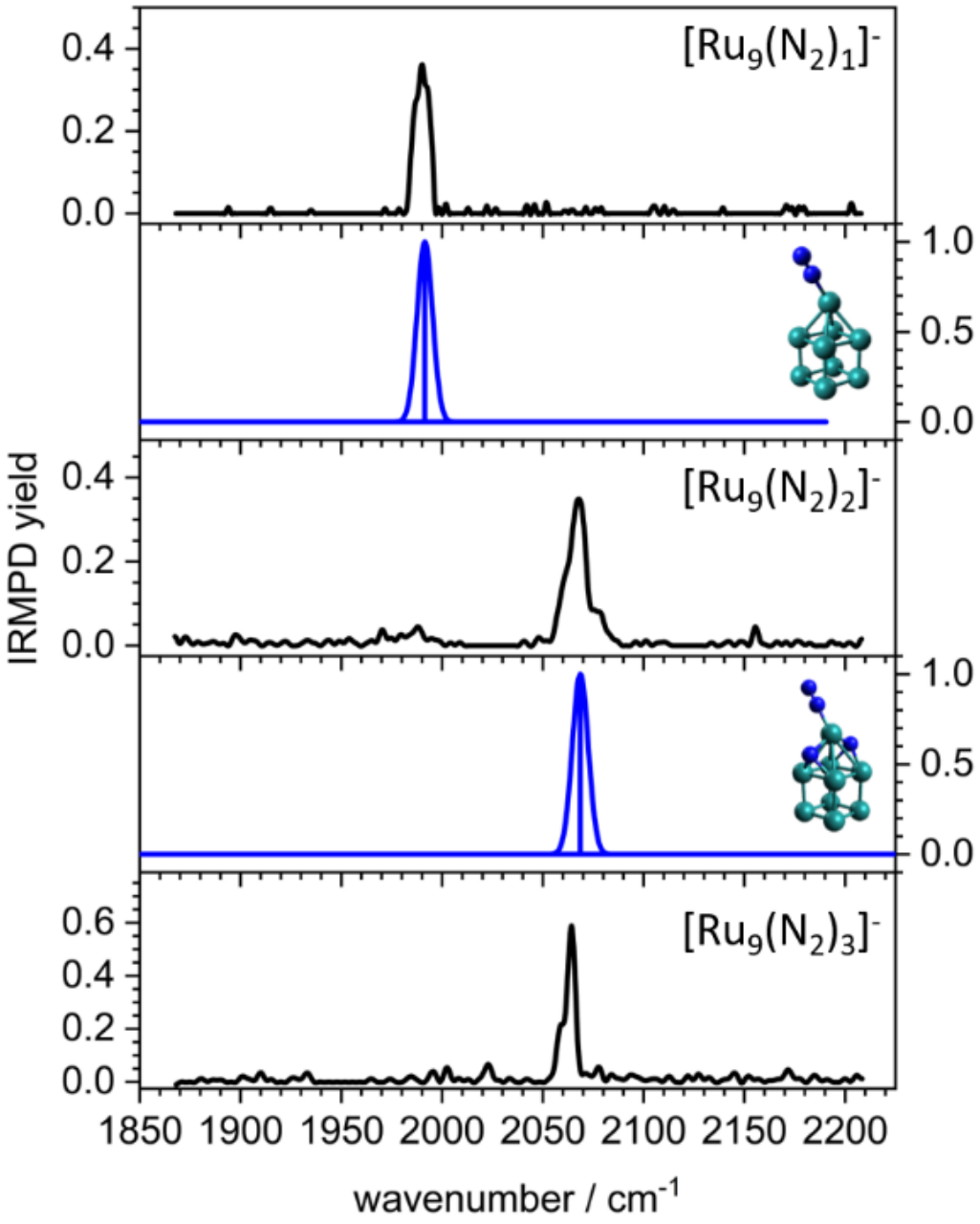


Fig. 6.8 IR-PD spectra of $[Ru_9(N_2)_m]^-$ for m = 1 – 3 (solid black line) and calculated IR spectra of m = 1 and 2 (solid blue line, predicted structures as insets). Note the N_2 activation in the case of m=2.

The achievable N_2 coverages m of the detected $[Ru_n(N_2)_m]^-$, n = 6-9 complexes increase stepwise during the interaction time within the cryo ion trap, up to an adsorption limit m_{max}. A Langmuir type single surface site – single adsorbate behavior would lead to a stoichiometric surface coverage of m_{max} = n, that would scale with the cluster size, up to the limit, where clusters possess some purely internal atom that do not achieve any exposure or access to the cluster surface. In the currently studied size range of n ≤ 10, this is clearly not the case. Nevertheless, the observed adsorption limits m_{max} stay clearly below n (cf. Fig. S6), but for the sole exception of n = 6 where m_{max} = 8. The found adsorption limit m_{max} = 4 is lowest in the case of n = 8. In remarkable contrast, the independently determined adsorption limit of the corresponding cationic clusters $[Ru_8(N_2)_m]^+$ is high, m_{max} = 8 [46]. None of these findings correlate with values of Table 1, and it becomes clear, that naked Ruthenium clusters experience quite an electronic reorganization upon covering with N_2 adsorbates. Further insights in these regards would require further experimental and further quantum chemical studies.

Finally, it is justified to have a look at the influence of the net charge on the ruthenium cluster properties. We have at hand some previously recorded yet unpublished data on IR-PD bands of $[Ru_n(N_2)_1]^+$ [46], and we compare these data to our current spectra of the anionic clusters $[Ru_n(N_2)_1]^-$ (Fig. 7). As to expect from a concerted σ donor - π acceptor action, the anionic clusters achieve higher red shifts of the N_2 stretching vibrations than the cationic ones. Some prior data of large neutral Ruthenium clusters [47] fall in between. Single size dependent variations of the observed IR-PD frequencies were discussed above in terms of cluster structures. Other than these, both, the measured IR-PD band positions of $[Ru_n(N_2)_1]^+$ and those of $[Ru_n(N_2)_1]^-$, follow linear but opposing trends. N_2 stretching band positions of cationic cluster N_2 complexes reveal an increasing red shift with increasing cluster sizes n. Those of anionic cluster complexes reveal a diminishing red shift with increasing cluster sizes n. An extrapolation towards large clusters (dashed

lines in Fig. 7), where a single extra charge would have almost no influence, would come close to the previously determined value of neutral clusters, 2126 cm^{-1}.

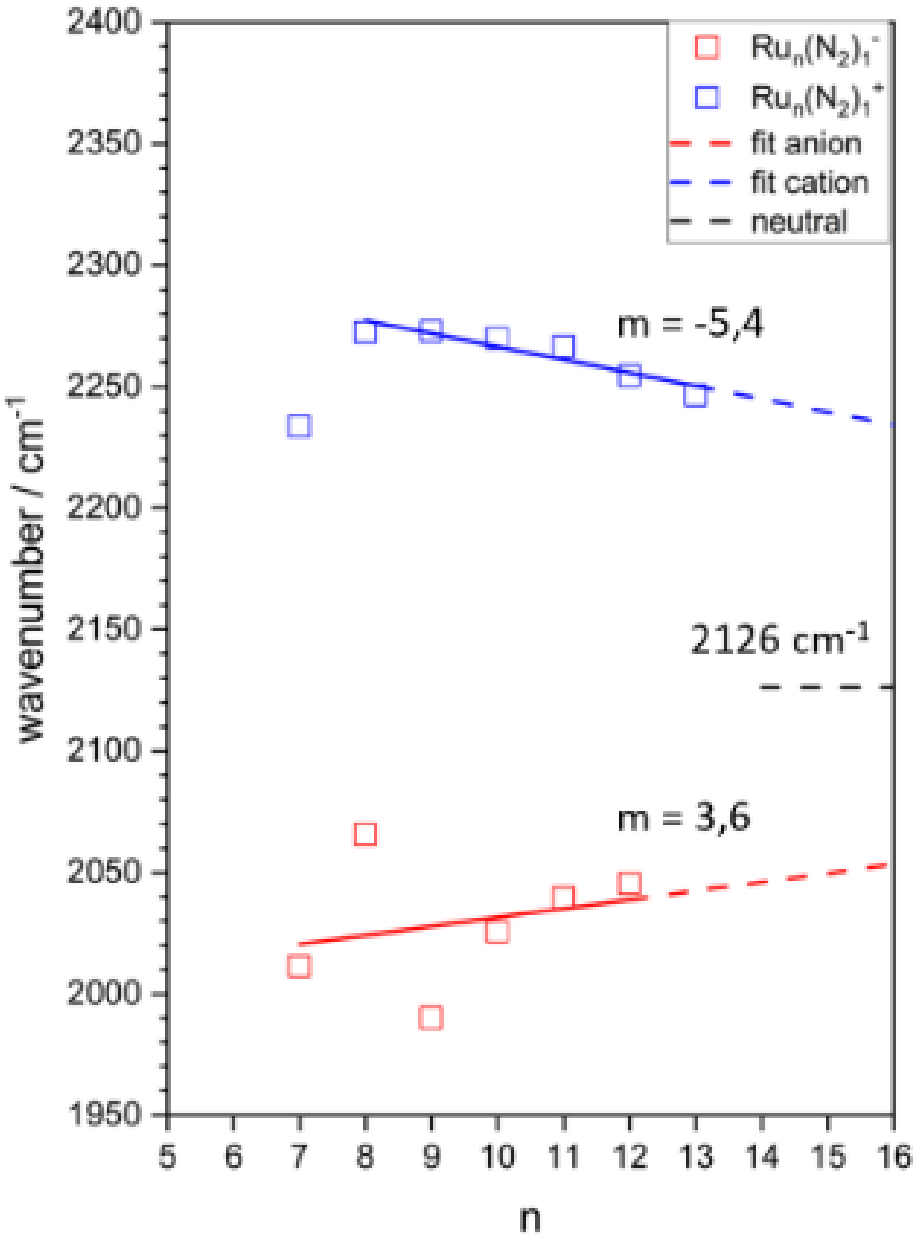


Fig. 6.9 Measured IR frequencies of $[Ru_n(N_2)_1]^{+/-}$, n = 7 – 13. The open blue squares represent cations, and the open red squares represent anions. The blue and red lines depict linear fits of the respective data, and the dashed lines extrapolate the observed trends towards larger clusters. They would cross at an IR frequency that was observed before for N_2 adsorbates on large neutral clusters.

6.6 Summary and Conclusions

This study presents N_2 uptake kinetics of anionic Ruthenium clusters $[Ru_n]^-$, n = 7-12 and IR-PD spectra of selected Ruthenium cluster – adsorbate complexes, $[Ru_n(N_2)_m]^-$, n = 7-12, m = 1-3, both recorded under isothermal cryo conditions (26 K), and presented together with quantum chemical modelling of selected cases. The uptake kinetics reveal large variations of the adsorption limit m_{max} by cluster size n, and evidence for some cases of notable N_2 desorption. The recorded IR-PD bands find interpretation as red shifted stretching modes of end on coordinated N_2 adsorbates. The varying band positions correlate with the calculated polarizability of the host clusters, which do vary by cluster size and cluster structure as well. This finding is well in line with established models of synergistic σ acceptor – π donor action amongst Ruthenium clusters and N_2 adsorbates. The case of $[Ru_9(N_2)_2]^-$ is particularly noteworthy, as the exploratory DFT modelling necessitates N_2 activation towards a di-nitrido motif, in order to model the shifted stretching band position of the other N_2 adsorbate. This finding shall be elucidated in more detail by subsequent work, which is underway as of now. Further insights arise from N_2 stretching band positions in cationic Ruthenium cluster – single N2 adsorbate complexes in comparison to those of anionic ones, and there is a close correspondence with published values of large neutral Ruthenium clusters.

6.7 Acknowledgments

This work was supported by the German research foundation DFG within the transregional collaborative research center SFB/TRR 88 “Cooperative effects in homo and heterometallic complexes” (3MET.de) and by the state research center OPTIMAS. The isotopically pure samples of ^{102}Ru were supplied by the United States Department of Energy Office of Science by the Isotope Program in the Office of Nuclear Physics. We thank Sebastian Dillinger and Jennifer Mohrbach for the recording of the IRPD frequencies of $[Ru_n(N_2)_1]^+$.

6.8 Author Contributions

CW and ML conducted all experiments at instrumentation of the GNS lab. CW conducted the DFT calculations and wrote the first draft of the manuscript, revised by GNS and finalized by all authors.

6.9 References

[1] X.-Y. Quek, Y. Guan , R. A. van Santen, E. J. M. Hensen, 'Unprecedented Oxygenate Selectivity in Aqueous-Phase Fischer–Tropsch Synthesis by Ruthenium Nanoparticles', *ChemCatChem* **2011**, *3*, 1735-1738.

[2] D. L. King, 'A Fischer-Tropsch study of supported ruthenium catalysts', *J. Catal.* **1978**, *51*, 386-397.

[3] F. R. García-García, A. Guerrero-Ruiz, I. Rodríguez-Ramos, 'Role of B5-Type Sites in Ru Catalysts used for the NH_3 Decomposition Reaction', *Top. Catal.* **2009**, *52*, 758-764.

[4] C. J. H. Jacobsen, S. Dahl, P. L. Hansen, E. Törnqvist, L. Jensen, H. Topsøe, D. V. Prip, P. B. Møenshaug, I. Chorkendorff, 'Structure Sensitivity of Supported Ruthenium Catalysts for Ammonia Synthesis', *J. Mol. Catal. A: Chem.* **2000**, *163*, 19.

[5] A. Logadottir, T. H. Rod, J. K. Nørskov, B. Hammer, S. Dahl, C. J. H. Jacobsen, 'The Brønsted–Evans–Polanyi Relation and the Volcano Plot for Ammonia Synthesis over Transition Metal Catalysts', *J. Catal.* **2001**, *197*, 229-231.

[6] S. Shetty, A. P. J. Jansen, R. A. van Santen, 'Active Sites for N_2 Dissociation on Ruthenium', *The Journal of Physical Chemistry C* **2008**, *112*, 17768-17771.

[7] R. van Hardeveld, A. van Montfoort, 'The influence of crystallite size on the adsorption of molecular nitrogen on nickel, palladium and platinum: An infrared and electron-microscopic study', *Surf. Sci.* **1966**, *4*, 396-430.

[8] H. Bielawa, O. Hinrichsen, A. Birkner, M. Muhler, 'The Ammonia-Synthesis Catalyst of the Next Generation: Barium-Promoted Oxide-Supported Ruthenium', *Angew. Chem. Int. Ed.* **2001**, *40*, 1061-1063.

[9] A. J. Cox, J. G. Louderback, S. E. Apsel, L. A. Bloomfield, 'Magnetism in 4d-Transition Metal Clusters', *Phys. Rev. B: Condens. Matter Mater. Phys.* **1994**, *49*, 12295.

[10] J. T. Lyon, P. Gruene, A. Fielicke, G. Meijer, D. M. Rayner, 'Probing C-O Bond Activation on Gas-Phase Transition Metal Clusters: Infrared Multiple Photon Dissociation Spectroscopy of Fe, Ru, Re, and W Cluster CO Complexes', *J. Chem. Phys.* **2009**, *131*, 184706.

[11] R. A. de Paola, F. M. Hoffmann, D. Heskett, E. W. Plummer, 'Adsorption of molecular nitrogen on clean and modified Ru(001) surfaces: The role of σ bonding', *Physical Review B* **1987**, *35*, 4236-4249.

[12] H. Shi, K. Jacobi, 'Evidence for physisorbed N_2 in the monolayer on Ru(001) at 40 K', *Surf. Sci.* **1992**, *278*, 281-285.

[13] H. Shi, K. Jacobi, G. Ertl, 'Dissociative Chemisorption of Nitrogen on Ru(0001)', *J. Chem. Phys.* **1993**, *99*, 9248.

[14] M. Kitano, Y. Inoue, Y. Yamazaki, F. Hayashi, S. Kanbara, S. Matsuishi, T. Yokoyama, S.-W. Kim, M. Hara, H. Hosono, 'Ammonia synthesis using a stable electride as an electron donor and reversible hydrogen store', *Nature Chemistry* **2012**, *4*, 934-940.

[15] S. Mark, C. Schellhammer, G. Niedner-Schatteburg, D. Gerlich, 'Guided ion beam studies of scattering dynamics and energy disposal: The $CD_3^+ + C_2H_6$ and the $CD_3^+ + C_3H_8$ case', *J. Phys. Chem.* **1995**, *99*, 15587-15594.

[16] M. Z. Kamrath, R. A. Relph, T. L. Guasco, C. M. Leavitt, M. A. Johnson, 'Vibrational predissociation spectroscopy of the H_2-tagged mono- and dicarboxylate anions of dodecanedioic acid', *Int. J. Mass spectrom.* **2011**, *300*, 91-98.

[17] O. Asvany, S. Brünken, L. Kluge, S. Schlemmer, 'COLTRAP: a 22-pole ion trapping machine for spectroscopy at 4 K', *Appl. Phys. B* **2014**, *114*, 203-211.

[18] H. Schwarz, K. R. Asmis, 'Identification of Active Sites and Structural Characterization of Reactive Ionic Intermediates by Cryogenic Ion Trap Vibrational Spectroscopy', *Chem. Eur. J.* **2019**, *25*, 2112-2126.

[19] N. Heine, K. R. and Asmis, 'Cryogenic ion trap vibrational spectroscopy of hydrogen-bonded clusters relevant to atmospheric chemistry', *Int. Rev. Phys. Chem.* **2015**, *34*, 1-34.

[20] O. V. Boyarkin, V. Kopysov, 'Cryogenically cooled octupole ion trap for spectroscopy of biomolecular ions', *Rev. Sci. Instrum.* **2014**, *85*, 033105.

[21] S. Dillinger, J. Mohrbach, J. Hewer, M. Gaffga, G. Niedner-Schatteburg, 'Infrared Spectroscopy of N_2 Adsorption on Size Selected Cobalt Cluster Cations in Isolation', *Phys. Chem. Chem. Phys.* **2015**, *17*, 10358.

[22] O. P. Balaj, C. B. Berg, S. J. Reitmeier, V. E. Bondybey, M. K. Beyer, 'A novel design of a temperature-controlled FT-ICR cell for low-temperature black-body infrared radiative dissociation (BIRD) studies of hydrated ions', *Int. J. Mass spectrom.* **2009**, *279*, 5-9.

[23] C. Joblin, C. Pech, M. Armengaud, P. Frabel, P. Boissel, 'A piece of interstellar medium in the laboratory: the PIRENEA experiment', *EAS Publications Series* **2002**, *4*, 73.

[24] L. Fritsche, A. Bach, L. Miloglyadova, A. Tsybizova, P. Chen, 'A 4 K FT-ICR cell for infrared ion spectroscopy', *Rev. Sci. Instrum.* **2018**, *89*.

[25] S. Dillinger, G. Niedner-Schatteburg, in *Fundamentals and Applications of Fourier Transform Mass Spectrometry* (Eds.: B. Kanawati, P. Schmitt-Kopplin), Elsevier, 2019, pp. 593-621.

[26] A. Tsybizova, L. Fritsche, L. Miloglyadova, B. Kräutler, P. Chen, 'Cryogenic Ion Vibrational Predissociation (CIVP) Spectroscopy of Aryl Cobinamides in the Gas Phase: How Good Are the Calculations for Vitamin B12 Derivatives?', *J. Am. Chem. Soc.* **2023**, *145*, 19561-19570.

[27] V. Gorbachev, A. G. Nobile, A. Tsybizova, P. Chen, 'Probing Electronic Effects in Tridentate Copper(I) Complexes by CIVP Spectroscopy', *Inorg. Chem.* **2023**, *62*, 14704-14714.

[28] A. Fielicke, 'Probing the binding and activation of small molecules by gas-phase transition metal clusters via IR spectroscopy', *Chem. Soc. Rev.* **2023**, *52*, 3778-3841.

[29] S. Dillinger, J. Mohrbach, G. Niedner-Schatteburg, 'Probing cluster surface morphology by cryo spectroscopy of N_2 on cationic nickel clusters', *J. Chem. Phys.* **2017**, *147*, 184305.

[30] A. A. Ehrhard, M. P. Klein, J. Mohrbach, S. Dillinger, G. Niedner-Schatteburg, 'Cryo kinetics of N_2 adsorption onto bimetallic rhodium-iron clusters in isolation', *J. Chem. Phys.* **2022**, *156*.

[31] D. V. Fries, M. P. Klein, A. Steiner, M. H. Prosenc, G. Niedner-Schatteburg, 'Observation and mechanism of cryo N_2 cleavage by a tantalum cluster', *Physical Chemistry Chemical Physics* **2021**, *23*, 11345-11354.

[32] M. P. Klein, A. A. Ehrhard, M. E. Huber, A. Straßner, D. V. Fries, S. Dillinger, J. Mohrbach, G. Niedner-Schatteburg, 'Cryo infrared spectroscopy of N_2 adsorption onto bimetallic rhodium-iron clusters in isolation', *J. Chem. Phys.* **2022**, *156*.

[33] M. P. Klein, A. A. Ehrhard, J. Mohrbach, S. Dillinger, G. Niedner-Schatteburg, 'Infrared Spectroscopic Investigation of Structures and N_2 Adsorption Induced Relaxations of Isolated Rhodium Clusters', *Top. Catal.* **2018**, *61*, 106-118.

[34] J. Mohrbach, S. Dillinger, G. Niedner-Schatteburg, 'Cryo Kinetics and Spectroscopy of Cationic Nickel Clusters: Rough and Smooth Surfaces', *J. Phys. Chem. C* **2017**, *121*, 10907-10918.

[35] D. V. Fries, M. P. Klein, A. Steiner, M. H. Prosenc, G. Niedner-Schatteburg, 'Observation and mechanism of cryo N2cleavage by a tantalum cluster', *Physical Chemistry Chemical Physics* **2021**, *23*, 11345-11354.

[36] D. V. Fries, M. P. Klein, A. Straßner, M. E. Huber, M. Luczak, C. Wiehn, G. Niedner-Schatteburg, 'Cryo IR spectroscopy and cryo kinetics of dinitrogen activation and cleavage by small tantalum cluster cations', *J. Chem. Phys.* **2023**, *159*.

[37] D. V. Fries, M. P. Klein, A. Straßner, M. E. Huber, G. Niedner-Schatteburg, 'Cryo-IR spectroscopy and cryo-kinetics of cluster N_2 adsorbate complexes of tantalum cluster cations $Ta_{5\text{-}8}^{+}$', *J. Chem. Phys.* **2023**, *159*.

[38] E. Waldt, A. S. Hehn, R. Ahlrichs, M. M. Kappes, D. Schooss, 'Structural Evolution of Small Ruthenium Cluster Anions', *J. Chem. Phys.* **2015**, *142*, 024319/024311.

[39] C. Kerpal, D. J. Harding, D. M. Rayner, J. T. Lyon, A. Fielicke, 'Far-IR Spectra and Structures of Small Cationic Ruthenium Clusters: Evidence for Cubic Motifs', *The Journal of Physical Chemistry C* **2015**, *119*, 10869-10875.

[40] S. Dillinger, M. P. Klein, A. Steiner, D. C. McDonald, II, M. A. Duncan, M. M. Kappes, G. Niedner-Schatteburg, 'Cryo IR Spectroscopy of N_2 and H_2 on Ru_8^{+}: The Effect of N_2 on the H-Migration', *J. Phys. Chem. Lett.* **2018**, *9*, 914-918.

[41] C. Adamo, V. Barone, 'Toward Reliable Density Functional Methods without Adjustable Parameters: The PBE0Model', *J. Chem. Phys.* **1999**, *110*, 6158.

[42] T. H. Dunning, 'Gaussian-Basis Sets for Use in Correlated Molecular Calculations 1. The Atoms Boron through Neon and Hydrogen', *J. Chem. Phys.* **1989**, *90*, 1007.

[43] K. A. Peterson, D. Figgen, M. Dolg, H. Stoll, 'Energy-consistent relativistic pseudopotentials and correlation consistent basis sets for the 4d elements Y–Pd', *The Journal of Chemical Physics* **2007**, *126*, 124101.

[44] M. J. Frisch, G. W. Trucks, H. B. Schlegel, G. E. Scuseria, M. A. Robb, J. R. Cheeseman, G. Scalmani, V. Barone, G. A. Petersson, H. Nakatsuji, X. Li, M. Caricato, A. V. Marenich, J. Bloino, B. G. Janesko, R. Gomperts, B. Mennucci, H. P. Hratchian, J. V. Ortiz, A. F. Izmaylov, J. L. Sonnenberg, Williams, F. Ding, F. Lipparini, F. Egidi, J. Goings, B. Peng, A. Petrone, T. Henderson, D. Ranasinghe, V. G. Zakrzewski, J. Gao, N. Rega, G. Zheng, W. Liang, M. Hada, M. Ehara, K. Toyota, R. Fukuda, J. Hasegawa, M. Ishida, T. Nakajima, Y. Honda, O. Kitao, H. Nakai, T. Vreven, K. Throssell, J. A. Montgomery Jr., J. E. Peralta, F. Ogliaro, M. J. Bearpark, J. J. Heyd, E. N. Brothers, K. N. Kudin, V. N. Staroverov, T. A. Keith,

R. Kobayashi, J. Normand, K. Raghavachari, A. P. Rendell, J. C. Burant, S. S. Iyengar, J. Tomasi, M. Cossi, J. M. Millam, M. Klene, C. Adamo, R. Cammi, J. W. Ochterski, R. L. Martin, K. Morokuma, O. Farkas, J. B. Foresman, D. J. Fox, Wallingford, CT, 2016.

[45] J. Chatt, L. A. Duncanson, '586. Olefin co-ordination compounds. Part III. Infra-red spectra and structure: attempted preparation of acetylene complexes', *J. Chem. Soc.* **1953**, 2939-2947.

[46] S. Dillinger, J. Mohrbach, G. Niedner-Schatteburg, *(unpublished)*.

[47] C. Kerpal, D. J. Harding, J. T. Lyon, G. Meijer, A. Fielicke, 'N_2 Activation by Neutral Ruthenium Clusters', *J. Phys. Chem. C* **2013**, *117*, 12153.

6.10 Supporting information

Nitrogen adsorption and activation
on size selected ruthenium cluster anions
under cryo conditions in isolation

Christopher Wiehn[a,b], Maximilian Luczak[a,c] and Gereon Niedner-Schatteburg[a,d]

[a]Department of Chemistry, RPTU, 67663 Kaiserslautern, Germany

[b]present address: Defense Logistics Agency, Rhine Ordnance Barracks, 67663 Kaiserslautern, Germany

[c] present address: Math2Market GmbH, 67655 Kaiserslautern, Germany

[d]State Research Center OPTIMAS, RPTU, 67663 Kaiserslautern, Germany

Text S1 On the nomenclature of N_2 adsorption and desorption steps

Fig. S1 Isothermal kinetics of the stepwise N_2 adsorption by $[Ru_7]^-$

Fig. S2 Rate constants by the fitted uptake kinetics of $Ru_7^- + N_2$

Fig. S3 Rate constants by the fitted uptake kinetics of $Ru_8^- + N_2$

Fig. S4 Isothermal kinetics of the stepwise N_2 adsorption by $[Ru_9]^-$

Fig. S5 Rate constants by the fitted uptake kinetics of $Ru_9^- + N_2$

Fig. S6 Observed adsorption limits of $[Ru_n(N_2)_m]^-$, n = 6-9

Fig. S7 Calculated structure of $[Ru_9]^-$

Text S1 On the nomenclature of N_2 adsorption and desorption steps.

The pseudo-first-order fits performed yield relative rate constants for all adsorption steps $k_{(n,m)}$ and desorption steps $k_{-(n,m+1)}$ according to the scheme:

$$[Ta_n(N_2)_{m-1}]^+ + 2\,N_2 \underset{\boldsymbol{k_{-(n,m)}}}{\overset{k_{(n,m-1)}}{\rightleftarrows}} [\boldsymbol{Ta_n(N_2)_m}]^+ + N_2 \underset{k_{-(n,m+1)}}{\overset{\boldsymbol{k_{(n,m)}}}{\rightleftarrows}} [Ta_n(N_2)_{m+1}]^+$$

This nomenclature is in line with that of our previous publications, and it is defined as to indicate, that a cluster-adsorbate complex $[\boldsymbol{Ta_n(N_2)_m}]^+$, potentially abbreviated as

(n,m), adsorbs an N_2 molecule by the rate constant $\boldsymbol{k}_{(n,m)}$ and desorbs an N_2 molecule by the rate constant $\boldsymbol{k}_{-(n,m)}$. Particular values of these rate constants stem from kinetic fits to observed kinetic measurements.

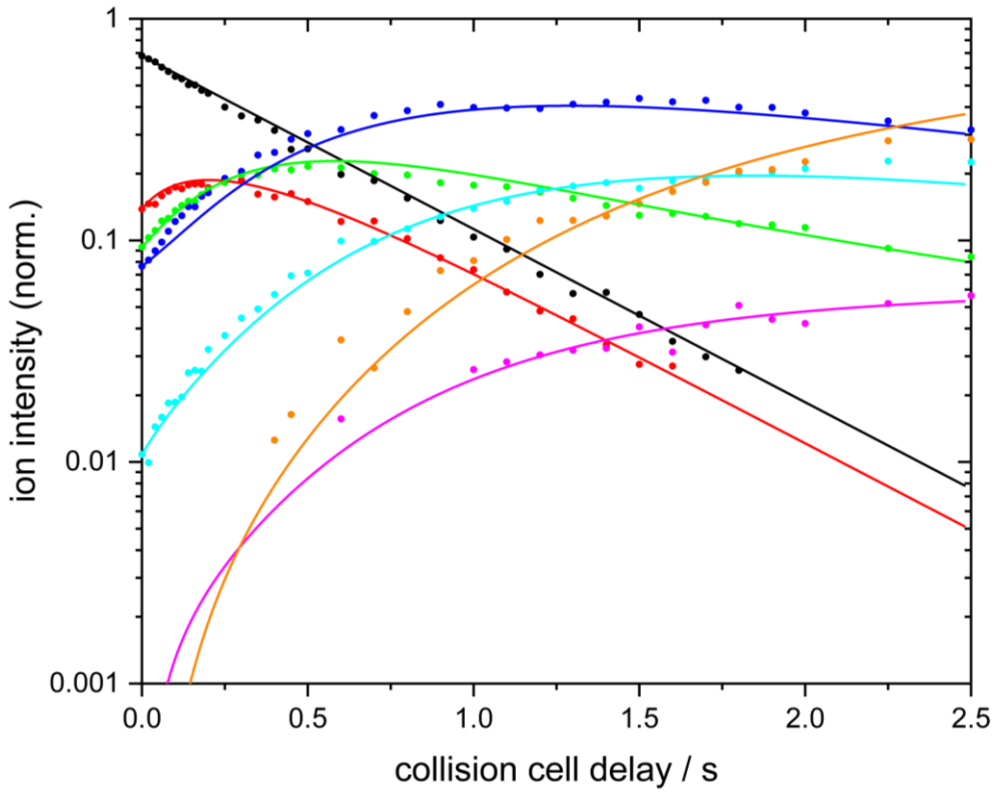


Fig. S1 Isothermal kinetics of the stepwise N_2 adsorption by $[Ru_7]^-$. The reactions took place within a 26 K He buffer gas and at 3.5 x 10^{-7} mbar of N_2 (solid points), and they were fitted by pseudo-first-order kinetic (solid lines). Consecutive uptake takes place up to an adsorption limit of six N_2 molecules.

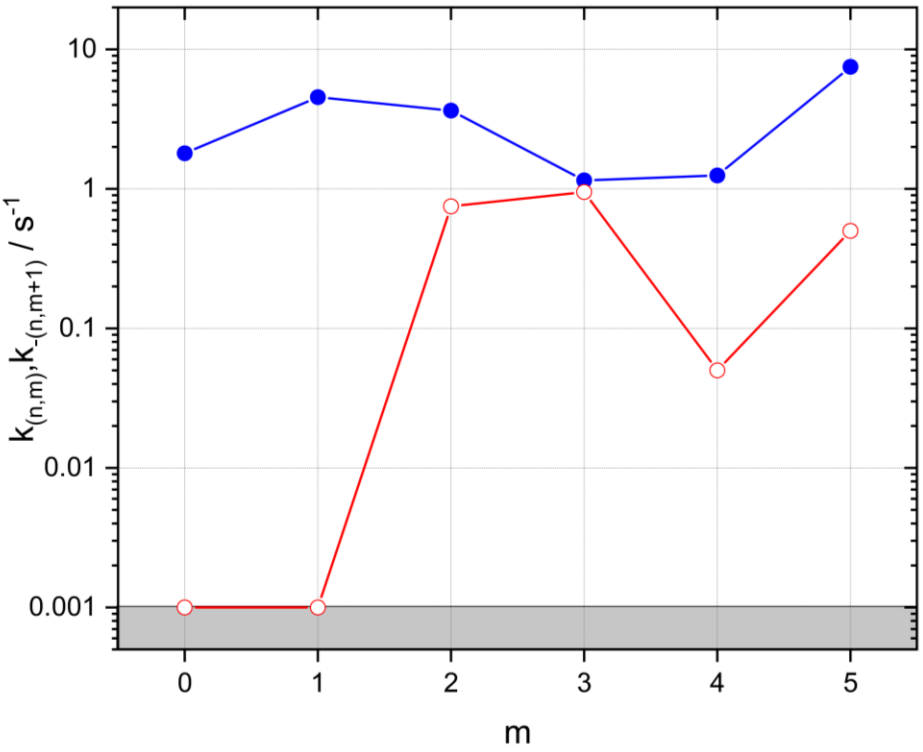


Fig. S2 Rate constants by the fitted uptake kinetics of Ru_7^- + N_2 as a function of N_2 adsorption ($k_{(n,m)}$, blue dots) and N_2 desorption ($k_{(n,m+1)}$, red circles). For the definition of m see Text S1.

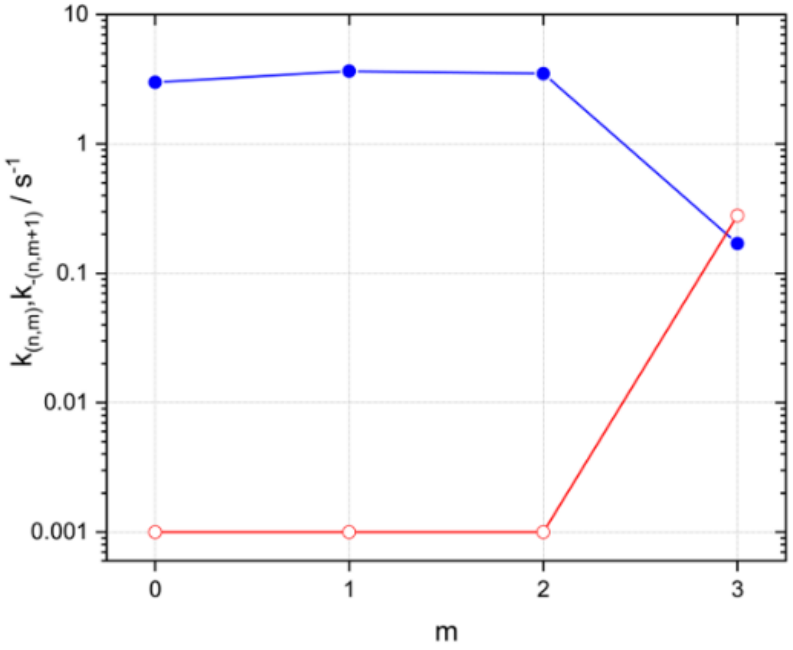


Fig. S3 Rate constants by the fitted uptake kinetics of Ru_8^- + N_2 as a function of N_2 adsorption (blue dots) and N_2 desorption (red circles). For the definition of m see Text S1.

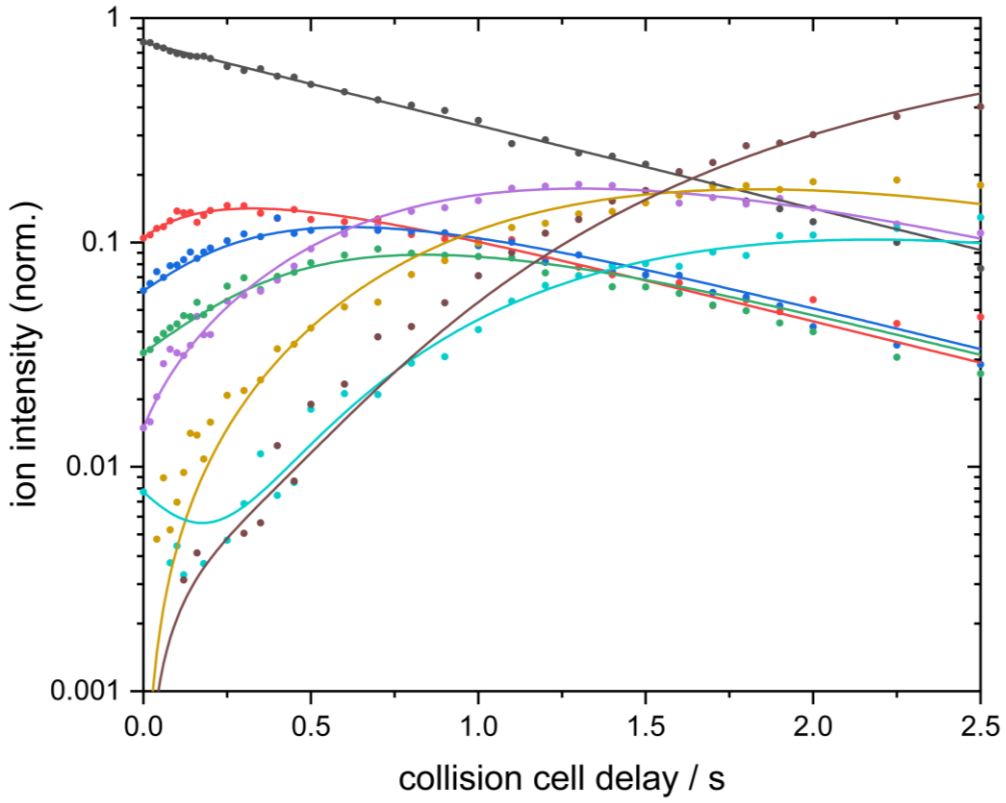


Fig. S4 Isothermal kinetics of the stepwise N_2 adsorption by $[Ru_9]^-$. The reactions took place within a 26 K He buffer gas and at 3.5 x 10^{-7} mbar of N_2 (solid points), and they were fitted by pseudo-first-order kinetic (solid lines). Consecutive uptake takes place up to an adsorption limit of seven N_2 molecules.

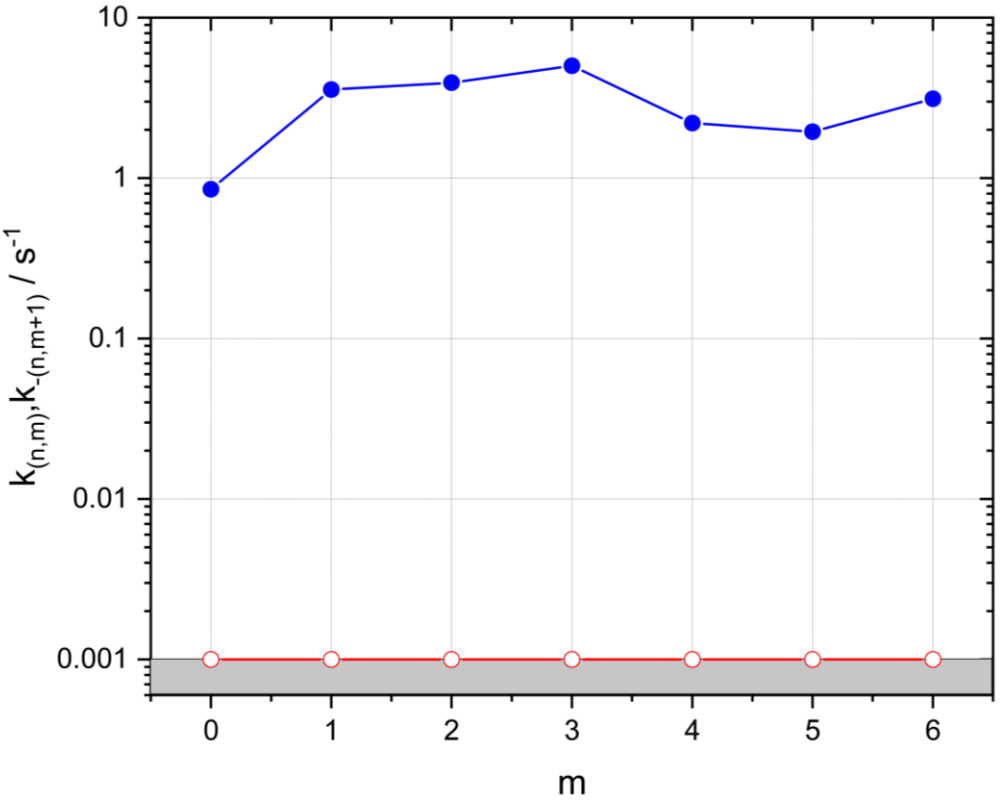


Fig. S5 Rate constants by the fitted uptake kinetics of Ru_9^- + N_2 as a function of N_2 adsorption (blue dots) and N_2 desorption (red circles). For the definition of m see Text S1.

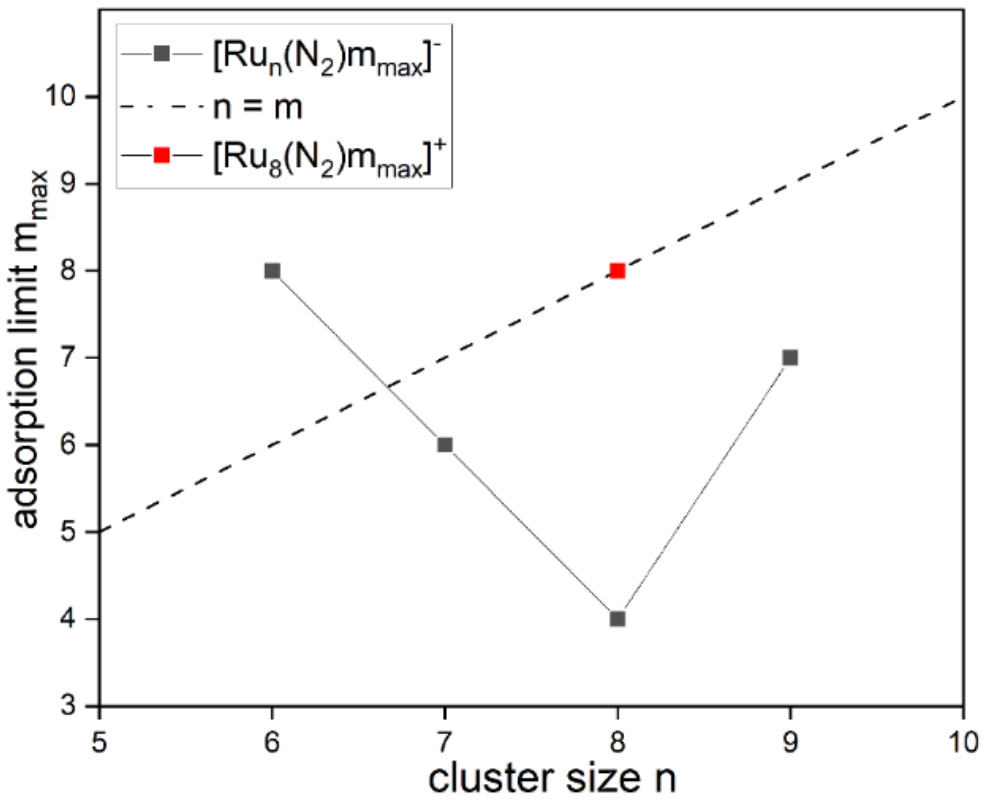


Fig. S6 Observed adsorption limits of $[Ru_n(N_2)_m]^-$, n = 6-9. The dashed line would indicate a stoichiometric N_2 uptake, the case of $m_{max} = n$.

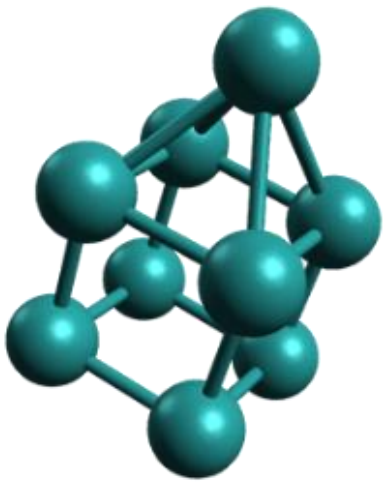


Fig. S7 Calculated structure of $[Ru_9]^-$, obtained at the PBE0/ecp28mdf level of theory. This cubic motif was assigned before by Waldt et al. on the basis of their trapped ion electron diffraction (TIED) experiments.{Waldt, 2015 #33}

7 Activation of dinitrogen on anionic ruthenium clusters

7.1 Preamble

The experiments in this work have been conducted by Maximilian Luczak and Christopher Wiehn in equal parts at RPTU Kaiserslautern's FRITZ lab. The quantum chemical models have been performed by Christopher Wiehn, using Gaussian 16 software package run on the RPTU Kaiserslautern computing center. The results were discussed among Maximilian Luczak, Christopher Wiehn and Prof. Gereon Niedner-Schatteburg. The following paper was drafted by Maximilian Luczak and Gereon Niedner-Schatteburg.

7.2 Introduction

Ruthenium is a catalytical active transition metal. It is the catalyst of the ammonia synthesis in the Kellogg Advanced Ammonia Process (KAAP).[1] Contrasting to the iron based catalysts used in the Haber-Bosch process[2], ruthenium catalysts allow for milder reaction conditions and thus save energy and resources in one of the central chemical processes worldwide.[3]

The industrial fixation of dinitrogen follows the steps proposed by Ertl. et al.[4] The first step is the adsorption of molecular dinitrogen to the catalytical active metal. In the second step the strong triple bond of the dinitrogen molecule has to be broken and cleaved. This step is called nitrogen activation. In the following steps hydrogen, adsorbed to the metal surface combines with the nitrogen atoms und form ammonia.

The adsorption and activation of dinitrogen follows a sigma donor-pi acceptor synergism, as proposed by Blyholder et al.[5] and Dewar-Chatt and Duncanson.[6] Electron density is transferred from the metal surface to the anti-binding pi* orbital of the dinitrogen triple bond. This process can eventually lead to a cleavage of the triple bond and the generation of nitrogen.

In industrial ammonia synthesis processes, such as the KAAP, ruthenium dotations are places on electride structures. These structures often use promotors, such as potassium,

to increase the electron density present in the catalytic centers to facilitate the cleavage of dinitrogen. [7]

To study the elementary steps of nitrogen activation in great detail, cluster chemistry studies provide complementary insights alongside studies of bulk systems or single atom organometallic chemistry.[8] The adsorption and activation of dinitrogen on transition metal (TM) clusters under cryo-conditions have been studied with differing cluster sizes, metals and charge states. Studies with cationic tantalum clusters were able to provide a detailed reaction coordinate of the activation and cleavage of adsorbed dinitrogen. Studies of positive ruthenium clusters were performed alongside hydrogen-nitrogen co-adsorption studies. Lately more studies of anionic cobalt and nickel clusters have provided insights into the activation process. In this study we will focus on anionic ruthenium clusters with dinitrogen adsorbed to the cluster surface under cryo-conditions.

The investigation of ruthenium – dinitrogen complexes under cryo-conditions allows us to review the pick-up of dinitrogen by the cluster at 40 K. Furthermore, we perform IR-PD experiments on size selected complexes with an IR light source to focus on the stretching mode of dinitrogen at 2330 cm^{-1}, which will give us a good impression on the activation of the triple bond. Additionally, the comparison to quantum chemical ab initio DFT modeling will give further insights on the geometry of the cluster-adsorbate complex and the elementary steps of dinitrogen activation.

7.3 Experimental

All experiments were conducted using a customized Fourier transform-ion cyclotron resonance (FT-ICR) mass spectrometer (Apex Ultra Bruker Daltonics), specifically, cluster production, isolation, N_2 adsorption, infrared photodissociation (IR-PD) spectroscopy, and mass analysis. The metal cluster ions were generated from a monoisotopic 102Ru (99.38%, Oak Ridge National Laboratories) foil using a home-built laser vaporization source. We were able to obtain clusters in the size range of n = 4 – 12, with n = 5 missing and n = 6 will be the topic of a separate publication. Following mass selection, Ru clusters of sizes n = 7, 8, 9, 10, 11, or 12 were stored in a cryogenic hexapole ion trap (cooled to 26

K). The reaction gas (in this case N_2) was continuously introduced up to a pressure of 4.0 × 10−7 mbar to yield sufficient reaction products. Helium was used as a buffer gas (up to 4.0 × 10−6 mbar) to achieve efficient trapping and cooling. After a variable storage time (0−2.5 s), the ions were guided into the FT-ICR cell, which was held at a temperature below 10 K. The cell was used for isolation, further storage, and ion detection.

To record kinetics, the formed $[Ru_8(N_2)_m]^-$ cluster adsorbate complexes were detected in the ICR cell in dependence to their storage time in the collision cell. A pseudo-first-order kinetic model was used to fit the obtained data, which allowed us to determine the pseudo-first-order rate constants for the individual adsorption steps. For a more detailed description of the kinetic data recording and analysis refer to Ref 22.

A Nd: YAG pump laser (Continuum DLS 8000, 10 Hz, 0,55 J/pulse) was coupled with an OPO/OPA setup (LaserVision, KTP/KTA) and a DFM stage to generate IR radiation in the range of 1000 – 2400 cm^{-1}. IR spectra were obtained by recording the fragmentation spectra of the ions while continuously scanning the IR wavelength. The ions were irradiated for 0.2 – 0.4 s in the ICR Cell. The IRPD signal was evaluated as $\Sigma_i F_i / (\Sigma_i F_i + \Sigma_i P_i)$, where F_i indicates the fragment ion signal and P_i is the parent ion signal. By plotting the fragmentation efficiency as a function of the laser frequency, the IR-PD spectra can be obtained. In this work we recorded IR-PD spectra in the range of 1870 – 2210 cm^{-1} of the $[Ru_n(N_2)_m]^-$ (n = 7 – 12, m = 1 – 3 for n = 7 – 9 and m = 1 for n = 10 - 12) species.

DFT calculations were performed using the hybrid functional PBE0, the cc-pVTZ basis set[15](N) and the effective core potential ecp28mdf provided by the Stuttgart/Cologne group[9] and the Gaussian 16 program package.[10] All calculations were checked for imaginary frequencies and calculated using the standard convergence criterion (10^{-8}).

7.4 Results and Discussion

The IR-PD spectrum of Ru6(N2)n- does not show a IR signal in the range from 1860 to 2330 cm^{-1}.(See fig.1 fist spectrum) Two possibilities can lead to a absence of an IR stretching mode in the spectrum. One is the absence of a fragmentation path. In order to record a IR-PD spectrum with the action spectroscopy method, the fragmentation of the cluster-adsorbate complex is necessary. The lighter charged fragment can be recorded and correlated with the incoming wavelength yields an IR-PD spectrum. The second

possibility is the absence of a chromophore in the used IR spectrum. This implies the absence of dinitrogen and hence the splitting of the dinitrogen bond and generation of two nitrides.

To determine which possibility is more likely, we recorded IR-PD spectra the following adsorption steps. The IR-PD spectra of $Ru_6(N_2)_2^-$ and $Ru_6(N_2)_3^-$ show IR signals at 2030 cm^{-1} and 2040 cm^{-1}. This indicates the presence of intact dinitrogen in the cluster-adsorbate complex, but the resolution of the band structure does not allow for a analysis of the cluster geometry. The IR-PD spectrum of $Ru_6(N_2)_4^-$ shows three IR signals at 2020 cm^{-1}, 2035 cm^{-1} and 2045 cm^{-1}. The signals are well resolved and allow for an analysis of the cluster structure with calculated IR spectra of DFT ab initio modeling.

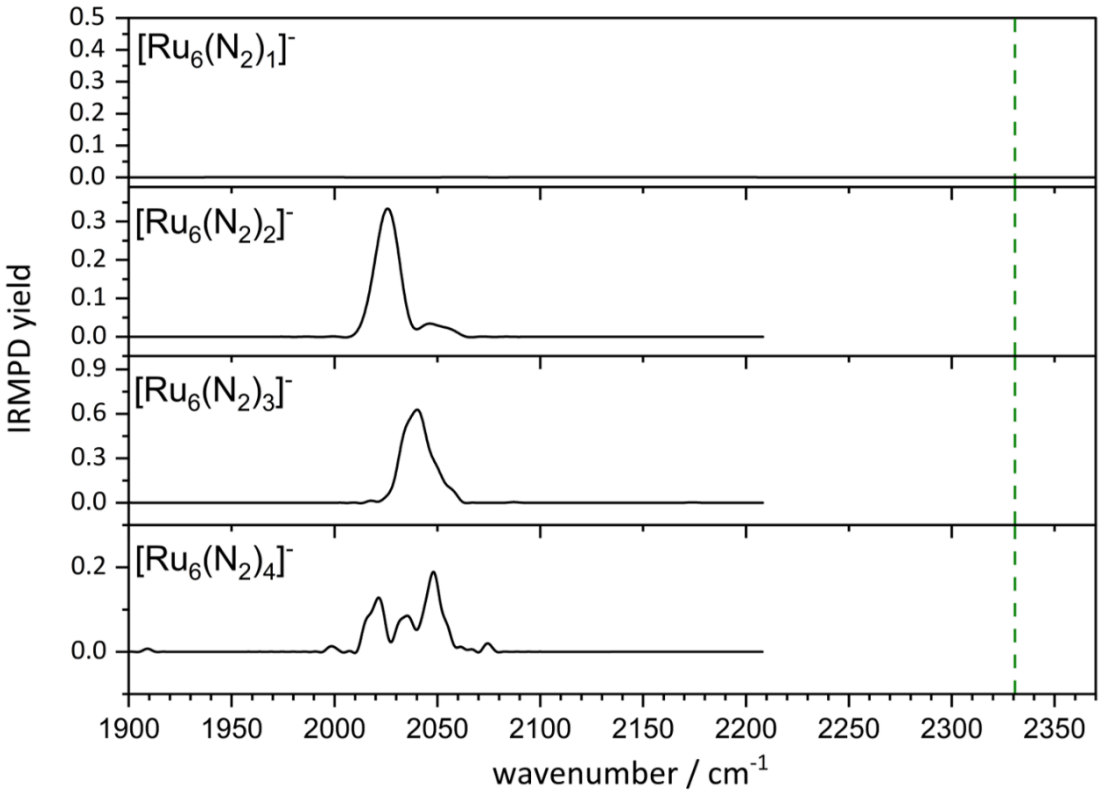


Fig. 7.1: IR-PD spectra of $Ru_6(N_2)_n^-$ (n=1-4) in the range from 1900 cm^{-1} to 2210 cm^{-1}. The green dotted line represents the location of the free dinitrogen stretching mode at 2330 cm^{-1}.

The comparison of the modeled structures with the experimental spectra are displayed in fig. 2. The experimental spectrum is displayed on the top in solid black lines, the calculated IR spectra are displayed as blue solid lines. The different simulated spectra are labeled with the relative formation enthalpies, and a structural description. Nitrides indicate the presence of cleaved dinitrogen, end-on represents intact dinitrogen molecules adsorbed in a end-on position to the cluster surface.

The structure of the experimental IR spectrum is described well by the simulated IR spectrum shown in the second, fourth and fith row. Since the absolute position of IR signals in simulated spectra is not very well dependable and is influenced by the scaling factor. The splitting between the IR signals gives a better indication of the comparability of the simulated geometry and its' IR spectrum and the experimental spectrum. The proposed geometries containing two nitrides, meaning a nitrogen has been split, all give reasonable matching IR signals. The energetic differences are within the tolerance of 5 kJ/mol from the best matching simulated IR spectrum.

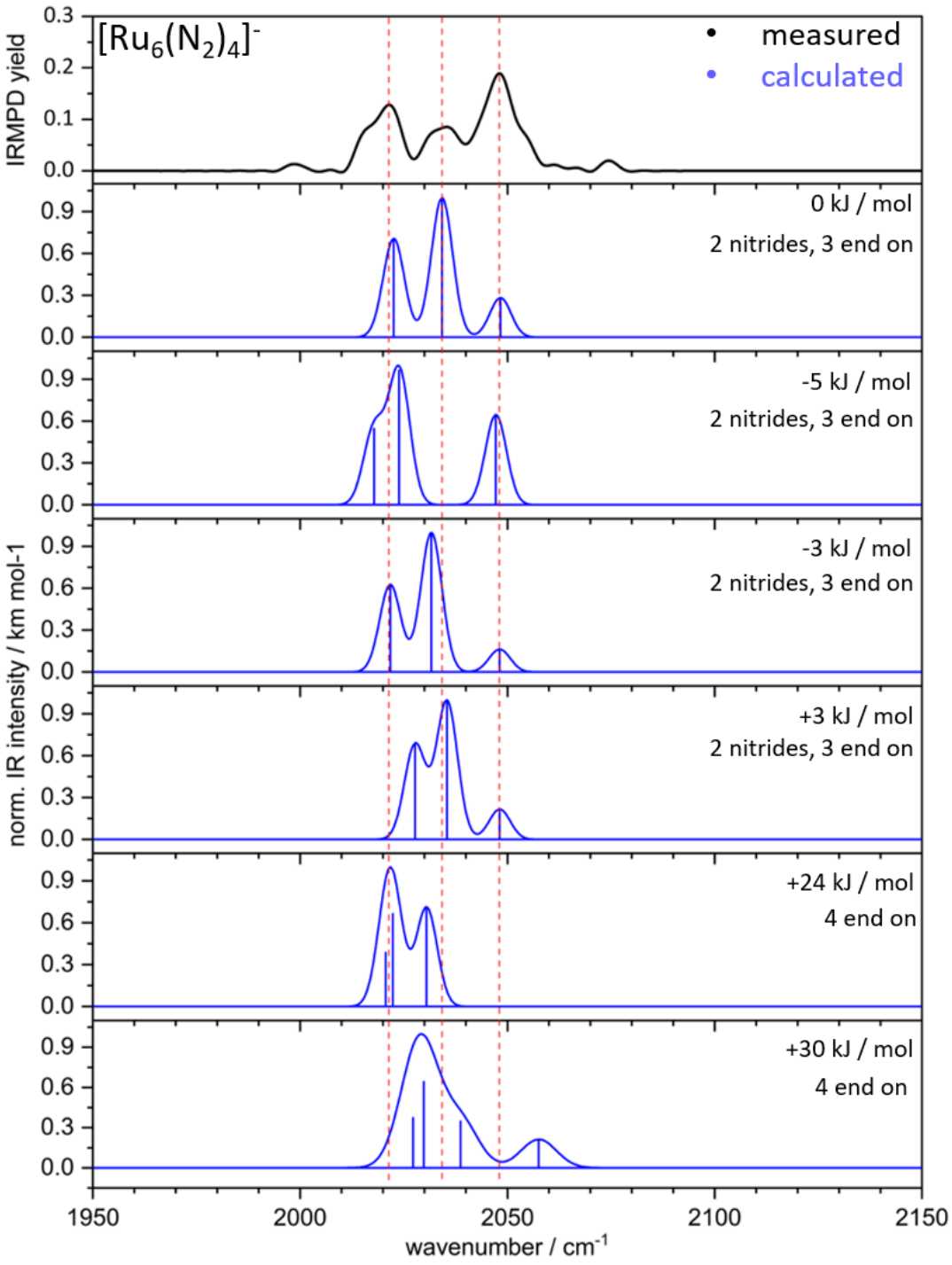
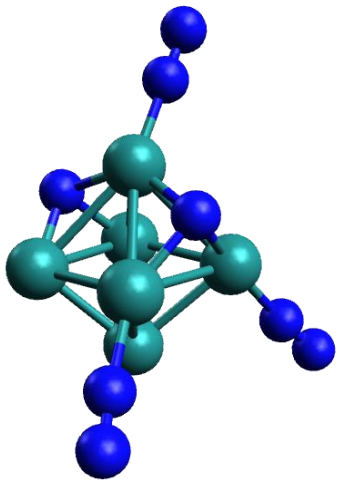


Fig. 7.2: IR-PD spectra of $Ru_6(N_2)_4^-$ is displayed at the top of the stack. The additional stacks show the calculated IR spectra of possible complexes. The designation nitride represents a cleaved dinitrogen molecule, the designation end-on represents an intact dinitrogen molecule absorbed end-on to the cluster surface.

On the other hand, simulated IR spectra of structures with four intact dinitrogen molecules adsorbed to the cluster surface do not match the IR pattern of the experiment. Additionally, they are about 25 kJ/mol disfavored by the calculated energy.

This information combined allows us to assume a nitrogen has been cleaved on the cluster surface. We propose the structure with the best matching IR signals to be the observed structure. Energetic differences are well within the accuracy of DFT modelling and thus we will consider the IR spectra for our designation. Within the geometries with matching IR patterns we chose the structure with the lowest energy.



It is the only cluster geometry and charge combination of ruthenium clusters we have observed this process.

Understanding the activation process further requires more DFT calculations. We conducted a study comparing structures with end-on adsorbed dinitrogen molecules with structures containing two nitrides. In Fig. 4, the red reaction coordinate describes the pathway with the nitrides forming after the first absorption, the blue pathway structures without a nitride formation.

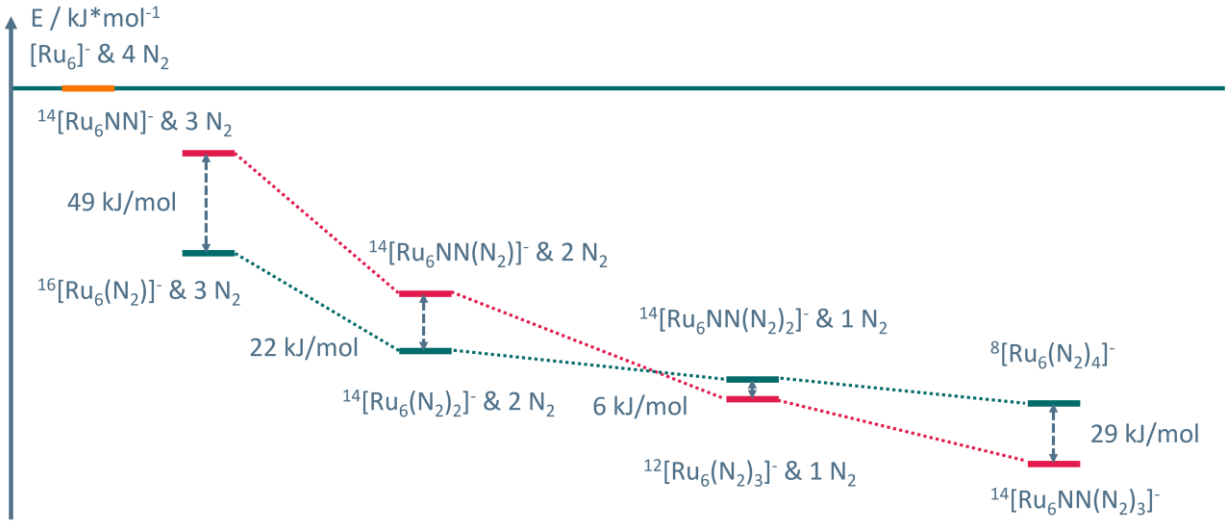


Fig. 7.3: Reaction coordinate, starting with the relative energy of the bipyramidal Ru6-cluster and four independent dinitrogen molecules. The red line indicates a reaction path assuming the cleavage of the first adsorbed dinitrogen. The blue reaction path displays a cluster-adsorbate complex with intact dinitrogen molecules. The four steps represent the sequential pick-up of four dinitrogen molecules to the structure.

We can observe that the relative energies of the two pathways do cross after the adsorption of the third dinitrogen molecule. This suggests the formation of the nitrides does only occur with the absorption of the third dinitrogen. For the cluster-adsorbate complex after four adsorbed dinitrogen, a nitride structure is favored, agreeing with the previous analysis of the $Ru_6(N_2)_4^-$ spectrum. The theoretical study gives a energy gap of 49 kJ/mol suggesting the nitride structure to be less favorable after the adsorption of the first dinitrogen.

However, we do not observe a IR signal for the first adsorbed dinitrogen and assumed the reason would be the activation of the dinitrogen molecule and hence the absence of a chromophore in the observed IR range. The IR spectra of $Ru_6(N_2)_n^-$ (n=2,3) do not provide enough information to determine a pathway with certainty.

There are multiple reasons for these observations. One is the dissociation energy of $Ru_6(N_2)_1^-$ is greater than the energy transferred into the system with the adsorption of a IR photon. We did however expose the complex to multiple IR photons, making this thesis improbable, but not impossible. Secondly, the DFT modeling could have missed a geometry energetically more favorable, possibly a intermediate position which does not

allow for a dissociation und the given conditions. Combining the results, we can not give a definitive answer to the findings but can ensure the presence of nitrides on the $Ru_6(N_2)_4^-$ cluster, where experiment and DFT modeling are in agreement.

The IR-PD spectra of $Ru_m(N_2)^-$ (m=7-12) are displayed in Fig. 5. The IR signals shown can be attributed to the stretching mode of the adsorbed dinitrogen molecules. They are all redshifted from the IR frequency of free dinitrogen at 2330 cm^{-1}. The redshift of the IR signal can be assigned to the level of activation of the dinitrogen molecule. According to the Blyholder model electron density is transferred from the cluster to the antibonding pi* orbital of the dinitrogen, weakening the triple bond. The position of the IR-signal shifts from 2010 cm^{-1} for the $Ru_7(N_2)^-$ cluster to 20250 cm^{-1} for the $Ru_{12}(N_2)^-$ cluster, illustrated by the solid red line in fig 5. This trend is referred to as the charge-dilution effect, correlating the size of the cluster – adsorbate complexes with the electronic charge. In this case the cluster size increases while the electronic charge is steady at -1. Thus the charge per cluster atom is reduced together with the ability to transfer electron density into the anti-binding pi* orbitals of the dinitrogen molecule.

An obvious deviation from the trend are IR signals of $Ru_8(N_2)^-$ and $Ru_9(N_2)^-$. The IR signal for $Ru_8(N_2)^-$ is significantly less redshifted than the trend would suggest For the IR-signals of $Ru_9(N_2)^-$ the opposite is true.

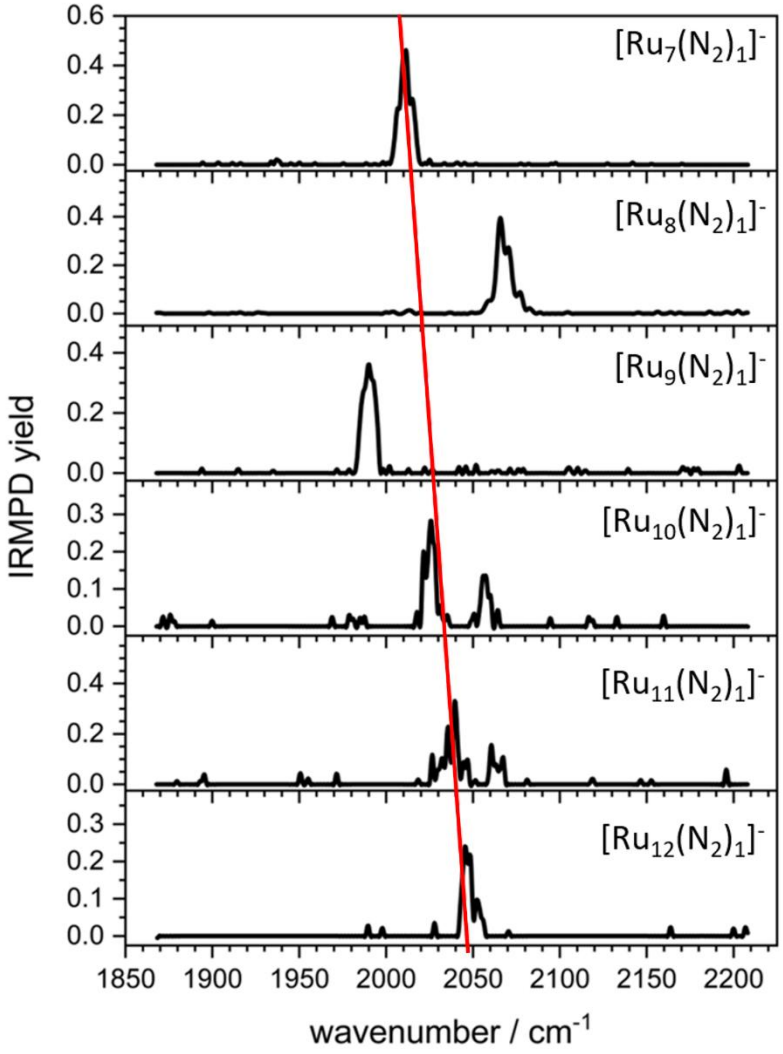


Fig. 7.4: IR-PD spectra of $Ru_m(N_2)^-$ (m=7-12) in the range from 1860 cm^{-1} to 2210 cm^{-1}. The red line guides the eye on the peaks of the IR signals in the IR PD spectra of $Ru_m(N_2)^-$ (m=7, 10-12). The outliers to this trend of $Ru_m(N_2)^-$ (m=8,9) will be explained in detail in the discussion.

A similar effect could be observed for the anionic cobalt cluster – dinitrogen complexes discussed in chapter 3. To discuss the effect, geometric models of the clusters were calculated using DFT theoretical modeling methods. The isotropic polarizability of the clusters give a measurement for the ability to donate electron density to the anti-binding pi* orbitals, discussed previously.

Tab. 1 shows the isotopic polarizabilities calculated for the defined cluster geometries. The results suggest a diminished polarizability for the Ru8- cluster, corresponding to a

lessened activation of the dinitrogen molecule. This effect corelates with a sharp drop in spin multiplicity. The Ru_9^- cluster has a heightened multiplicity corresponding again to the observations made in the IR-PD spectra.

Tab. 7.1: IR-PD band positions in relation to polarizability of clusters

n	IR-PD band position [cm^{-1}]	Isotrop. polarizability [$Bohr^3$]	Intensive polarizability per atom	multiplicity
7	2010	412	58.9	22
8	2070	365	45.6	6
9	1990	483	53.7	8

7.5 Conclusion

The results show a similar trend to the observations made in the anionic cobalt study. Observing the same effect with multiple transition metal clusters suggest a general trend in cluster-adsorbate interaction. One a general redshift, as suggested by Blyholder, as well as Dewar-Chatt and Duncanson, secondly the charge dilution effect observable in all cluster-adsorbate IR-PD experiments. Additionally, we can observe a effect of the isotropic polarizability on the effectiveness of the dinitrogen activation. This tertiary effect can only be observed in cases where the isotropic polarizability has sharp differences which lead to visible breaks in trends. However, outliers from the general trend are observable in most systematic cluster-adsorbate studies and should therefore be considered when interpreting activation processes.

7.6 Literature

[1] M. Capdevila-Cortada, *Nat Catal* **2019**, *2*, 1055.

[2] F. Haber, R. Le Rossignol, US971501, **1910**.

[3] H. Liu, *Chinese Journal of Catalysis* **2014**, *35*, 1619.

[4] a) G. Ertl, S. B. Lee, M. Weiss, *Surface Science* **1982**, *114*, 515; b) G. Ertl, *Catalysis Reviews Science and Engineering* **1980**, *21*, 201; c) G. Ertl, M. Neumann, K. M. Streit, *Surface Science* **1977**, *64*, 393.

[5] G. Blyholder, *J. Phys. Chem.* **1964**, *68*, 2772.

[6] J. Chatt, L. A. Duncanson, *J. Chem. Soc.* **1953**, 2939.

[7] J. Huang, M. Yuan, X. Li, Y. Wang, M. Li, J. Li, Z. You, *Applied Catalysis A: General* **2021**, *615*, 118058.

[8] a) E. L. Muetterties, T. N. Rhodin, E. Band, C. F. Brucker, W. R. Pretzer, *Chem. Rev.* **1979**, *79*, 91; b) S. M. Lang, T. M. Bernhardt, *Phys. Chem. Chem. Phys.* **2012**, *14*, 9255; c) M. B. Knickelbein, *Annual review of physical chemistry* **1999**, *50*, 79.

[9] *Energy-adjusted ab initio pseudopotentials for the first row transition elements*, **1987**.

[10] M. J. Frisch, G. W. Trucks, H. B. Schlegel, G. E. Scuseria, M. A. Robb, J. R. Cheeseman, G. Scalmani, V. Barone, G. A. Petersson, H. Nakatsuji et al., *Gaussian 16*, Gaussian Inc., Wallingford CT, **2016**.

8 Summary, conclusion, and outlook

Transition metal clusters are model systems which we use for the study of elementary steps of catalytic processes. This work is based on previous studies, both theoretical models and experimental setups. This work enlarges the scope of previous research by adding the analysis of adsorption analysis of size selected anionic transition metal clusters at cryo-conditions.

Since the experimental setup has been used to study mostly cationic transition metal-dinitrogen complexes, we now have a database to study the differences and trends of anionic and cationic cluster-adsorbate complexes. To summarize the found effects, an overview of both the cationic and anionic trends yields a better understanding of the processes governing the adsorption of dinitrogen to transition metals.

Anionic clusters of cobalt, nickel, rhodium and ruthenium were analyzed with IR-PD action spectroscopy. Fig. 1 shows the IR-PD spectra of anionic cobalt clusters (n=11-20) with one or two dinitrogen adsorbed to the surface. As discussed all IR signals are redshifted from the free dinitrogen stretching mode, but adhere to both the Blyholder model and the charge-dilution effect. To guide the eye, the red line shows the general trend of the IR signal position of the $Co_n(N_2)^-$ dinitrogen stretching modes. The guiding line emphasizes the outliers to this effect, especially observable with the $Co_{19}(N_2)^-$ and $Co_{20}(N_2)^-$spectra.

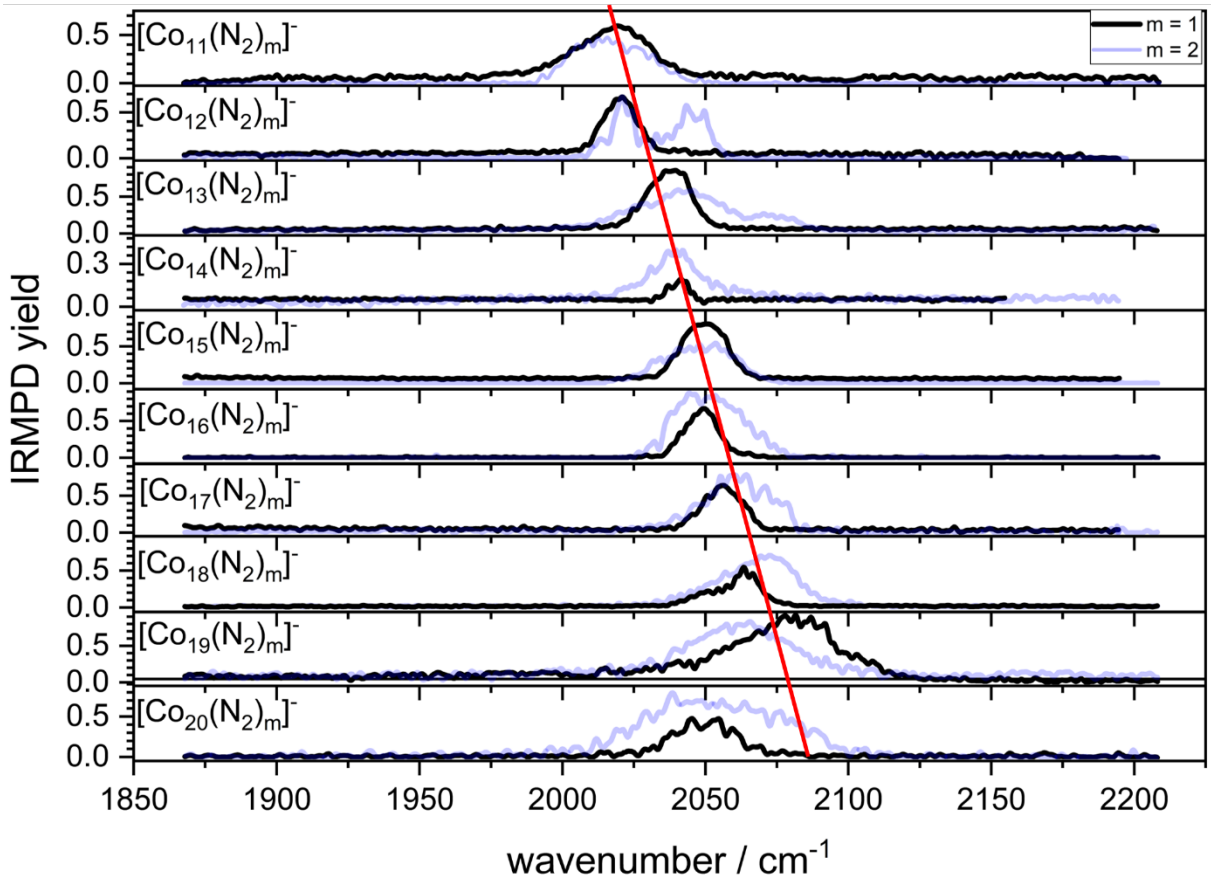


Figure 8.1: IR-PD spectra of $[Co_n(N_2)_m]^-$ for n = 11 – 20 and m = 1, 2. The dotted red line serves to guide the eye. The prevailing linear trend in the decreasing red shift of the N_2 stretching vibration frequency with increasing size of the cluster aligns with the decreasing charge per atom of the cobalt clusters. The spectrum of the first N_2 adsorbate of each cluster size shows only one peak, which indicates only one predominant isomer. $[Co_{20}(N_2)_1]^-$ shows a stronger red shift compared to n= 17-19 which might hint to a reorganization of the cluster core.

Our analysis shows a dependence of these outliers to the effects with the isotropic polarizability. In short, the polarizability has a direct effect on the interaction of the transition metal cluster with the dinitrogen molecule, which follows a sigma-donor-pi-acceptor synergism. Polarizability is a measurement of the cluster to donate electron density to the antibonding pi* orbital. The effect we see is the redshift of the dinitrogen stretching mode, which is larger with a higher amount of electron density in the antibonding pi* orbital.

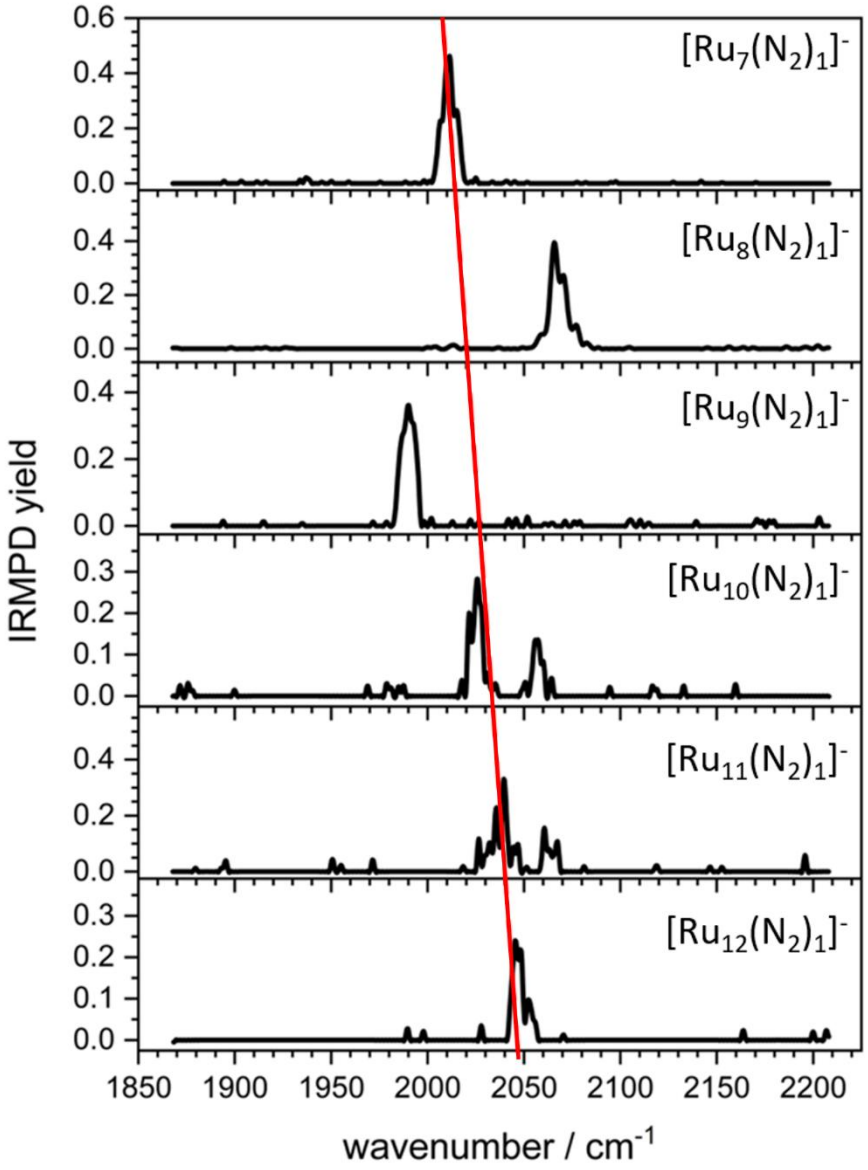


Figure 8.2: IR-PD spectra of $Ru_m(N_2)^-$ (m=7-12) in the range from 1860 cm^{-1} to 2210 cm^{-1}. The red line guides the eye on the peaks of the IR signals in the IR PD spectra of $Ru_m(N_2)^-$ (m=7, 10-12). The outliers to this trend of $Ru_m(N_2)^-$ (m=8,9) will be explained in detail in the discussion.

This effect is also observable in Fig. 2, which displays the IR signals of $Ru_n(N_2)^-$ (n=7-12). The red line illustrates the general trend of the position of the IR signals of the dinitrogen stretching mode, in accordance with both Blyholder and charge-dilution models. $Ru_8(N_2)^-$ and $Ru_9(N_2)^-$ are obvious outliers on both sides of the trend. The isotropic polarizabilities

of the clusters reflect the effects and therefore confirms the conclusions laid out for the anionic cobalt dinitrogen complexes.

Fig. 3 and Fig.4 show similar spectra to the previous two, for anionic rhodium and nickel cluster-dinitrogen complexes. While the spectra for $Rh_n(N_2)^-$ (n=5-13) shows a trend following Blyholder and charge-dilution models, the IR signals for the nickel -dinitrogen complexes $Ni_n(N_2)^-$ (n=10-21) do not adhere to a linear trend.

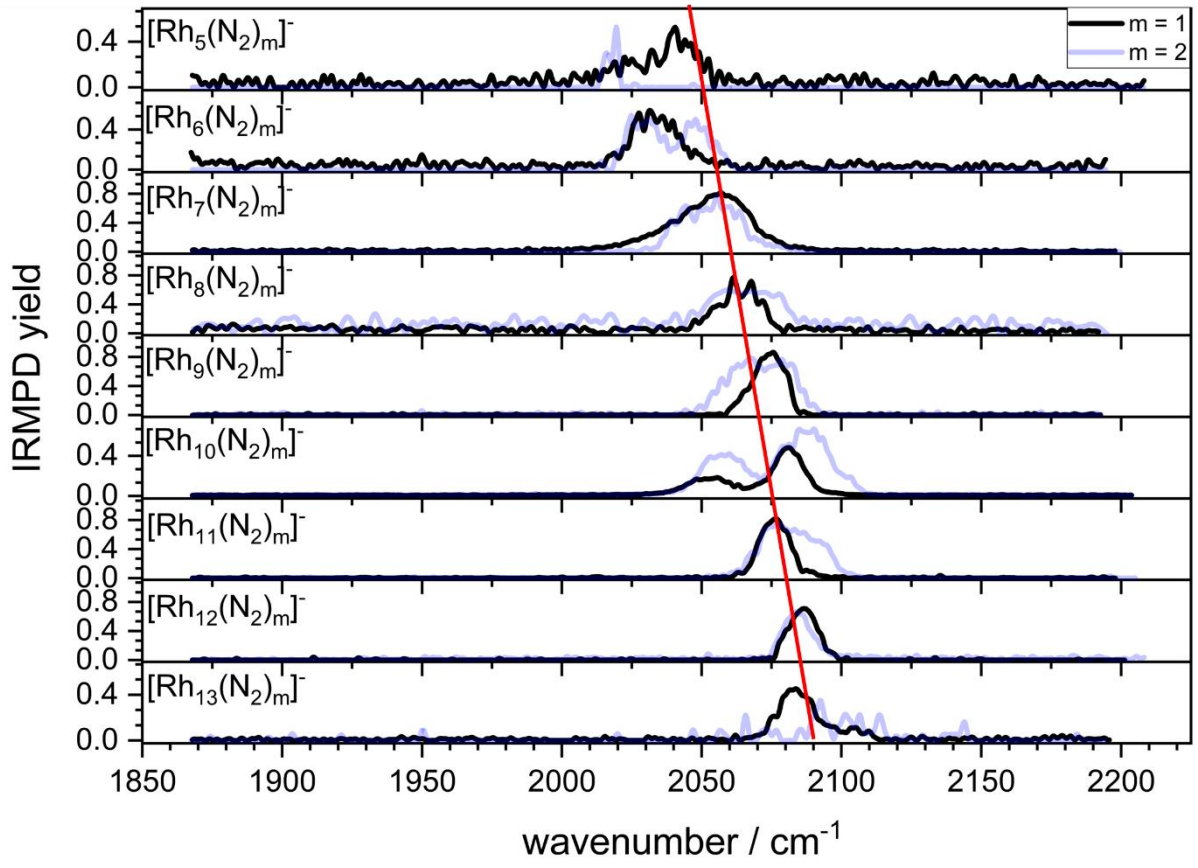


Figure 8.3: IR-PD spectra of $[Rh_n(N_2)_m]^-$ (n = 5-13; n = 1, intermittent/maximum N_2 uptake) from 1870 cm^{-1} to 2190 cm^{-1}. The recorded N_2 streching bands in the IR-PD spectra for the $[Ni_n(N_2)_1]^-$ (n = 10-21) (black line) reveal a red shift from the free N_2 stretching band (2330 cm^{-1}) ranging from 2040 cm^{-1} to 2095 cm^{-1} decreasing with the size of the cluster. This gradual change does not follow a linear trend. The recorded N_2 streching bands in the IR-PD spectra for the $[Ni_n(N_2)_m]^-$ (n = 10-21, m = intermittent/maximum) (blue line) show

significantly more features with the exeption of $[Ni_n(N_2)_m]^-$ (n = 12, 13) which show only one dominant feature.

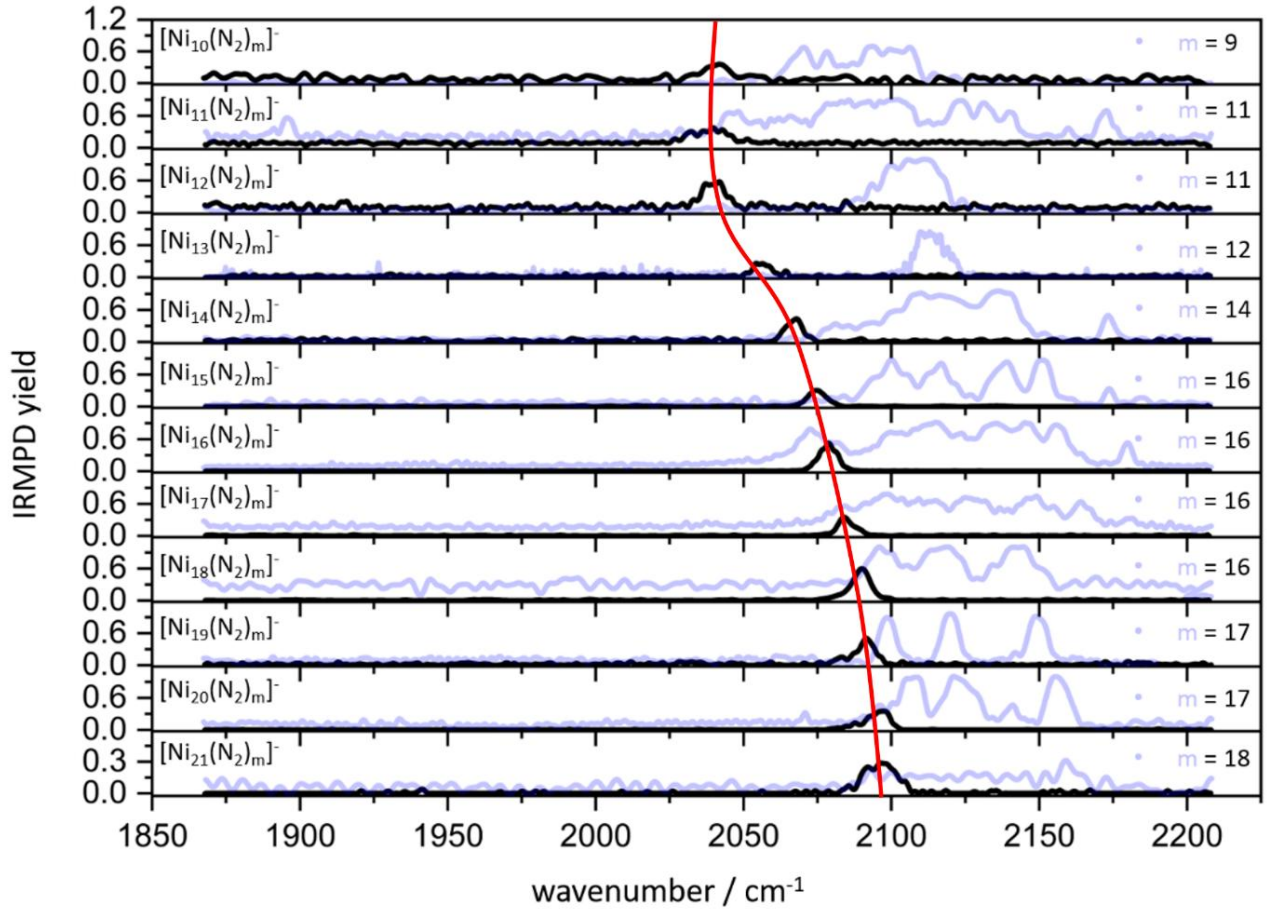


Figure 8.4: IR-PD spectra of $[Ni_n(N_2)_m]^-$ (n = 10-21; n = 1, intermittent/maximum N_2 uptake) from 1870 cm^{-1} to 2210 cm^{-1}. The recorded N_2 streching bands in the IR-PD spectra for the $[Ni_n(N_2)_1]^-$ (n = 10-21) (black line) reveal a red shift from the free N_2 stretching band (2330 cm^{-1}) ranging from 2040 cm^{-1} to 2095 cm^{-1} decreasing with the size of the cluster. This gradual change does not follow a linear trend. The recorded N_2 streching bands in the IR-PD spectra for the $[Ni_n(N_2)_m]^-$ (n = 10-21, m = intermittent/maximum) (blue line) show significantly more features with the exeption of $[Ni_n(N_2)_m]^-$ (n = 12, 13) which show only one dominant feature.

The comparison of the anionic nickel-dinitrogen complexes with studies of cationic nickel-dinitrogen complexes conducted with the same experimental setup yields a similar non-linear trend (see fig. 5). In general the IR-signals of the anionic cluster-adsorbate complexes show a larger redshift of the dinitrogen stretching modes from the

free dinitrogen molcule. Since the anionic TM clusters have more electron density to donate tot ehantibonding pi* orbital of the absorbed dinitrogen molecule, this trend is to be expected.

Between the anionic and cationic IR signals we can propose the position of a dinitrogen molecule adsorbed to a neutral cluster at 2158 cm-1. With our experimental set-up we are not able to examine neutral clusters, but compared to literature values we are in agreement with the current state of research.

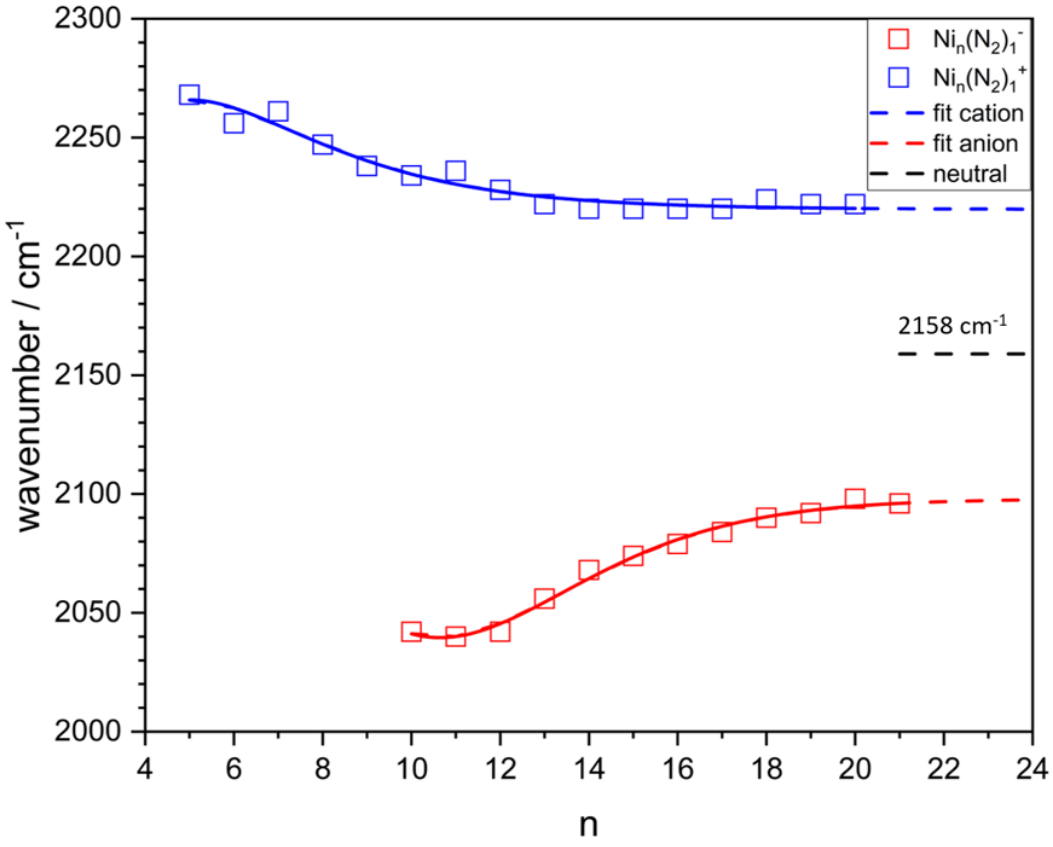


Figure 8.5: IR-PD frequencies of the N_2 stretching band of cationic cluster dinitrogen complexes $[Ni_n(N_2)_1]^+$ (n = 5-20) and anionic cluster dinitrogen complexes $[Ni_n(N_2)_1]^-$ (n = 10-21) are depicted in blue and red respectively. All frequencies are red shifted to the neutral N_2 streching band at 2330 cm^{-1}, cationic species to 2270 cm^{-1} to 2225 cm^{-1}, anionic species to 2040 cm^{-1} to 2095 cm^{-1}. Both reveal a asymptotic solution toward aprixmatly 2160 cm^{-1} with increasing cluster size, where we propose the neutral cluster dinitrogen complex N_2 IR streching band to be located.

Comparisons of anionic and cationic cluster - dinitrogen complexes for cobalt, rhodium and ruthenium are presented in fig. 6, fig.7 and fig.8. Trends according to the Blyholder and charge-dilution models are displayed as solid lines. The linear effects can be assigned a slope. If we prolong the slope and find the intersection of the linear fits of the anionic and cationic IR signal positions, we find a theoretical IR frequency we assign to the neutral cluster.

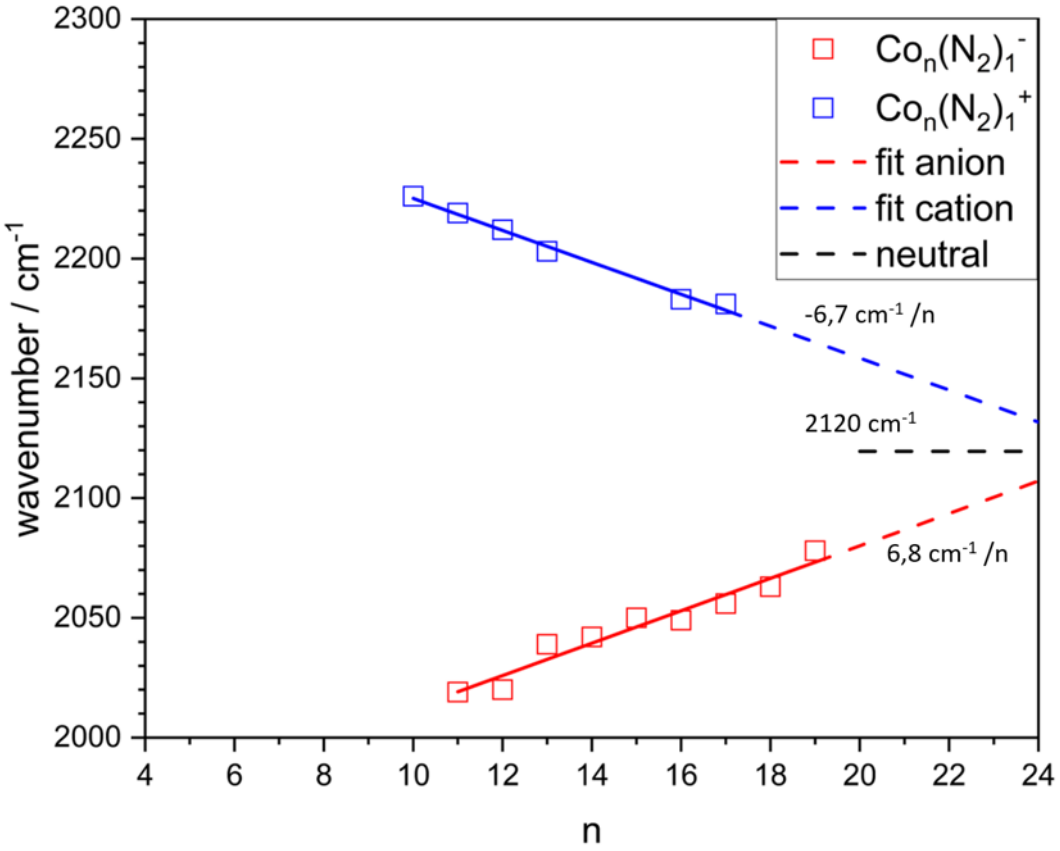


Figure 8.6: Recorded IR frequencies of $[Co_n(N_2)_1]^{+/-}$ for n = 10 – 19, cations in blue, anions in red. The dashed lines represent a linear fit of the data. The black line represents a hypothetical frequency of N_2 adsorbed onto a neutral cobalt surface. In both charge states a linear change in frequency with increasing cluster size is observed. The absolute value of both gradients is approximate.

The IR signals of the anionic and cationic clusters are however not expected to intersect, rather an asymptotic development, similar to the observations of the nickel complexes is probable.

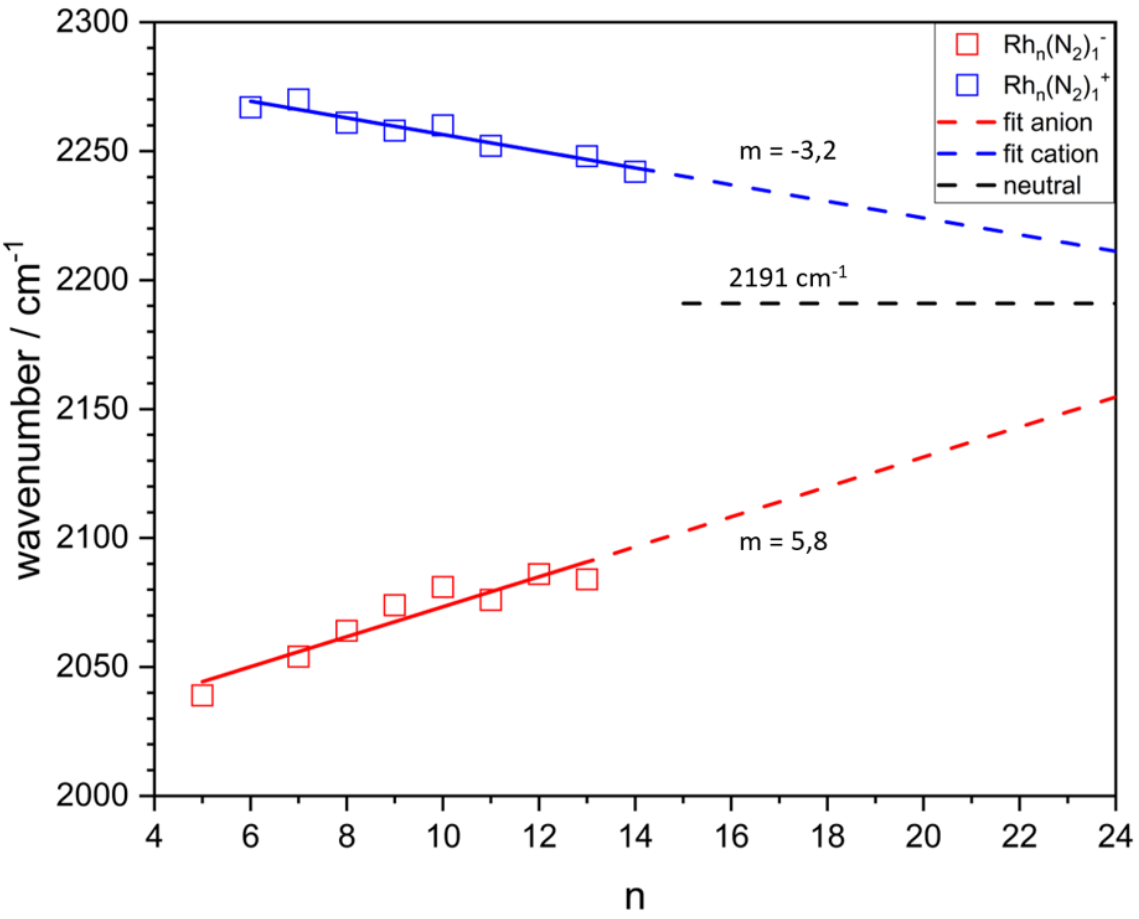


Figure 8.7: Recorded IR frequencies of $[Co_n(N_2)_1]^{+/-}$ for n = 10 – 19, cations in blue, anions in red. The dashed lines represent a linear fit of the data. The black line represents a hypothetical frequency of N_2 adsorbed onto a neutral cobalt surface. In both charge states a linear change in frequency with increasing cluster size is observed. The absolute value of both gradients is approximate.

The slopes of cationic and anionic cobalt cluster-dinitrogen complexes have the same absolute values of -6.7 cm-1/n and 6.8 cm-1/n. The slopes for rhodium and ruthenium cluster-adsorbate complexes are not symmetrical (see fig. 7 and fig. 8). The slopes range from absolute values of 3.2 cm-1/n to 5.8 cm-1/n, but the asymmetry is inverted in both cases. Therefore, no general trend can be concluded from the observations.

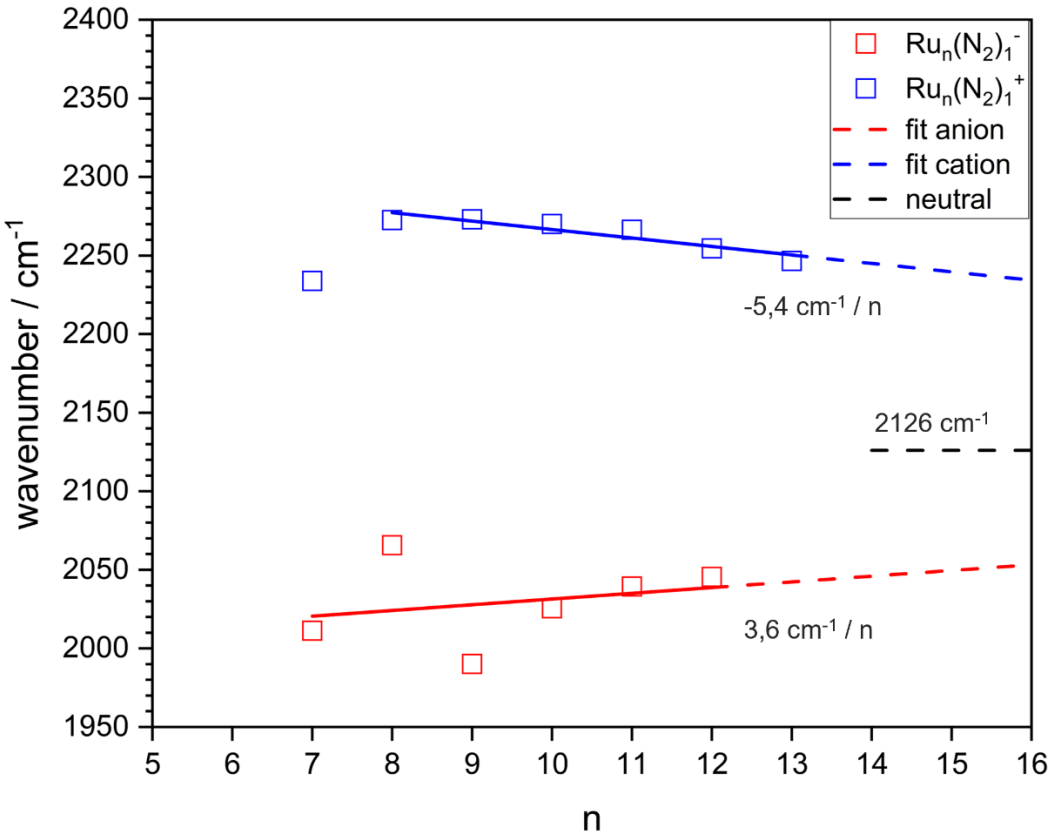
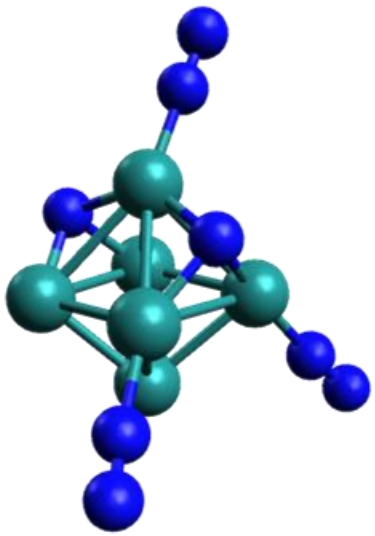


Figure 8.8: Recorded IR frequencies of $[Co_n(N_2)_1]^{+/-}$ for n = 10 – 19, cations in blue, anions in red. The dashed lines represent a linear fit of the data. The black line represents a hypothetical frequency of N_2 adsorbed onto a neutral cobalt surface. In both charge states a linear change in frequency with increasing cluster size is observed. The absolute value of both gradients is approximate.

In this work, we analyzed the activation process of dinitrogen on transition metal surfaces. Transition metal clusters allow us to correlate the geometric and electronic structures. The cleavage of dinitrogen could only be observed for the anionic ruthenium 6 cluster.

The implication of this study points to a significant influence on the correlation of electronic and geometric structure to the activation process in the nitrogen activation. The need for electron replenishment follows from the reduction process.



Empirical studies of catalysis point in the same direction. Electron surplus and a specific geometry are key elements in catalyst design.

Cluster chemistry studies develop a better understanding of elementary steps in dinitrogen catalytic processes. Anionic clusters give an additional angle to observations commonly made in cluster chemistry.

9 Short Summary

This thesis presents research studies investigating the activation of molecular dinitrogen on anionic transition metal clusters at cryo temperatures. In these studies we correlate the effects of both geometric and electronical properties of the adsorbate surface to the activation of dinitrogen.

The LVAP ion source produced transition metal cluster anions containing Cobalt, Nickel, Ruthenium and Rhodium. The FRITZ setup allowed the storage of the clusters and a reaction with added molecular dinitrogen. IR-PD spectroscopy was performed to investigate the vibrational modes of the cluster-adsorbate complexes. Together with quantum chemical modeling allowed the designation of geometries and electronic structure of the cluster-adsorbate complexes.

In agreement with previous studies performed with the FRITZ setup, the Blyholder effect, correlating the activation of dinitrogen with the charge of the transition metal cluster was observed. Additionally, the charge dilution model which postulates a correlation of the present charge surplus of the cluster with the degree of dinitrogen activation is in agreement with the experimental data obtained in the presented studies.

Furthermore, an additional effect connecting the polarizability of the surplus charge with the dinitrogen activation was observed and is described in the study in detail.The present data reveals three separate effects impacting the activation of dinitrogen, the charge itself, the available surplus charge, and the ability of named surplus charge to be donated to the dinitrogen facilitating the activation.

In the case of anionic Ru_6^- cluster, we were able to studz the complete activation of dinitrogen, forming the nitride species. This result, linking dinitrogen activation to a specific geometry and electronical structure underlines the importance of both geometry and electronic structure of the adsorbent surface for the successful activation of dinitrogen.

10 Kurzzusammenfassung der Dissertaion

Diese Arbeit präsentiert Forschungsstudien, die die Aktivierung von molekularem Distickstoff auf anionischen Übergangsmetallclustern bei Kryotemperaturen untersuchen. In diesen Studien korrelieren wir die Auswirkungen sowohl der geometrischen als auch der elektronischen Eigenschaften der Adsorbatoberfläche mit der Aktivierung von Distickstoff.

Die LVAP-Ionenquelle erzeugte Übergangsmetallcluster-Anionen, die Kobalt, Nickel, Ruthenium und Rhodium enthielten. Die FRITZ-Anordnung ermöglichte die Speicherung der Cluster und eine Reaktion mit zugesetztem molekularem Distickstoff. Zur Untersuchung der Schwingungsmoden der Cluster-Adsorbaten-Komplexe wurde IR-PD-Spektroskopie durchgeführt. Zusammen mit quantenchemischen Modellen konnten die Geometrien und die elektronische Struktur der Cluster-Adsorbaten-Komplexe bestimmt werden.

In Übereinstimmung mit früheren Studien, die mit dem FRITZ-Aufbau durchgeführt wurden, wurde der Blyholder-Effekt beobachtet, der die Aktivierung von Distickstoff mit der Ladung des Übergangsmetallclusters korreliert. Darüber hinaus stimmt das Ladungsverdünnungsmodell, das eine Korrelation zwischen dem vorhandenen Ladungsüberschuss des Clusters und dem Grad der Distickstoffaktivierung postuliert, mit den in den vorgestellten Studien gewonnenen experimentellen Daten überein.

Darüber hinaus wurde ein zusätzlicher Effekt beobachtet, der die Polarisierbarkeit der überschüssigen Ladung mit der Dinitrogenaktivierung in Verbindung bringt und in der Studie ausführlich beschrieben wird. Die vorliegenden Daten zeigen drei separate Effekte, die sich auf die Aktivierung von Dinitrogen auswirken: die Ladung selbst, die verfügbare überschüssige Ladung und die Fähigkeit der genannten überschüssigen Ladung, an das Dinitrogen abgegeben zu werden, wodurch die Aktivierung erleichtert wird.

Im Fall des anionischen Ru6-Clusters konnten wir die vollständige Aktivierung von Dinitrogen untersuchen, wodurch sich Nitridspezies bildeten. Dieses Ergebnis, das die Dinitrogenaktivierung mit einer bestimmten Geometrie und elektronischen Struktur in Verbindung bringt, unterstreicht die Bedeutung sowohl der Geometrie als auch der

elektronischen Struktur der Adsorbensoberfläche für die erfolgreiche Aktivierung von Dinitrogen.

Lebenslauf

Persönliche Daten

Name: Maximilian Luczak

Ausbildung

10/2013 – 12/2016 Studium, Technische Universität Kaiserslautern

Fach: Chemie

Abschluss: Bachelor of Science

12/2016 – 12/2018 Studium, Technische Universität Kaiserslautern

Fach: Chemie

Abschluss: Master of Science

02/2019-09/2023 wiss. Mitarbeiter, Technische Universität Kaiserslautern; Rheinland-Pfälzische Universität

List of publications

Cryo IR spectroscopy and cryo kinetics of dinitrogen activation and cleavage by small tantalum cluster cations

Daniela V. Fries, Matthias P. Klein, Annika Straßner, Maximilian E. Huber, Maximilian Luczak, Christopher Wiehn, and Gereon Niedner-Schatteburg

J. Chem. Phys. 159, 164303 (2023)

Glutathione kinetically outcompetes reactions between dimedone and a cyclic sulfenamide or physiological sulfenic acids

Eileen Bischoff [a], Lukas Lang [a], Jannik Zimmermann [b], Maximilian Luczak [a], Anna Maria Kiefer [c], Gereon Niedner-Schatteburg [a], Georg Manolikakes [a], Bruce Morgan [b], Marcel Deponte [a]

Free Radical Biology and Medicine 208 (2023) 165–17

Generative Adversarial Framework to Calibrate Excursion Set Models for the 3D Morphology of All-Solid-State Battery Cathodes

Orkun Furat,* Sabrina Weber, Anina Dufter, Johannes Schubert, René Rekers, Maximilian Luczak, Erik Glatt, Andreas Wiegmann, Jürgen Janek, Anja Bielefeld, and Volker Schmidt

Adv. Intell. Syst. 2026, 8, 2500572

Cyclometalated iridium complexes: Synthesis, photoluminescence, and catalysis

Pacifique Muhoza [a], Yu Sun [a], Harald Kelm [a], Subham Burai [a b], Maximilian Luczak [a], Katharina Rediger [a], Philipp Weber [a], Mahir Sönmez [a], Ann-Katrin Britzius [a], Maria Wächtler [a b], Gereon Niedner-Schatteburg [a], Marc H. Prosenc [a], Werner R. Thiel [a]

Journal of Organometallic Chemistry Volume 1045, 1 February 2026, 123976

Danksagungen

Ich danke Prof Gereon Niedner-Schatteburg für die Betreuung während meiner Promotion. Ich bedanke mich für die Möglichkeit sowohl in Kaiserslautern wie an großen Forschungseinrichtungen wie dem Bessy II und dem PSI in Villigen an großen Forschungsvorhaben mitzuwirken.

Ich bedanke mich bei Jun.Prof Jennifer Meyer für die Übernahme des Zweitgutachtens und bei Prof. Werner Tiehl für die Übernahme des Vorsitzes.

Ich bedanke mich bei meinen Arbeitskollegen meiner Gruppe, Christopher Wiehn, der mit mir das Büro geteilt und manche Strahlzeit verbracht hat. Gerade die langen Messzeiten während der Pandemie wären ohne ihn nicht machbar gewesen und ich denke wir waren ein gutes Team. Des Weiteren danke ich Thomas Kolling, Mike Lembach, Björn Kwasigroch, Daniela Fries, Matthias Klein, Annika Strasser und den vielen Bachelor und Masterstudenten, die die Gruppe bevölkert haben.

Ein weiterer großer Dank geht an meine Studien und Promotionskollegen, die mich immer fachlich wie moralisch unterstützt haben. Hier sind vor allem Benedikt Wyrwol, Christian Malcha, Yannick Mees und Patrick Gass unter vielen Weiteren zu nennen. Ohne euch wäre die Uni die Therapie gegen die Pandemie geworden, die sie für mich war. Vielen Dank für Alles!

Ich danke meinen Kollegen bei Math2Market, dass sie mich nur mit dem Versprechen eines Doktortitels aufgenommen und mir das Vertrauen geschenkt haben mich zu beweisen. Vielen Dank!

Ich bedanke mich bei meinem Vater für die stetige Motivation und realistische Einschätzung der Lage von außen, bei meiner Mutter für die immerwährende bedingungslose Unterstützung und bei meiner Schwester für ihre Freundschaft. Vielen Dank.

Eidesstattliche Erklärung

Hiermit bestätige ich, Sebastian Dillinger, dass die vorliegende Arbeit mit dem Titel „Activation of dinitrogen on size selected transition metal cluster anions at cryo temperatures“ gemäß der Promotionsordnung des Fachbereichs Chemie der Rheinland-Pfälzischen Technischen Universität selbstständig und mit keinen anderen als den hier angegebenen Quellen und Hilfsmitteln erstellt wurde.

Kaiserslautern, Februar 2026 Maximilian Luczak